

JOINT DENSITY-FUNCTIONAL THEORY FOR
ENERGETICS AND SPECTROSCOPY IN
COMPLEX AQUEOUS AND NONAQUEOUS
SOLVENTS

A Dissertation

Presented to the Faculty of the Graduate School
of Cornell University

in Partial Fulfillment of the Requirements for the Degree of
Doctor of Philosophy

by

Deniz Gunceler

May 2016

© 2016 Deniz Gunceler
ALL RIGHTS RESERVED

JOINT DENSITY-FUNCTIONAL THEORY FOR ENERGETICS AND
SPECTROSCOPY IN COMPLEX AQUEOUS AND NONAQUEOUS
SOLVENTS

Deniz Gunceler, Ph.D.

Cornell University 2016

Solvents are of great importance in many technological applications, but are difficult to study using standard, off-the-shelf *ab initio* electronic structure methods. This is because a single configuration of molecular positions in the solvent (a "snapshot" of the fluid) is not necessarily representative of the thermodynamic average. To obtain any thermodynamic averages (e.g. free energies), the phase space of the solvent must be sampled, typically using molecular dynamics. This greatly increases the computational cost involved in studying solvated systems.

Joint density-functional theory has made its mark by being a computationally efficient yet rigorous theory by which to study solvation. It replaces the need for thermodynamic sampling with an effective continuum description of the solvent environment that is in-principle exact, computationally efficient and intuitive (easier to interpret). It has been very successful in aqueous systems, with potential applications in (among others) energy materials discovery, catalysis and surface science. In this dissertation, we develop accurate and fast joint density functional theories for complex, non-aqueous solvent environments, including organic solvents and room temperature ionic liquids, as well as new methods for calculating electron excitation spectra in such systems. These theories are then applied to a range of physical problems, from dendrite formation

in lithium-metal batteries to the optical spectra of solvated ions.

BIOGRAPHICAL SKETCH

Deniz Gunceler was born in 1988 in Istanbul. He attended the Robert College of Istanbul, then moved to Ankara to study at Bilkent University. He is currently a PhD student in Cornell University. His research interests include electronic structure theory, density-functional theory, energy storage technologies, high-performance computing, machine learning and big data. He has numerous publications on academic journals and is co-inventor on a patent on alkaline battery materials.

ACKNOWLEDGEMENTS

First I would like to thank my thesis committee: My PhD advisor Prof T. A. Arias for the opportunity to work on very interesting research, Prof Erich Mueller for good advice and interesting discussions throughout the years (and also for introducing me to the wonderful world of Python!), Prof Carl Franck and Prof Doug James.

In my years at Cornell, I was blessed with many amazing colleagues and collaborators, both in Cornell and beyond. I would like to thank Ravishankar (Shankar) Sundararaman for his through mentorship during my first years and for expanding my horizons with his amazing intellect, Megan Holtz for being an great experimentalist and collaborator, Kiran Matthew for making our ideas widely accessible by making them available in VASP and Mukul Tikekar for long and fruitful discussions on the nature of lithium dendrites. I would especially like to thank Yalcin Ozhabes, who joined our group later in my studies but quickly became a great friend and colleague. Furthermore, I owe thanks to Christine Umbright, Doug DeSario, Kendra Letchorth-Weaver, Katie Schwarz, Xin Huang, Zhengyuan Tu, Pooja Nath, Snehashis Choudhury, Ran Wei, Semran Ipek, Prof Engin Durgun, Prof Ersen Mete, Prof Lynden Archer, Prof Joel Brock and many others for enriching discussions and/or collaborative work. Finally, I would like to thank everyone in the EMC2 collaboration and especially Prof Hector Abruna, who made it all happen.

Ithaca may be home to amazing gorges and scenery, but it is one's friends that made this place special. I consider myself lucky to have met many in my years here. I am grateful to Turan Birol without whose friendship and sharp wit grad school would have been incredibly dull; to Baris Ugurcan and Melik Turker who were amazing friends; to Ajay Bhat, Kaumudi Prabhakara and

Hyeri Lee of our little physics gang; and of course to Yucel Altug, Mehmet Demirtas, Zeyneb Saraoglu, Oznur Pehlivaner, Vural Kara, Efe Gencer, Anil Akturk, Nurten Akturk, Berk Esen, Ozgur Ozan Eken, Atakan Buke, Serhan Ardanuc, Hakan Atakisi, Onder Ozgener, Leyla Ozgener, Azar Eyvazov, Adem Merter Birson (and his band), Ahmet Serdar Simsek, Cagri Onuk, Can Bilir, Erdal Yilmaz, Baris Bircan, Daniel Citron, Michael Weiner, Susan Dittmer, Robin Bjorkquist and many others who made Ithaca and Cornell a great place.

A significant portion of the work in this thesis was supported as a part of the Energy Materials Center at Cornell (EMC2), an Energy Frontier Research Center funded by the U.S. Department of Energy, Office of Science, Office of Basic Energy Sciences under Award Number DE-SC0001086.

TABLE OF CONTENTS

Biographical Sketch	iii
Acknowledgements	iv
Table of Contents	vi
List of Tables	viii
List of Figures	x
1 Introduction	1
1.1 <i>Ab initio</i> electronic structure methods	3
1.2 Density-functional theory	6
1.3 Electronic structure of liquids and solvated systems	11
1.4 Joint density-functional framework	13
1.5 Implementations of (solvated) electronic structure methods	18
2 Towards a universal iso-density polarizable continuum model for molecular solvents in plane-wave DFT	23
2.1 Electrostatic contributions	25
2.2 Non-electrostatic terms in implicit solvation theory	32
2.3 Universal solvation model for molecular solvents	33
2.4 Surface solvation energy of Lithium Fluoride	42
2.5 Conclusion	44
2.6 Computational details	44
3 Stability and surface diffusion at lithium-electrolyte interphases with connections to suppression of dendrite suppression	46
3.1 Introduction	46
3.2 Computational Methods	48
3.3 Surface energies and diffusion	52
3.3.1 Comparing rates of deposition and diffusion	53
3.3.2 Change in the binding sites of Li-halides	55
3.3.3 Predictions for battery performance	56
3.3.4 Comparisons with measurements of short-circuit time	59
3.4 Conclusion	60
4 Joint density functional theory of room temperature ionic liquids: ion pairing and differential capacitance	63
4.1 Solvated electronic structure	67
4.2 Self-consistent determination of model parameters	72
4.3 Discussion	79
4.4 Solvation of metal surfaces	80
4.5 Conclusion	86
4.6 Appendix A: Importance of the vibrational and zero-point energy	87
4.7 Appendix B: Possibility of fractional (non-integer) effective ion charges	89

4.8	Appendix C: Computational/numerical details	90
5	Electronic excited states from stationary-point Kohn-Sham theory	92
5.1	Existing excited-state methods	93
5.2	Theory	95
5.2.1	Stationarity of the Hohenberg-Kohn functional	97
5.2.2	Stationarity of the Kohn-Sham functional	101
5.3	Finite vs extended systems	103
5.4	Issues with multiple-determinant (correlated) states	107
5.5	Open-shell systems: The case of solvated ions	109
5.6	Applications in lithium battery research	112
5.7	Computational Advantages/Disadvantages	116
5.8	Computational/Experimental Procedures	117
5.9	Conclusion	117
6	Outlook	119
	Bibliography	123

LIST OF TABLES

1.1	Asymptotic scaling of popular electronic structure methods. N is a measure of the system size, usually the number of atoms or electrons in the calculation. Hartree-Fock, Møller-Plesset perturbation (MP2) theory and Coupled Cluster (CCSD) are briefly discussed at the end of Section 1.1, while DFT is discussed in detail in Section 1.2.	6
1.2	Popular electronic structure codes [30, 31, 32, 33, 34, 35, 22, 23]. PW is an abbreviation for plane-waves and LAPW is an abbreviation for linearized augmented planes waves.	17
2.1	PCM parameters and RMS errors for the solvents used in the determination of the values for γ_0 and γ_1	35
2.2	Parameters for additional solvents of potential interest that were not used in the construction of the model.	39
2.3	Effective dipole moment of solvent molecules in vacuum and liquid phase (calculated self-consistently) All values in atomic units (ea_0).	39
2.4	Model predictions and experimental values for solvation energy in the pathological case of ethylene glycol. Second set of results ("corrected") are for a simple model to confirm the origin of the pathology. (See text.) All values are in kcal/mol.	42
2.5	Surface cleavage energy of an LiF (100) surface, in eV/nm ² . Vacuum denotes the surface energy in the presence of no solvent. PC and THF indicate propylene carbonate and tetrahydrofuran respectively.	44
4.1	The mean (ME) and mean absolute (MAE) errors for 57 molecules in 3 ionic liquids: [MEIM][Tf ₂ N] (1-methyl-3-ethylimidazolium bis(trifluoromethylsulfonyl) amide), [MBIM][PF ₆] (1-Butyl-3-methylimidazolium hexafluorophosphate) and [OMIM][PF ₆] (1-Methyl-3-octylimidazolium hexafluorophosphate). Results for individual molecules are plotted in Figure 4.2. In the last column, mean absolute errors of the SMD-GIL solvation model [156] for the same ionic liquids is presented for comparison. A dash (-) means that the data is not available at the given reference.	74
4.2	Self-consistent values for the critical electron density contour (n_c), the effective interfacial tension (τ) and the fractional dissociation (x) for 3 ionic liquids. n_c and τ values are given in atomic units, x is dimensionless. The last two columns show the results two disagreeing experimental measurements ($\Lambda_{imp}/\Lambda_{NMR}$ is the molar conductivity ratio). A dash (-) means that the data is not available at the given reference.	76

4.3	For the [MEIM][Tf ₂ N] RTIL, The energy difference between neutral and ± 1 charged "ion" pairs, calculated using PBE and PBE0 functionals. All energies are in electron-volts (eV). Positive numbers mean that neutral species are lower in energy whereas negative numbers mean that charged species are more stable.	80
4.4	The hard sphere radii for the different species. Values for Na ⁺ and Cl ⁻ have been included for comparison purposes.	91
5.1	First 8 excited states of the H ₂ O molecule. ΔE_{KS} is Kohn-Sham eigenvalue difference, ΔE_{stHK} is stationary-point Hohenberg-Kohn theory within NAKKA, ΔE_{TDFFT} is Tamm-Dancoff Time-Dependent DFT (performed with a 6-311++G** and plane-wave basis sets [209]), ΔE_{BS} is GW/BSE [199], ΔE_{CASSCF} is complete active space self-consistent field [210] and ΔE_{exp} is the experiment [208]. All DFT calculations were performed with the PBE exchange correlation functional [14].	103
5.2	HOMO-LUMO gaps calculated by different exchange correlation functionals, including stationary-point Hohenberg-Kohn theory (SPHK). All values in electron-volts (eV). Dashes (-) in the UV-vis column indicate values must be above the ~ 7 eV HOMO-LUMO gap of liquid water.	114

LIST OF FIGURES

1.1	Molecular dynamics and continuum model representations of an acetylsalicylic acid (aspirin) molecule solvated in water.	13
1.2	The density of the solvent (water) as a function of the distance from a solvated atom. Solvent density is given in units of the bulk density. The green line shows the exponential tail of the solute electron density on a log scale, the blue curve shows the solvent density. The critical solute electron density ($nc = 0.0007$) places the solute-solvent interface ~ 3 bohr from the atomic center.	15
1.3	The acetylsalicylic acid molecule from Figure 1.1, placed in a polarizable continuum. Bound charges form on the interface. . . .	16
1.4	The core and valence densities of the nickel. The valence states are 3d, 4s and 4p. Figure generated with the Opium pseudopotential generator [37].	19
1.5	The valence Kohn-Sham orbitals (3d, 4s and 4p) of the nickel. Solid lines are all-electron orbitals and dashed lines are the pseudized (smoothed) orbitals. Vertical lines show the core radii, beyond which pseudized and all-electron orbitals must agree. nickel pseudopotential generated with the Opium pseudopotential generator [37].	20
2.1	The effective dielectric constant of the nonlinear continuum theory [50] (with H ₂ O paramters) at different electric fields. SPC/E molecular dynamics and classical density-functional results are also plotted for comparison.	30
2.2	Fractional polarization at the solute-solvent interface as a function of the dimensionless effective field ϵ , solvated molecules (circles), charged metal surfaces (triangles) and ionic surfaces (squares).	31
2.3	Van der Waals radius, as determined using the equation of state for the gas phase versus result from density-functional theory procedure described in the text.	35
2.4	Surface tension correction ($\tau' = \tau_{\text{eff}} - \tau_{\text{bulk}}$) as a function of van der Waals factor $N_b C_{\text{solv}} / R_{\text{vdw}}^5$ (scaled to that of water to provide a dimensionless quantity for display purposes): data from fits to experimental solvation energies [56, 57, 58, 59] (black x's), best-fit linear correlation in the form of equation 2.14 (red line).	36
2.5	Theoretical versus experimental solvation energies for 124 solutes in 10 solvents computed in three theories: SMD[47], SCIPCM[69], and our work.	40

3.1	The percentage error in DFT lattice constants, plotted as a function of the experimental lattice constants. The solid black line represents exact agreement of theory and experiment. The dashed black lines represent $\pm 2.5\%$ deviations from experiment.	50
3.2	From left to right: rocksalt (Li-halides), anti-fluorite (Li_2O), zabuyelite (Li_2CO_3) and LiOH. Pictures were made using VESTA [121].	50
3.3	Surface binding energies versus its binding site. LiF is in the left, LiBr is on the right. The lowest energy binding sites are indicated with a green circle and the diffusion path is as shown with the green arrows. The black cross markers indicate our data points, the whole contour plot is generated using symmetries of the surface and cubic interpolation.	56
3.4	The surface diffusion barrier (x-axis) and the surface energy (y-axis) of various Lithium SEI materials. Hollow data points represent surfaces in contact with vacuum whereas filled data points represent the same surfaces in contact with the electrolyte (CH_3CN , modeled with a polarizable continuum model). The black markers indicate the bare metal calculations by Jäckle and Groß [78].	57
3.5	Battery short circuit times (from Lu, Tu, and Archer [107]) plotted as a function of the surface diffusion barrier. The green line is the best fit line, excluding the one outlier. The blue line shows has the slope for an Arrhenius process.	61
4.1	Two of the competing microscopic pictures for an RTIL. On the left hand side, most ions forming the RTIL have been dissociated and are free to move independently, with only a small fraction existing in pairs. On the right hand side, most ions have formed into pairs, with a very small fraction existing in dissociated form. Note that fractions and interatomic distances have been greatly exaggerated.	66
4.2	The solvation energies of neutral molecules, in three different room-temperature ionic liquids. Diagonal black solid line is the line of exact agreement; diagonal dashed lines show ± 1 kcal/mol errors. Errors for each solvent are reported in table 4.1.	73
4.3	2D scan of the mean absolute error in the solvation energies of neutral molecules in $[\text{MEIM}][\text{Tf}_2\text{N}]$. The solid black lines are contours of the mean absolute error. The dashed black line is the zero contour for the mean error.	75

4.4	The concentration of free (mobile) ions plotted as a function of the screening length. Red and black data points show the <i>ab initio</i> results, with and without the vibrational free energy. Solid blue and dashed green lines show the same, calculated using the Debye expressions in equation 4.5 and equation 4.6 respectively. The intersection of curves correspond to self-consistent solutions. For the ab-inio results, lines between the data points are only to guide eyes.	77
4.5	The surface charge on Au (111) surface in conact with [MBIM][PF ₆] RTIL, as measured by experiments (Silva [168] and Lockett [158]), as calculated by classical molecular dynamics simulations (Hu [153]) and as calculated by us (JDFT). Au, Pt and GC stand for gold, platinum and glassy carbon electrodes respectively. We determined surface charge by integrating capacitance (see Figure 4.6) over the potential.	82
4.6	The differential capacitance of [MBIM][PF ₆] RTIL, as measured by experiments (Silva [168] and Lockett [158]), as calculated by classical molecular dynamics simulations (Hu [153]) and as calculated by us (JDFT). Au, Pt and GC stand for gold, platinum and glassy carbon electrodes respectively.	83
4.7	In black, is the charging curve of the [MEIM][Tf ₂ N] RTIL in contact with a gold (111) electrode. In red, is the surface solvation energy (per unit area), as a function of the electrode potential. Lines are only to guide eyes.	85
4.8	The change in the vibrational modes of an [MEIM][Tf ₂ N] ion pair: The blue curve shows the change in the eigenvalue for each vibrational mode, a positive value meaning that the bound ion pair has a smaller eigenvalue than dissociated ion pair. The green curve is the cummulative sum of the blue curve. Eigenvalues are sorted, ascending in energy.	88

5.1	Cartoon representing the Hilbert space. The three surfaces represent subspaces formed by $\Psi^{(\alpha)}[n]$ for different n and α . Horizontal curves represent contours of constant electronic density n . The arrows represent the direction of the gradient of total energy wrt changes in the wavefunction. For wavefunctions belonging to one of the α -subspaces, this gradient is non-zero only in-plane, i.e. in the tangent space of the constant-density contour (this is shown with a perpendicular sign). For these wavefunctions, there exists some potential $V^{(\alpha)}$ that cancels this component exactly, making it an eigenfunction of the many-body hamiltonian. For an arbitrary wavefunction that is not necessarily in an α plane, the gradient is free to have non-zero components in all dimensions. This is illustrated with an angle θ between the gradient and the constant-density contour.	100
5.2	The first 8 excited states of the water molecule, calculated with different levels of theory. Raw data and references are in table 5.1.	104
5.3	Bandgap of Lithium Fluoride calculated using Perdew-Zunger LDA. Difference (ΔE) between the results obtained from the two methods (ground state eigenvalues and NAKKA) is plotted as a function of the number of k-points along each dimension.	105
5.4	HOMO-LUMO gap of straight-chain alkanes of increasing length, calculated using different levels of theory. Lines connecting data points are only to guide eyes. All calculations are done with the PBE exchange-correlation functional. Blue and green data points are obtained by subtracting Kohn-Sham eigenvalue differences from results computed by using more advanced levels of theory. The same data is plotted as a function of the alkane length (N) and the inverse alkane length (1/N).	106
5.5	Convergence of calculation of the first excited state of Cu^{2+} ion solvated in water, with an explicit first solvation shell: traditional approach in red and the shifted-eigenvalue Fermi function approach in black. Actual data in points, lines are only to guide eyes.	111
5.6	Experimental measurements and theoretical predictions for the uv-vis spectrum of CuSO_4 in water and methanol. Kohn-Sham eigenvalue differences (dashed lines), stationary-point Hohenberg-Kohn theory (solid lines) and uv-vis experiment (thick solid lines). Theoretical results include Gaussian broadening of 0.2 eV (water) and 0.4 eV (methanol), determined by best agreement with experiment.	112
5.7	The intensity of the 6 eV EELS signal observed by Holtz et. al. [224], measured as a function of the distance from the cathode nanoparticle. Experimental data courtesy of Megan Holtz [224].	113

5.8 A selection of the most probable species involved in experiment
by Holtz et. al. From left to right: LiSO_4^- , $\text{Li}[\text{H}_2\text{O}]_4^+$, HSO_4^- and
 LiOH . Pictures were made using Avogadro [225]. 113

CHAPTER 1

INTRODUCTION

From the very early days of scientific endeavour, scientists have aspired for the ability to predict properties of real materials from fundamental physical principles. Over the last several decades, new approximate theories together with the rise of fast and inexpensive computers have made this aspiration possible. *Ab initio*¹ electronic structure theory has now become an established and very successful field of study with application areas in physics, chemistry, materials science and even biology, to the point that it is now possible to design new functional materials on the computer.

Application of *ab initio* electronic structure methods to the study of fluids and solvated species have lagged behind their application elsewhere (e.g. crystals and gas-phase molecules), even though the physics of solvation is of great importance. This is because, in situations involving a fluid, one needs to sample the phase space of possible fluid configurations, which requires one to solve the quantum mechanical problem repeatedly for different configurations of the fluid molecules. Not surprisingly, the need for sampling increases the computational cost enormously. It is thus very important to develop approximate theories that simplify the application of electronic structure methods to fluids and solvated species.

Joint density-functional theory (JDFT) is an in-principle exact framework developed over the last decade that has become one of the several successful ways for studying systems in thermal equilibrium with a liquid solvent. To date, it has been applied primarily for calculating free energies and capacitances in

¹ *Ab initio* is Latin for "from the beginning" or "from first principles".

aqueous systems. This thesis develops accurate, stable and fast approximations and algorithms that simplify the study of solutes (including ions), surfaces and excited states in complex, nonaqueous environments.

In the second chapter, we focus on the polarizable continuum limit of joint density functional theory and develop a framework for constructing polarizable continuum models for a large class of protic and aprotic molecular solvents, without having to re-train the description for each new solvent. The third chapter presents an application of the continuum model developed in the second chapter to the infamous dendrite problem in lithium metal batteries. Here, the focus is on the explanation of new experiments from the Archer group in Cornell University, which were inspired from the theoretical work included in this thesis. These experimental results show that the composition of the surface passivation layer on a lithium-metal anode has a profound impact on the battery's stability and performance. In the fourth chapter, we make the first attempt to construct a joint density-functional theory of room-temperature ionic liquids (RTILs). RTILs are salts that are molten at room temperature, and thus have many current and potential applications in electrochemistry. The fifth chapter develops a new method, the stationary-point Hohenberg-Kohn theory, for calculating the excitation spectra of electrons. This method is thoroughly benchmarked and then applied to calculate the uv-vis (ultraviolet-to-visible) spectra of solvated ions (in both aqueous and nonaqueous solvents). Finally, we give some general conclusions in Chapter 6.

A note about units: unless explicitly stated otherwise, all quantities in this thesis are expressed in atomic units, in which energies are measured in Hartrees (~ 27.21 eV) and distances are measured in Bohr (~ 0.529 Angstrom).

1.1 *Ab initio* electronic structure methods

Since the development of quantum mechanics in the early 20th century, the fundamental laws of physics governing the behaviour of liquids and solvated species have been well understood. In fact, as far back as 1929, Paul Dirac, one of the founders of modern physics, stated [1]

“The general theory of quantum mechanics is now almost complete, the imperfections that still remain being in connection with the exact fitting in of the theory with relativity ideas. These give rise to difficulties only when high-speed particles are involved, and are therefore of no importance in the consideration of atomic and molecular structure and ordinary chemical reactions, in which it is, indeed, usually sufficiently accurate if one neglects relativity variation of mass with velocity and assumes only Coulomb forces between the various electrons and atomic nuclei. The underlying physical laws necessary for the mathematical theory of a large part of physics and the whole of chemistry are thus completely known, and the difficulty is only that the exact application of these equations leads to equations much too complicated to be soluble. It therefore becomes desirable that approximate practical methods of applying quantum mechanics should be developed, which can lead to an explanation of the main features of complex atomic systems without too much computation.”

The first approximation utilized, almost ubiquitously in electronic structure theory, is the Born-Oppenheimer approximation. Due to the large differ-

ence between electron (m_e) and nuclei masses (the proton mass $m_p \sim 1800m_e$), this approximation assumes that the motion of the electrons can be separated (and solved independently) from the motion of the nuclei. In other words, the timescales of electronic motion are much shorter than the timescales of nuclear motion ². Thus the electrons can be assumed to react instantaneously to any change in nuclear positions. Therefore, the problem of predicting most material properties then becomes, to a large extent, the problem of solving many-electron problems at given external potentials, specifically those potentials provided by different arrangements of the nuclei composing the systems of interest.

Once the Born-Oppenheimer approximation is made, the Schrödinger equation for the electrons becomes:

$$\hat{H}\Psi = E\Psi,$$

where the Hamiltonian operator \hat{H} is (in atomic units)

$$\begin{aligned} \hat{H} &= \hat{T} + \hat{V} + \hat{U}_{ee} + \hat{U}_{NN} \\ &= \sum_j \left(-\frac{1}{2} \nabla_j^2 + V(\vec{r}_j) \right) + \frac{1}{2} \sum_{j,k} \frac{1}{r_{jk}} + \hat{U}_{nn}. \end{aligned}$$

In the equation above, \hat{T} is the kinetic energy operator, \hat{V} is the total external potential (which arises entirely from the nuclei), \hat{U}_{ee} is the electron-electron repulsion and \hat{U}_{nn} is the nuclear-nuclear repulsion. As mentioned above, we work in units where $\hbar^2/2m = 1$ Hartree-Bohr², $k_e e^2 = 1$ Hartree-Bohr. From the perspective of electrons, the nuclear-nuclear repulsion is a constant energy term that does not affect the eigenfunctions Ψ . The external potential is computed by

² The motion of the nuclei, with the exception of very light elements such as hydrogen, are classical and obey Newton's laws of motion.

the summing over all the nuclei

$$\hat{V}(\vec{r}_j) = \sum_{\alpha} \frac{Z_{\alpha}}{r_{j\alpha}}$$

where α enumerates all nuclei, Z_{α} is the charge of each nucleus and $r_{j\alpha} = |\vec{r}_j - \vec{r}_{\alpha}|$.

Finally, the nuclear-nuclear repulsion energy is given by

$$U_{nn} = \frac{1}{2} \sum_{\alpha, \alpha'} \frac{Z_{\alpha} Z_{\alpha'}}{r_{\alpha\alpha'}}.$$

The ability to solve the Schrödinger equation for a given (fixed) set of atomic coordinates allows for the determination of the Born-Oppenheimer surface, from which many important physical properties can be extracted. For example, each local minimum in the Born-Oppenheimer surface corresponds to a stable or meta-stable structure of a given molecule or crystal. Solving the many-body Schrödinger equation, however, is a momentous task. Exact solutions, whether analytical or numerical, exist only for a handful of model many-electron systems such as the uniform electron gas [2, 3], the airy gas [4] and the harmonium atom [5]. In most calculations involving atoms and molecules, some simplifying assumptions about the wavefunction must be made. For example, Hartree-Fock theory, which serves as the starting point for many more sophisticated quantum-mechanical calculations, assumes Ψ to be a single Slater determinant, while configuration interaction and coupled cluster methods assume Ψ to be well represented by a finite sum of several Slater determinants. See Table 1.1 for the scaling of the computational costs of these methods.

Hartree-Fock	$O(N^4)$
MP2	$O(N^5)$
CCSD	$O(N^6)$
semilocal DFT	$O(N^3)$

Table 1.1: Asymptotic scaling of popular electronic structure methods. N is a measure of the system size, usually the number of atoms or electrons in the calculation. Hartree-Fock, Møller-Plesset perturbation (MP2) theory and Coupled Cluster (CCSD) are briefly discussed at the end of Section 1.1, while DFT is discussed in detail in Section 1.2.

1.2 Density-functional theory

From a computational perspective, the problem with wave-function methods is that the ‘size’ of the Hilbert space grows exponentially with the number of electrons in the system, with three spatial dimensions and one spin dimension added every time a new particle is introduced. There are, of course, more compact approximations to the many-body wavefunction and it is possible to develop accurate methods that scale polynomially with the number of variables. However, the resulting exponents are from the 4th to the 6th power (or more), which are still too large for the study of many systems of practical interest. It is, therefore, preferable to formulate a theory that expresses the total energy of the system as a function of a simpler and more compact object, for example, the mean density of the electron cloud. This is indeed what the density-functional methods are designed to achieve.

The first attempt at a density-functional theory was the Thomas-Fermi approximation [6, 7]. In this scheme, the total energy of the many-body system was approximated as

$$E [n] = C_F \int d^3r [n(\vec{r})]^{5/3} + \int d^3r V(\vec{r}) n(\vec{r}) + \frac{e^2}{2} \int \int d^3r d^3r' \frac{n(\vec{r}) n(\vec{r}')}{|\vec{r} - \vec{r}'|}$$

where $C_F = \frac{3}{10} (3\pi^2)^{2/3}$. The first term in the functional approximates the kinetic energy of the electrons in a form that is exact for an electron gas of uniform density. The last (third) term approximates the electron-electron repulsion, which is treated at a mean-field level, ignoring the tendency of electrons to avoid each other and, thus, treating each as feeling the potential from the average density. In this simple form however, Thomas-Fermi theory is not accurate enough for the prediction of material properties. This is due to two reasons: First, the $n^{5/3}$ kinetic energy term, while exact for the uniform electron gas, fails for electrons localized around atoms. It does not reproduce the shell structure of atoms, which is essential for the description of many physical and chemical properties. The second reason is that the treatment of the electron-electron repulsion at a mean-field level (by neglecting any correlation) significantly overestimates the coulomb repulsion.

While there were many attempts to improve the Thomas-Fermi approximation³, the real breakthrough for density-functional theory came with Hohenberg and Kohn's now famous work [8]. They showed that there exists a functional of the electron density, $E_{HK} [n]$, whose minimum gives the ground state energy and density of the many-body system. Immediately below, we use the Levy constrained search procedure [9] to demonstrate this profound result.

Let Ψ be a normalized and anti-symmetric wavefunction. As discussed earlier, the total energy as a function of Ψ is given as

³ For example, one scheme prescribes improving the Thomas-Fermi kinetic energy by mixing in some fraction of the exact kinetic energy of a single electron system at the same density (the so-called von Weizsacker term).

$$\begin{aligned}
E[\Psi] &= \langle \Psi | \hat{H} | \Psi \rangle = \langle \Psi | \hat{T} + \hat{U}_{ee} + V | \Psi \rangle \\
&= \langle \Psi | \hat{T} + \hat{U}_{ee} | \Psi \rangle + \int d^3r V(\vec{r}) n(\vec{r}).
\end{aligned}$$

By the Rayleigh-Ritz variational principle, the ground state energy E_{GS} may be found by minimizing the above functional over all possible fermionic Ψ ,

$$E_{GS} = \min_{\Psi} \left(\langle \Psi | \hat{T} + \hat{U}_{ee} | \Psi \rangle + \int d^3r V(\vec{r}) n(\vec{r}) \right). \quad (1.1)$$

We now exploit the fact that the second term (coupling to the nuclei) does not have an explicit dependence on the many body wavefunction, but depends on it only through the *density*,

$$E_{GS} = \min_n \left(\min_{\Psi \rightarrow n} \langle \Psi | \hat{T} + \hat{U}_{ee} | \Psi \rangle + \int d^3r V(\vec{r}) n(\vec{r}) \right) \quad (1.2)$$

$$= \min_n \left(F[n] + \int d^3r V(\vec{r}) n(\vec{r}) \right). \quad (1.3)$$

In the expression above, the outer minimization is performed over all densities n which integrate to the correct number of electrons, whereas the inner minimization is performed over all wavefunctions Ψ that integrate to n . Here, we observe that $F[n] \equiv \min_{\Psi \rightarrow n} \langle \Psi | \hat{T} + \hat{U}_{ee} | \Psi \rangle$ itself is a function that depends on the electron density only. Equation 1.3 thus shows that E_{GS} can be expressed as a function of density alone.

While the Levy constrained-search procedure demonstrates the existence of a functional $F[n]$, it offers very little practical help in way of constructing an explicit form which may be used for practical computations. Indeed, to-date, an

exact explicit form of $F [n]$ is not known. Furthermore, density-only approximations to $F [n]$ have not advanced sufficiently to be of use in predicting material properties. See [10] for a comprehensive review of density-only DFT. Most applications of density-functional theory today follow the prescription of Kohn and Sham [11], where the kinetic energy $T [n]$ of the many body system is approximated with the minimum kinetic energy of a non-interacting system of the same density

$$T [n] \equiv -\frac{1}{2} \min_{\{\phi_j\} \rightarrow n} \sum_j \int d^3 r \phi_j(\vec{r}) \nabla^2 \phi_j(\vec{r}), \quad (1.4)$$

where $\{\phi_j\} \rightarrow n$ denotes a minimization over Slater determinants giving rise to density n .

Once the approximation (1.4) is made, $F [n]$ may then be expressed as

$$F [n] = T [n] + \frac{1}{2} \int d^3 r d^3 r' \frac{n(\vec{r}) n(\vec{r}')}{|\vec{r} - \vec{r}'|} + E_{xc} [n],$$

where the second term is the mean-field Coulomb interaction and the third term $E_{xc} [n]$ is the famous exchange-correlation piece, whose purpose is to correct for the errors introduced by the previous two terms.

For semilocal exchange-correlation functionals, which we will use extensively throughout this thesis, the exchange-correlation energy is approximated as the integral of an exchange-correlation energy density per particle ($\varepsilon_{xc}[n]$) which depends on the local electron density and its gradients.

$$E_{xc} \equiv \int d^3 r \varepsilon_{xc} [n(\vec{r}), |\vec{\nabla} n(\vec{r})|, ..] n(\vec{r}).$$

When the dependence of ε_{xc} is only on the density, and not on gradients of the density, such approximations are called *local density approximations* (LDAs). The

next step in the ladder of approximations are the *generalized gradient approximations* (GGAs), where the gradient of the density is also used. Recently, there have also been developments towards meta-GGA functionals, where the Laplacian of the density or the kinetic energy density is also used in the construction of ε_{xc} .

There are multiple approaches to exchange-correlation functional construction, and a very large family of functionals exist. Most functionals are exact in the uniform electron gas limit, for which numerical values values can be obtained through quantum Monte Carlo many body calculations [2]. In the chemistry community, the most popular choice is B3LYP [12], a hybrid functional that also contains some non-local ("Fock") exchange in the same form as appears in the Hartree-Fock approximation. B3LYP, however, is highly parametrized and empirical, working with remarkable accuracy in systems for which it was designed (organic/inorganic molecules), while exhibiting much larger errors for systems outside its domain of optimization (e.g. metals) [13]. In contrast, the most popular choices for the exchange-correlation functional in physics and materials science communities are the PBE [14] and PBEsol [15] functionals, which are of the GGA form. While not as accurate as B3LYP for molecules, these latter functionals have a wider domain of applicability and do not contain empirical parameters.

Use of "orbitals" (the $\{\phi_j\}$) in DFT as in Eq 1.4 is a well accepted practice to achieve the necessary level of accuracy. This, of course, comes at the cost of increased computational complexity. A density-only DFT (sometimes also called orbital-free DFT) would, theoretically, be significantly more efficient (potentially even scaling linearly). Therefore, development of density-only kinetic

energy functionals is an active field of research area [10, 16, 17, 18]. However, as of today, no orbital-free kinetic energy functional can come close to the level of accuracy of so called "Kohn-Sham" orbital approaches. The lack of an orbital-free kinetic energy functional is not the only reason holding back orbital-free DFT. Most DFT implementations include the effect of core electrons through the use of pseudopotentials. Most pseudopotentials today require nonlocal orbital-dependent operators for accuracy. Thus another important requirement for potential future orbital-free DFT is the development of accurate, density-only ("local") pseudopotentials [16].

1.3 Electronic structure of liquids and solvated systems

Application of Kohn-Sham DFT to the study of liquids and solvated systems is more involved than the application to solids or molecules. At room temperature, atomic nuclei in solids and molecules are mostly stationary. As such, a single DFT calculation at fixed nuclear coordinates is often sufficient for the determination of many physical quantities. However, this is not the case for liquids, where atoms are free to move even at room temperature. Therefore, for systems involving liquids, thermodynamic sampling is needed for the determination of the physical quantities of interest (e.g. free energy of the system and any thermodynamic averages of interest). This can be achieved of course using *ab initio* molecular dynamics (AIMD), where the forces at each time step are determined using DFT and the atomic positions are updated using Newton's equations. While this is a popular approach that has found widespread use in the community, the approach is extremely computationally demanding and not optimal for high-throughput studies involving large numbers of different mate-

rials.

The *Quantum Mechanics / Molecular Mechanics* (QM/MM) approach was awarded the Nobel prize for chemistry in 2013. This method offers a way to accelerate *ab initio* molecular dynamics (AIMD) simulations by dividing the system under study into two regions: a small region described by quantum mechanics (usually DFT) and a much larger region described with a less sophisticated level of theory (usually model classical force fields). The use of a less sophisticated (hence faster) method for a large part of the system allows the forces at each time step to be computed more efficiently. This approach was best summarized by A. Warshel during his Nobel lecture [19],

“In light of the complexity of macromolecular complexes, it is essential to use computer simulations to describe how the molecular forces are related to a given function. However, using a full and reliable quantum mechanical representation of large molecular systems has been practically impossible. The solution to this (and related) problems has emerged from the realization that large systems can be spatially divided into a region where the quantum mechanical description is essential (e.g. a region where bonds are being broken), with the remainder of the system being represented on a simpler level by empirical force fields. This idea has been particularly effective in the development of the combined quantum mechanics/molecular mechanics (QM/MM) models.”

These QM/MM models [20] have been very successful and have been implemented in many popular electronic structure software packages. For example,

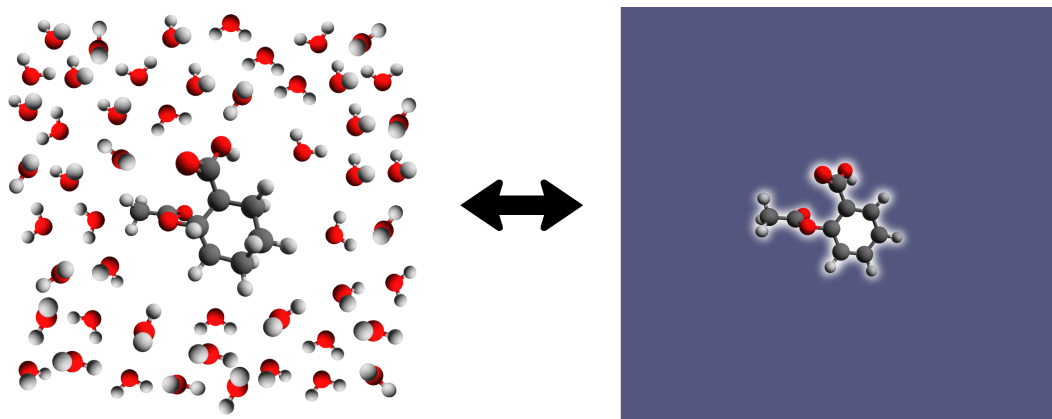


Figure 1.1: Molecular dynamics and continuum model representations of an acetylsalicylic acid (aspirin) molecule solvated in water.

ONIOM [21], which allows for the combination of *ab initio* methods with faster semi-empirical methods, is supported by Gaussian [22] and NWChem [23].

Despite their apparent success, these QM/MM methods do not remove the need to perform thermodynamic sampling, but rather allow for such sampling to be done more efficiently. In the next section we will discuss joint density-functional theory, and its polarizable continuum limit, which have the advantage of removing the need for sampling altogether.

1.4 Joint density-functional framework

Joint density-functional theory (JDFT) is a computationally economic alternative to thermodynamic sampling that is based on a rigorous variational principle. As shown by Petrosyan and coworkers [24], the free energy of a solute-solvent system can be exactly described as a functional of the electronic degrees of freedom (of the solute) *and* the mean (i.e. thermodynamically averaged) densities of the solvent nuclei. See Figure 1.1 for a cartoon depiction of the JDFT

representation. Unfortunately, as was the case with the Hohenberg-Kohn functional, the existence proof for this functional does not offer a quick path to constructing the functional itself.

In most implementations of JDFT, the total free energy of the solute-solvent system (A_{tot}) is broken down to three components which are easier to approximate individually,

$$A_{tot}[n(\vec{r}), N_\alpha(\vec{r})] = A_{HK}[n(\vec{r})] + A_{fl}[N_\alpha(\vec{r})] + A_c[n(\vec{r}), N_\alpha(\vec{r})]. \quad (1.5)$$

In the equation above, the first term A_{HK} is the free energy of the explicit, quantum mechanical part of the system (the solute) that is described using Hohenberg-Kohn DFT (hence the subscript).⁴ The second term is the internal free energy of the fluid, which similarly to A_{HK} , depends only on the (mean) nuclear densities $N_\alpha(\vec{r})$ of the nuclear sites making up the solvent molecules. There exists approximations to A_{fl} with greatly varying degrees of sophistication, where A_{fl} can be as simple as an effective surface tension at the interface [25, 26] or as sophisticated as a full-fledged classical density functional theory of the liquid [27]. Finally, the coupling term A_c describes the interaction between solute and solvent. In most approximations, this interaction contains a mean-field Coulomb term and an r^{-6} dispersion (van der Waals) term, and may contain an electron Thomas-Fermi repulsion term corresponding to the natural repulsion when electron clouds of the solvent molecules and the system of interest overlap.

It is possible to classify implementations of JDFT into two broad categories, *explicit* and *implicit*. In the *explicit* approach, the fluid degrees of freedom N_α

⁴ The coordinates of the solute nuclei are assumed to be fixed. The entire functional A_{tot} is minimized (solved) for a given set of *solute* nuclei coordinates. The positions of the solute nuclei can then be minimized in an outer loop to obtain the minimum free energy structure.

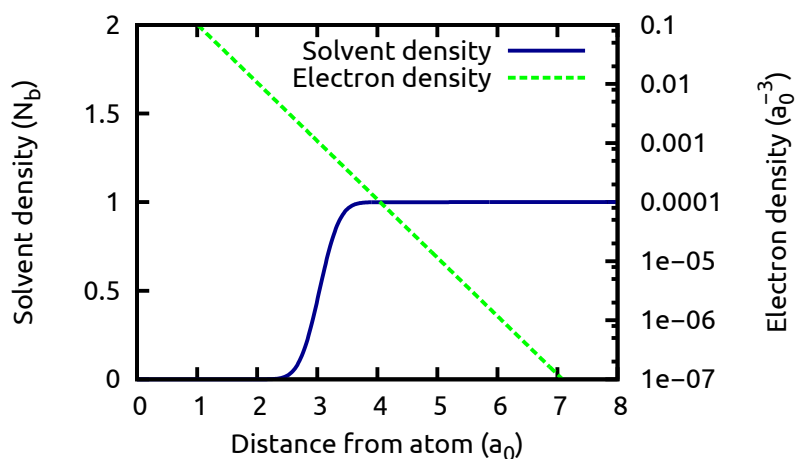


Figure 1.2: The density of the solvent (water) as a function of the distance from a solvated atom. Solvent density is given in units of the bulk density. The green line shows the exponential tail of the solute electron density on a log scale, the blue curve shows the solvent density. The critical solute electron density ($nc = 0.0007$) places the solute-solvent interface ~ 3 bohr from the atomic center.

are included explicitly in the free energy expression as variables in the minimization. In the *implicit* approach, the effects of the fluid degrees of freedom are directly approximated from some property of the solute (usually the electron density). For example, in the implicit approach the fluid density might be computed directly from the solute electron density. (See Figure 1.2 for one example of an implicit solvent model.) Explicit approaches usually feature a smaller number of fitted empirical parameters while the implicit approaches, while more empirical, are often faster and more accurate. Finally, we note that not all approaches can be classified simply into one category or the other. For example, in the nonlinear polarizable continuum model [26], which will be used in several of the later chapters, the fluid density is determined from the solute electron density while the mean orientation of solvent molecules remains an independent variable.

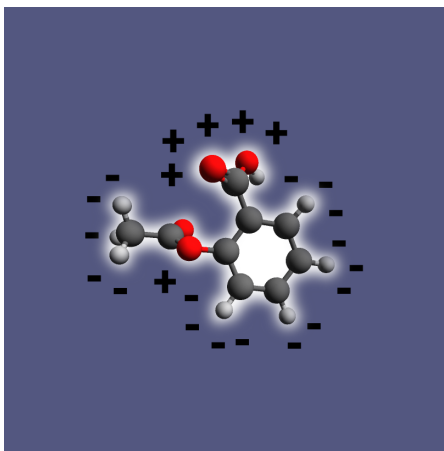


Figure 1.3: The acetylsalicylic acid molecule from Figure 1.1, placed in a polarizable continuum. Bound charges form on the interface.

Such implicit JDFT models may be placed on a rigorous basis as we now show. Integrating out the solvent nuclei from Equation (1.5) gives

$$\begin{aligned}
 A_{tot} [n(\vec{r})] &= \min_{n(\vec{r}), N_\alpha(\vec{r})} (A_{HK} [n(\vec{r})] + A_{fl} [N_\alpha(\vec{r})] + A_c [n(\vec{r}), N_\alpha(\vec{r})]) \\
 &= \min_{n(\vec{r})} \left(\min_{N_\alpha(\vec{r})} (A_{HK} [n(\vec{r})] + A_{fl} [N_\alpha(\vec{r})] + A_c [n(\vec{r}), N_\alpha(\vec{r})]) \right) \\
 &= \min_{n(\vec{r})} \left(A_{HK} [n(\vec{r})] + \min_{N_\alpha(\vec{r})} (A_{fl} [N_\alpha(\vec{r})] + A_c [n(\vec{r}), N_\alpha(\vec{r})]) \right) \\
 &= \min_{n(\vec{r})} (A_{HK} [n(\vec{r})] + \Delta A [n(\vec{r})]),
 \end{aligned}$$

where $\Delta A [n(\vec{r})] \equiv \min_{N_\alpha(\vec{r})} (A_{fl} [N_\alpha(\vec{r})] + A_c [n(\vec{r}), N_\alpha(\vec{r})])$ captures rigorously and exactly all the effects of the fluid implicitly without any reference to N_α . In this way the fluid and coupling free energies can be expressed as a function of the solvent electron density alone.

A very simple (but also very powerful) approximation towards an implicit JDFT is the polarizable continuum model (PCM). Here, the effects of the solvent molecules are replaced with an effective dielectric continuum. See Figure 1.1 for an illustration. The figure dielectric polarizes in response to the partial charges

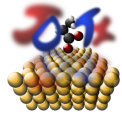
	Software Package	Developed in	License	Basis Set
	JDFTx	C++ & CUDA	GPL3	PW
	Quantum Espresso	Fortran	GPL2	PW
	WIEN2k	Fortran	Commercial	LAPW
	abinit	Fortran	GPL3	PW
	GPAW	C & Python	LGPL	PW
	VASP	Fortran	Commercial	PW
	Gaussian	Fortran	Commercial	Gaussians
	NwChem	Fortran	ECL 2.0	Gaussians

Table 1.2: Popular electronic structure codes [30, 31, 32, 33, 34, 35, 22, 23]. PW is an abbreviation for plane-waves and LAPW is an abbreviation for linearized augmented planes waves.

on the solute and bound charges form on the solute-solvent interface (see Figure 1.3 for a cartoon depiction). A detailed review of PCMs can be found in references [26, 28], as well as in the later chapters of this thesis. In earlier versions of the polarizable continuum model, the dielectric response was assumed to be local and linear [24], but in more recent years nonlinear [26] and/or nonlocal [29] dielectric response models have also been developed.

1.5 Implementations of (solvated) electronic structure methods

Density-functional theory and quantum mechanical solvation models have been implemented in a wide range of free and commercial software packages. Table 1.2 lists several of the popular choices. An important distinction between different software packages is the basis set(s) they use, which also affects the way core electrons are treated in the calculation. There are two types of basis sets that largely dominate modern implementations, namely plane waves and atom-centered gaussians. In the plane wave community, the electronic wave functions are expanded as a sum of plane waves ($e^{-\vec{G}\cdot\vec{x}}$), whereas in the gaussian basis set community, the wave functions are expanded as a sum of atomic orbitals (Gaussians) centered on each atom. Plane waves are the more natural choice when the electrons are delocalized (e.g. in metals) whereas atomic orbitals are more natural when the electrons are localized on atoms (e.g. core electrons, molecules).

Because plane-waves, unlike gaussian orbitals, have uniform real-space resolution, they are ill-suited to describe the electronic wave functions near the atomic cores. The wavefunctions near the core regions are sharply peaked and oscillate to maintain orthogonality with respect to each other. A plane-wave basis set with a resolution sufficient to resolve this region would demand extremely high computational resources. Therefore, most implementations of density-functional theory make use of the pseudopotential approximation, where the core electrons are removed from the calculation but their overall effect is built into the ionic *pseudo*-potentials. Furthermore, the wave functions of valence electrons, even though they remain in the calculation, have their core regions smoothed and their oscillations removed. Such pseudo-potentials, now

Atomic density: Ni

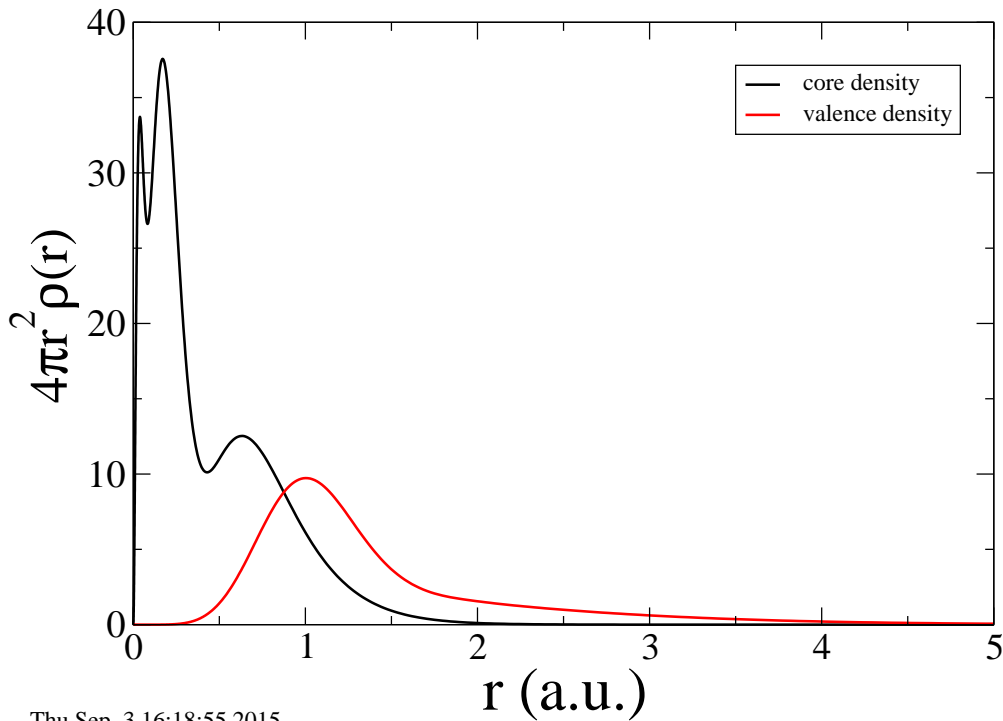


Figure 1.4: The core and valence densities of the nickel. The valence states are 3d, 4s and 4p. Figure generated with the Opium pseudopotential generator [37].

standard in plane wave codes, are largely unnecessary in Gaussian basis sets. In Table 1.2, Wien2k [32] is an outlier in that it is a plane-wave code that does not make use of the pseudopotential approximation. Instead, it makes use of the LAPW method (linearized augmented plane wave) where the wave functions near the atomic cores are expanded as a product of radial functions and spherical harmonics which are then matched to the plane waves at some boundary [36].

Figures 1.4 and 1.5 illustrate the pseudopotential approximation using an

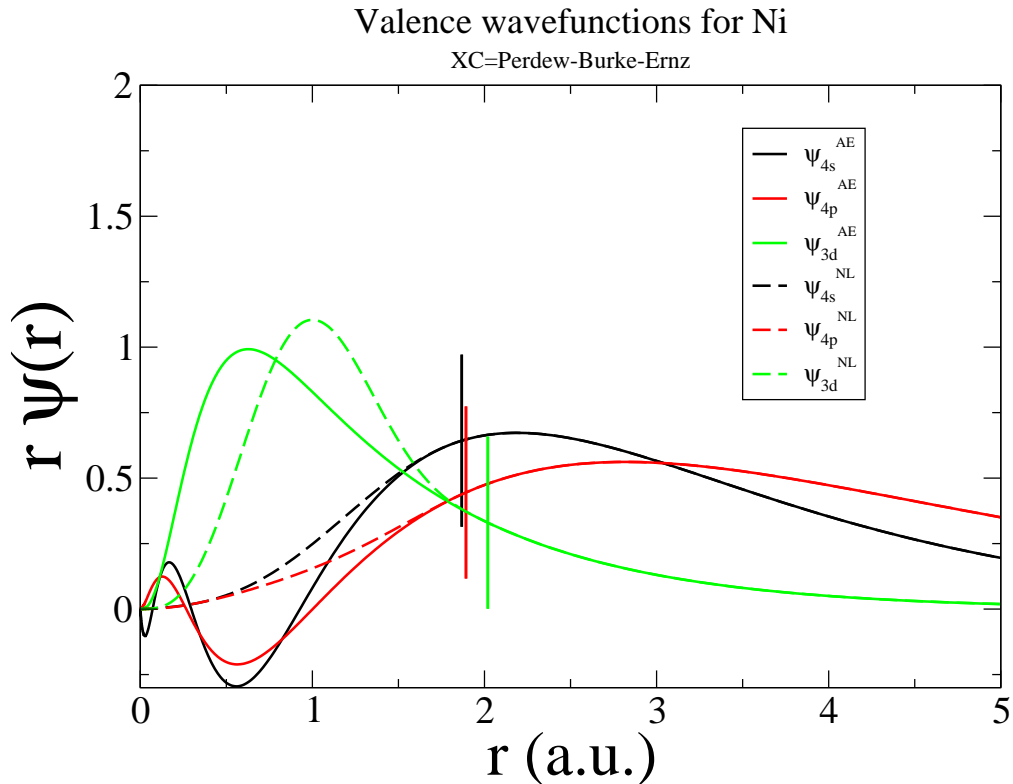


Figure 1.5: The valence Kohn-Sham orbitals (3d, 4s and 4p) of the nickel. Solid lines are all-electron orbitals and dashed lines are the pseudized (smoothed) orbitals. Vertical lines show the core radii, beyond which pseudized and all-electron orbitals must agree. nickel pseudopotential generated with the Opium pseudopotential generator [37].

atom of nickel. Plotted in Figure 1.4 is the radial charge density ($4\pi r^2 \rho(\vec{r})$). It can be seen from the figure that there are different peaks for each electronic shell. The first two peaks, corresponding to 1s and 2s shells, are clearly on a different length-scale than the valence charge density plotted in red. Therefore, any uniform rectilinear grid that is sufficiently fine to resolve those 1s and 2s shells will be unnecessarily fine for the valence electrons. Furthermore, as seen in Figure 1.5, the 4s and 4p valence orbitals themselves oscillate near the core to main-

tain orthogonality with the lower indexed s and p orbitals (no such oscillations are needed for 3d as there are no 1d or 2d orbitals). As there is kinetic energy in these oscillations, they are important but also expensive to resolve. The pseudized orbitals on the other hand, have been smoothed in the core regions, which greatly reduces the number of basis elements (or real-space grid points) needed to represent them, in addition to removing the need for calculating large numbers of nearly completely inert core electrons.

A highly active and potentially transformative field of research is the development of linear-scaling density-functional theory codes [38, 39, 40]. In most calculations, whether they are done using plane waves or gaussian orbitals, the total run time scales as $O(N^3)$ where N is the number of electrons in the system (the pseudopotential approximation itself also doesn't change the scaling of the problem, but it reduces N and the prefactor). The cubic scaling comes from the fact that there are N Kohn-Sham orbitals, each of which has the dimensions of volume (which itself usually scales linearly with the number N of electrons). The need to maintain orthonormality between these Kohn-Sham orbitals necessitates the calculation of N^2 dot products of the form $\langle \phi_j | \phi_k \rangle$ each of which requires a sum over the basis functions and thus introduces an additional factor of N , pushing up the total cost to $O(N^3)$ [39]. As discussed earlier, one way around this problem is to develop density-only kinetic energy approximations which would remove the need for Kohn-Sham orbitals altogether. But in the absence of such functionals, other ways to tackle this problem must be found. One method is to work with a transform which localizes the wave functions themselves (as with Wannier functions [41]), so that the dot products involving most basis elements evaluate to essentially zero and thus only $O(N)$ dot products need to be calculated. Throughout this thesis, we will use density-functional theory

implementations that scale as $O(N^3)$. However, development of $O(N)$ methods are very relevant to the study of liquids and solvated systems. If such methods develop further, they may be used to efficiently perform ab initio molecular dynamics simulations of liquids, and thus provide very effective testbeds for the approximations used within JDFT. However, even if $O(N)$ methods are successfully developed, JDFT will nevertheless continue to scale more efficiently than molecular dynamics because it eliminates the need for statistical sampling and gives thermodynamic averages directly.

CHAPTER 2

TOWARDS A UNIVERSAL ISO-DENSITY POLARIZABLE CONTINUUM MODEL FOR MOLECULAR SOLVENTS IN PLANE-WAVE DFT

Ab initio methods, in particular density-functional theory, have a well established record of significant impact in chemistry, physics and materials science [42]. However, despite the fact that many chemical reactions occur in a liquid environment where the solvent (or electrolyte) plays an important role in the chemistry, applications of density-functional methods to liquid and solvation chemistry has lagged behind applications to solids, gas-phase molecules, or surfaces in vacuum. This is because a single configuration of liquid molecules is often not representative of the thermal average, and thermodynamic sampling, done for instance with *ab initio* molecular-dynamics[43] or QM/MM[20], is needed to carry out realistic calculations.

Polarizable continuum models (PCMs) [44, 28, 45, 46, 47, 48, 25, 49, 50, 51, 52] are one class of approximations where the solvent effect is reproduced with an effective dielectric description of the liquid environment, thus removing the need for sampling and thermodynamic integration and providing an economic alternative to molecular dynamics. Continuum solvation models that use the union of spheres approach to construct the solute cavity, in particular the universal "SMx" series[45, 46, 47] and those developed by Tomasi and coworkers,[44, 28] have been very successful for a wide variety of solvents and widely implemented in quantum chemistry software using gaussian basis sets. An alternative approach is the iso-density PCM [48, 25, 49, 50, 51, 52], which is usually preferred in the plane-wave community and uses the solute electron density to construct the solute cavity. Such iso-density models also have

achieved significant success describing processes in aqueous environments, including predicting, among other things, solvation energies for molecules [50, 25] and ions [51, 52], optical spectra for solvated molecules [53] as well as interfacial capacitances and potentials of zero charge for crystalline metals [49]. Successful application of iso-density methods have great potential for new discoveries in many areas of research, especially in energy-material related technologies[54] where the processes at solid-liquid interfaces are of prime importance and can most easily be studied in a plane-wave context.

Despite much recent interest [25, 51, 55], one important obstacle is that most iso-density PCMs [24, 25, 48, 55, 51] are parametrized for only a handful of solvents (primarily water), and parameters don't exist for many solvents commonly encountered in organic chemistry and electrochemistry. There has been much progress in reducing empiricism and increasing the generality of such models[25, 50], but such approaches continue to require that multiple solvent-dependent parameters be fit to experimental data sets, typically to solvation free-energies of molecules.

While a great deal of solvation data is available [56, 57, 58, 59] for common solvents (such as water, chloroform and carbon tetrachloride), many solvents of technological relevance do not have sufficient published data from which to construct iso-density continuum models. To aid exploration of microscopic physical processes in general solvent environments *and particularly studies to identify the best solvent for a given application*, this work provides a general framework for constructing accurate iso-density models for a large class of solvents, similar in spirit to the way SMx models[45, 46, 47] have been made universal. We use a limited number of coefficients, all of which can be derived directly

either from bulk thermodynamic data that is generally easy to obtain *or* from relatively simple single-molecule *ab initio* calculations.

2.1 Electrostatic contributions

Polarizable continuum models represent a class of approximate theories which treat the interaction with the fluid environment as the dielectric response of a continuum medium filling the space not occupied by the molecule or surface of interest, to which we refer hereafter generically as the “solute”. For most solvents, the dielectric response of the fluid is the largest, but not necessarily the entire, contribution to the free energy of solvation. Many models [48, 25, 49] assume that the dielectric response of the fluid is linear; but this need not be so. Indeed, in this work, we use the nonlinear dielectric response function of Gunceler et. al. [50], which also includes the rotational dielectric saturation of polar solvents. Continuum solvation models generally model the remaining, non-electrostatic contributions to the free energy as related to the total area of the solute-solvent interface, treated independently of the underlying dielectric response model. The central ideas in this paper thus apply equally well to linear response models, should one desire to work with those instead.

The first key issue in development of a PCM is determination of the dielectric region. Traditionally, continuum models filled space with the dielectric medium except for spherical cavities centered on each atom of the solute, each with a species-dependent atomic radius ultimately fit to a database of solvation energies[28]. Several groups, instead, independently developed the isodensity approach for cavity determination [48, 24, 60], where the dielectric function

changes from 1 in the interior of the solute region to the bulk value (ϵ_{bulk}) of the solvent dielectric constant, with the transition occurring on the surface of a critical cutoff n_c of the solute electron density. As noted by Petrosyan *et al.*[24], this has the advantage of placing such models in the class of approximate joint density-functionals.

For the functional form of the above transition in the the dielectric response, we here use the functional form of Petrosyan *et al.* [24],

$$\epsilon(\vec{r}) = 1 + (\epsilon_b - 1) s(n(\vec{r})), \quad (2.1)$$

where $s(n(\vec{r}))$ is the cavity-shape function,

$$s(n(\vec{r})) = \frac{1}{2} \operatorname{erfc} \frac{\log(n(\vec{r})/n_c)}{\sigma \sqrt{2}}. \quad (2.2)$$

The parameter σ , controlling the width of the transition, is chosen to be large enough to resolve the transition on typical real-space grids. (Here, we employ $\sigma = 0.6$ as chosen by Petrosyan and coworkers[24].) By replacing atom-dependent fit parameters with a single critical electron density n_c , which can then be fit to a database of solvation energies for each solvent considered, such iso-density approaches[48, 24, 60] thereby eliminate many fit parameters in favor of a single parameter. However, the remaining cutoff parameter n_c is highly solvent dependent, varying over several orders of magnitude, and it's determination still requires access to a database of solvation energies for each new solvent considered.

Linear polarizable continuum theories describe the dielectric constant of space through

$$\epsilon(\vec{r}) = 1 + (\epsilon_b - 1) s(n(\vec{r})), \quad (2.3)$$

where ε_b is the bulk dielectric constant of the solvent. The main advantage which such theories offer is conceptual and operational simplicity. However, we have shown [50] that these models can be highly inaccurate and produce unphysical results in systems where the microscopic electric fields are strong. In such systems, the rotational response of solvent molecules saturate quickly, giving rise to a much weakened electrostatic response to further increases in the electric field, a phenomenon completely missed by such linear theories.

To capture such saturation effects, in the nonlinear theories ¹, the response of the system is treated as though originating from a collection of "point molecules", whose density is given by

$$N[s(\vec{r})] = N_b s(\vec{r}),$$

where N_b is the bulk number density of the solvent. Under an external electric field, the fluid molecules not only rotate to align with the external field, they also polarize further. In this picture, the total electrostatic contribution to the free energy is then given by

$$A_\varepsilon = A_{pol} + A_{rot} + \int \frac{(n(\vec{r}) + n_{nuc}(\vec{r}) + \frac{1}{2}n_b(\vec{r}))n_b(\vec{r})}{|\vec{r} - \vec{r}'|} \quad (2.4)$$

where A_{pol} and A_{rot} are the (polarization and rotation) internal energies of the solvent, $n(\vec{r}) + n_{nuc}(\vec{r})$ is the total charge (electronic and nuclear) of the solute, $n_b(\vec{r})$ is the bound charge induced in dielectric, and the factor of 1/2 avoids double counting the interaction of the bound charge with itself.

The internal energy corresponding to polarizations is given by

$$A_{pol} = \int d^3r N(\vec{r}) \frac{1}{2} \chi |\vec{P}_{pol}(\vec{r})|^2, \quad (2.5)$$

¹The discussion on the nonlinear theory follows the one presented by Gunceler et. al. [50]

where $\vec{P}_{pol}(\vec{r})$ represents the induced polarization and χ is the molecular polarizability.

The above theory for the polarization response is equivalent to a linear dielectric. The nonlinearity in the theory is in the rotational part below. For rotations, the internal energy is given by

$$A_{rot} = \int d^3r kT N(\vec{r}) \left[\int \frac{d\Omega}{4\pi} \hat{e} p_{\hat{e}} \log p_{\hat{e}} - l(\vec{r}) \left(\int \frac{d\Omega}{4\pi} p_{\hat{e}} - 1 \right) - \frac{\alpha \vec{P}_{rot}^2(\vec{r})}{2} \right], \quad (2.6)$$

where \hat{e} is the unit vector, $d\Omega$ is the unit solid angle over a sphere, $p_{\hat{e}}$ is the probability of finding a solvent particle pointing in the direction \hat{e} , $l(\vec{r})$ is the Lagrange multiplier enforcing unit normalization for probabilities, α is a correlation correction discussed below and $\vec{P}_{rot}(\vec{r})$ is the average dipole density given by

$$\vec{P}_{rot}(\vec{r}) = p_{mol} \int \frac{d\Omega}{4\pi} \hat{e} p_{\hat{e}}.$$

In the above equation, p_{mol} is the permanent dipole of a single solvent molecule in solution.

In equation 2.6, the first term inside the integral is the rotational entropy of solvent molecules. The second term is a constraint enforcing unit normalization for probabilities $p_{\hat{e}}$. The last (third) term with the constant α is the correlation term. In equation 2.4, the interactions between solvent molecules are handled through the mean field coulomb term without any regard to the correlations between them. The last (third) term in equation 2.6 is a *local dipole density approximation* (LPDA) to the correlations between solvent dipoles, and plays a role analogous to the one played by the local density approximation (LDA) in electronic DFT. Later, we will determine constant α by constraining the model to reproduce the bulk dielectric constant of the solvent.

The free energy functional described above admits solutions for $p_{\hat{e}}$ of the form $e^{\vec{\epsilon}(\vec{r}) \cdot \hat{e}}$, where $\vec{\epsilon}$ is some vector field related to the local electric field. After eliminating $\vec{P}_{\text{pol}}(\vec{r})$, $\vec{P}_{\text{rot}}(\vec{r})$ and $l(\vec{r})$ in favor of $\vec{\epsilon}(\vec{r})$, for the total electrostatic internal energy, we get

$$A_{\text{pol}} + A_{\text{rot}} = \int d^3r kT N(\vec{r}) \left[\epsilon^2 \left(f(\epsilon) - \frac{\alpha}{2} f^2(\epsilon) + \frac{X}{2} (1 - \alpha f(\epsilon))^2 \right) - \log \frac{\sinh \epsilon}{\epsilon} \right]. \quad (2.7)$$

In the above expression, $f(\epsilon) = (\epsilon \coth \epsilon - 1)/\epsilon^2$ is the effective dimensionless rotational susceptibility and $X \equiv \chi T/p_{\text{mol}}^2$ is its linear counterpart. The bound charge induced in this nonlinear dielectric is given by

$$\rho_{\epsilon}(\vec{r}) = -\vec{\nabla} \cdot [p_{\text{mol}} N_b s(\vec{r}) \vec{\epsilon} (f(\epsilon) + X(1 - \alpha f(\epsilon)))]. \quad (2.8)$$

The parameters α and X are constrained so that the theory reproduces the known dielectric response of the solvent. In the high-field limit, the rotations should "freeze out" and the theory should recover the high field dielectric constant ϵ_{∞} . In practice, this value can be approximated as the square of the refractive index, as rotations are too slow to respond at optical frequencies. In contrast, in the low-field limit, the theory should reproduce the static bulk dielectric constant ϵ_b of the solvent. In light of this, we find that X and α are given by

$$X = \frac{T(\epsilon_{\infty} - 1)}{4\pi N_b p_{\text{mol}}^2} \quad \text{and} \quad \alpha = 3 - \frac{4\pi N_b p_{\text{mol}}^2}{T(\epsilon_b - \epsilon_{\infty})}. \quad (2.9)$$

The last missing piece in the electrostatic part of the theory is the determination of p_{mol} . One approach is to calculate the dipole moment of a solvent molecule in vacuum. However, there is no reason why the average dipole moment of a solvent molecule in liquid phase should be the same as the one in gas phase. Indeed, later in the chapter (Table 2.3), we will see that is not the case.

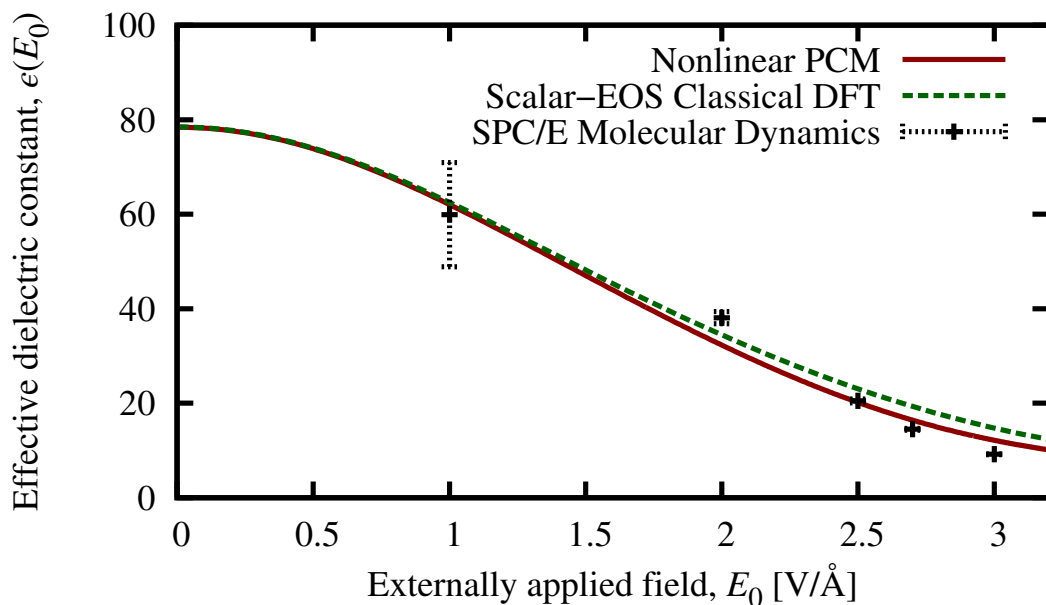


Figure 2.1: The effective dielectric constant of the nonlinear continuum theory [50] (with H_2O parameters) at different electric fields. SPC/E molecular dynamics and classical density-functional results are also plotted for comparison.

Instead, for each solvent, we calculate p_{mol} self-consistently by placing a single solvent molecule in a nonlinear polarizable continuum description of the same solvent.

The dielectric response function of water, calculated with the nonlinear theory, is plotted in Figure 2.1 as a function of the electric field. As expected, the effective dielectric constant decreases with increasing electric field. The values calculated from the nonlinear theory agree very well with the values calculated from more complex classical density-functional theories [27] or from SPC/E molecular dynamics simulations [61].

It is also important to understand when, if at all, rotational nonlinearity is

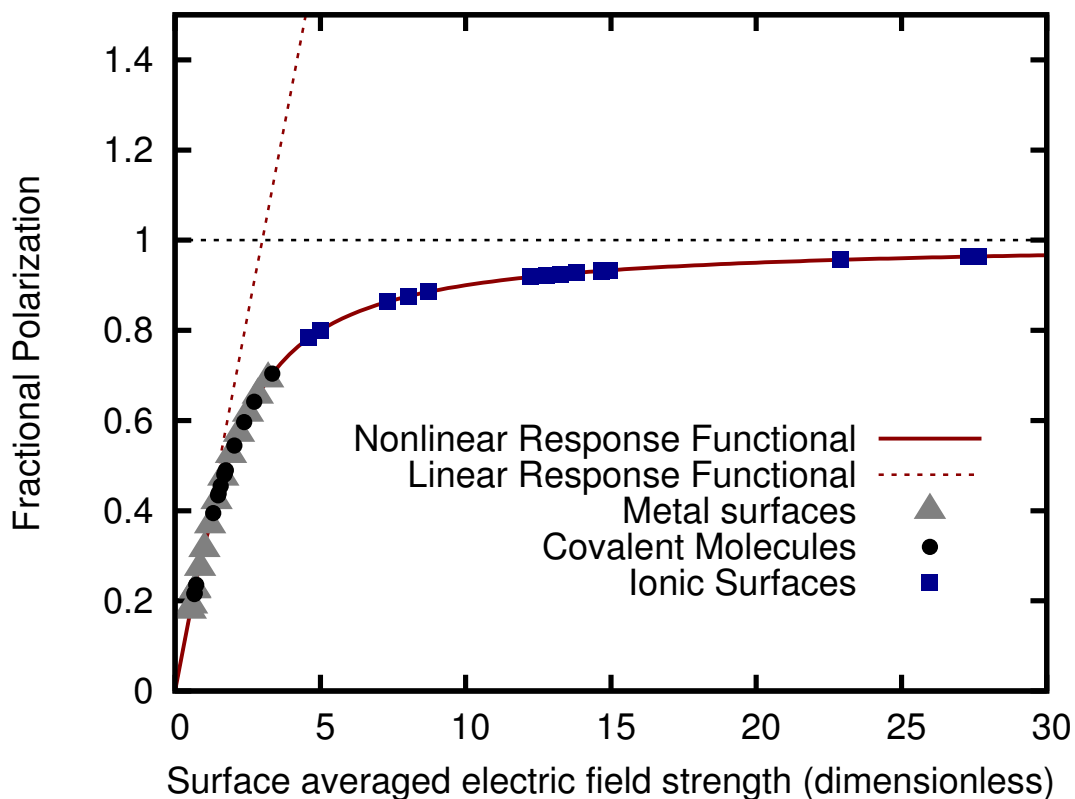


Figure 2.2: Fractional polarization at the solute-solvent interface as a function of the dimensionless effective field ϵ , solvated molecules (circles), charged metal surfaces (triangles) and ionic surfaces (squares).

significant. This is explored in detail in Figure 2.2. Plotted there is the fractional polarization ($\langle R \rangle$, on the y-axis) as a function of the surface averaged electric ($\langle \epsilon \rangle$, on the x-axis). These are calculated in the following way:

$$\langle \epsilon \rangle = \left| \int d^3r \frac{|\vec{\nabla}_s(\vec{r})|}{A} \vec{\epsilon}(\vec{r}) \right| \quad (2.10)$$

and

$$\langle R \rangle = \int d^3r \frac{|\vec{\nabla}_s(\vec{r})|}{A} \frac{\vec{P}_{rot}(\vec{r})}{p_{mol}}, \quad (2.11)$$

where

$$A = \int d^3r |\vec{\nabla}_s(\vec{r})| \quad (2.12)$$

is the total area of the solute-solvent interface. For the fractional polarization $\langle R \rangle$, a value of unity means that all solvent dipoles are aligned and point towards the same direction whereas a value of zero means that the dipoles point in random directions.

We repeat this calculation for 3 different kinds of systems. First is a set of neutral, covalently bonded organic molecules, discussed later in this chapter (black circles in Figure 2.2). Next are the surfaces of noble metals (gold, platinum and silver) charged up to ± 1 V from their respective potentials of zero charge (gray triangles in Figure 2.2). And last are the surfaces of lithium solid-electrolyte interface materials, to be studied in more detail in the next chapter (blue squares in Figure 2.2). These lithium surfaces are ionic oxides and hydroxides where the polarity of the surface gives rise to very strong electric fields at the interface.

We see in Figure 2.2 that for most molecules and metallic surfaces, the linear response approximation performs well, with only the most polar molecules and metal surfaces with the highest charge showing noticeable nonlinearities. However, for surfaces of ionic crystals, the electric fields are too strong to describe the response with a linear response approximation.

2.2 Non-electrostatic terms in implicit solvation theory

Even beyond the fitting needed to determine n_c , additional key parameters must be determined to yield accurate solvation energies. This is because significant non-electrostatic processes contribute to solvation, such as the dispersion interaction between the solute and solvent, as well as the free-energy associated

with forming the solute cavity in the solvent. This is particularly true for non-aqueous solvents like chlorform and carbon tetrachloride, where solvation energies are not dominated by electrostatic interactions[62]. To capture these effects, the effective surface-tension approximation is commonly used in the iso-density PCM context [25, 50]. It approximates the *non-electrostatic* contributions to the solvation energy (E_{ne}) as

$$E_{ne} = \tau_{\text{eff}} \int d^3r |\vec{\nabla}s|, \quad (2.13)$$

where τ_{eff} is an effective surface tension and the integral represents the surface area of the solute. This particular use of the shape function to calculate the surface area is a special case of the co-area formula in geometric measure theory [63], and is similar in spirit to the way surface areas are calculated in level-set theory [64]. For solvents with high bulk surface tension (such as water), the *effective* surface tension generally is positive, whereas, for a large number of non-polar and weakly polar solvents with weak bulk surface tensions and strong (attractive) dispersion interactions, these *effective* surface tensions can become negative.

2.3 Universal solvation model for molecular solvents

Motivated by the aforementioned trend of the effective surface tension with the strength of dispersion interactions, we now consider whether there exists a simple, approximate universal correlation between these two quantities. To begin, we separate out the bulk surface tension, as suggested independently by Dupont and coworkers [51], and write $\tau_{\text{eff}} = \tau_{\text{bulk}} + \tau'$, where τ_{bulk} is the (generally available) bulk surface tension of the solvent and τ' is a correction term, which we will now attempt to correlate with dispersion interactions. Next, to

characterize the strength of the dispersion interactions, we make use of a very simple model (not to be taken literally as a quantitative model) and consider a self-solvation scenario where the van der Waals r^{-6} potential has been integrated in a region outside twice the van der Waals radius of the solvent molecule, resulting in a dispersion energy per unit area $E_{\text{vdw}}/A \equiv \tau_{\text{vdw}}$ of

$$\tau_{\text{vdw}} = \frac{s_6}{A} \int_{2R_{\text{vdw}}}^{\infty} 4\pi r^2 dr N_b \frac{\sum_j C_6^{(j)}}{r^6} = \gamma_1 \frac{N_b C_{\text{solv}}}{R_{\text{vdw}}^5} \quad (2.14)$$

where we employ the pair-potential model of dispersion corrections introduced by Grimme[65]. Here, $C_{\text{solv}} = \sum_j C_6^{(j)}$ is the effective dispersion coefficient, and is computed by summing over the Grimme C_6 coefficients of all atoms in the solvent molecule. N_b is the bulk number density of the solvent, R_{vdw} is a measure for the size of the solvent molecule (explained more detailed in the next paragraph) and s_6 is a dimensionless scale factor accounting for renormalization of the fluctuating dipole interaction by multiple-atom interactions. In equation 2.14, we absorb s_6 and all other dimensionless constants into γ_1 . (See below for a more detailed exploration of s_6 .) Finally, if desired, one can view the final expression as a simple dimensional analysis requiring some characteristic size of the solvent molecule, which we take to be the van der Waals radius.

To determine the van der Waals radius (R_{vdw}), one could use the volume of exclusion in the van der Waals equation of state for the gas phase, but such data is not available for all solvents. Instead, we define a DFT volume of exclusion

$$V \equiv \int (1 - s) d^3r \equiv (4\pi/3)R_{\text{vdw}}^3 \quad (2.15)$$

using the cavity shape function $s(\vec{r})$, but now with n_c set to $n_{\text{vdw}} = 1.83 \times 10^{-4}$ bohr $^{-3}$, which we obtained by fitting to van der Waals radii which are available in the literature[66, 67]. The results, which show good agreement with literature, are given in figure 2.3.

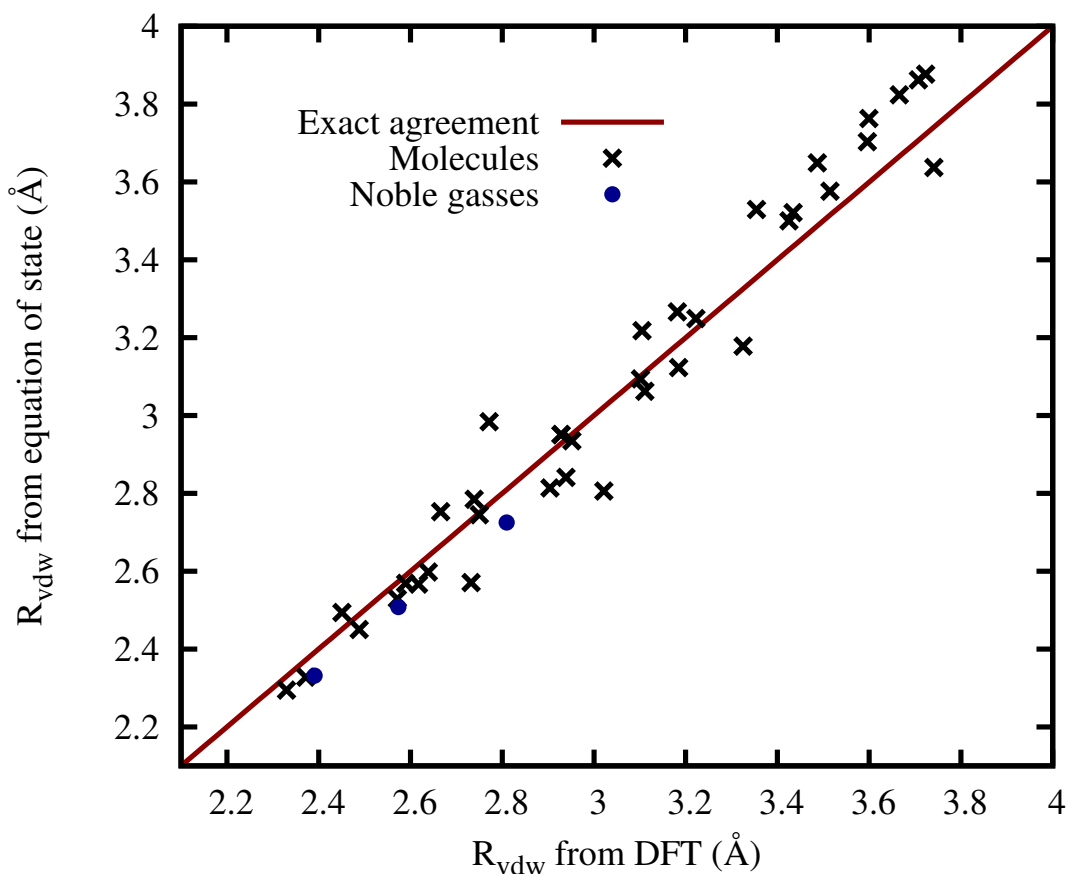


Figure 2.3: Van der Waals radius, as determined using the equation of state for the gas phase versus result from density-functional theory procedure described in the text.

With all of the parameters in equation 2.14 defined, we next test our correlation hypothesis. We begin by employing the standard technique of deriving solvation model parameters from fits to solvation databases. These fits allow us to determine the effective surface tension (τ_{eff}) for each of the six solvents in figure 2.4.

Figure 2.4 shows that there indeed is a strong correlation between the correction term $\tau' = \tau_{\text{eff}} - \tau_{\text{bulk}}$ and our measure of dispersion strength $N_b C_{\text{solv}} / R_{\text{vdw}}^5$.

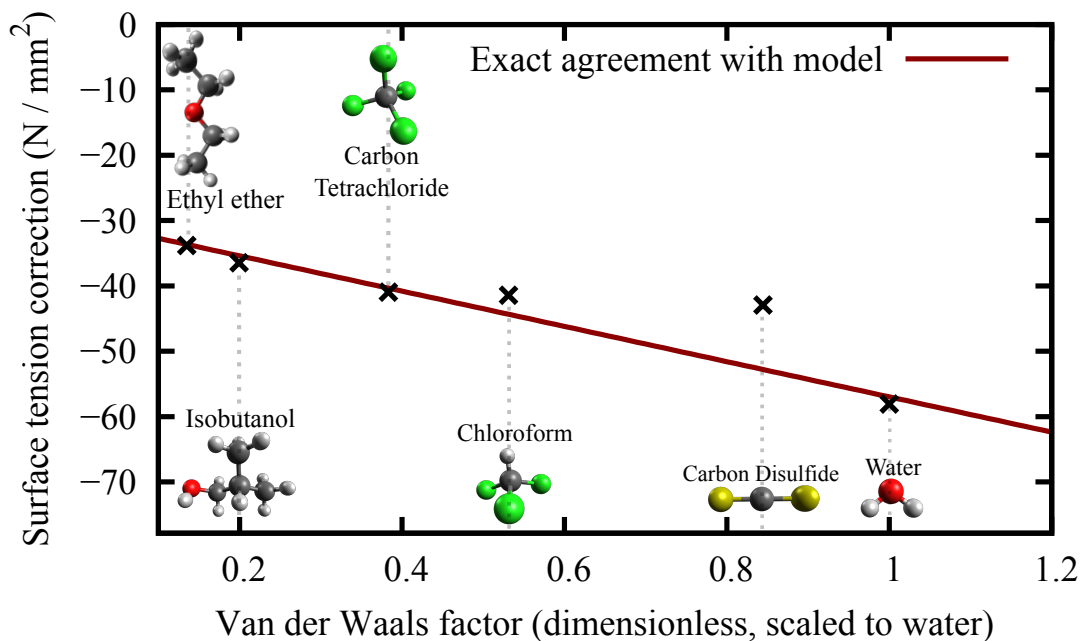


Figure 2.4: Surface tension correction ($\tau' = \tau_{\text{eff}} - \tau_{\text{bulk}}$) as a function of van der Waals factor $N_b C_{\text{sol}} / R_{\text{vdw}}^5$ (scaled to that of water to provide a dimensionless quantity for display purposes): data from fits to experimental solvation energies [56, 57, 58, 59] (black x's), best-fit linear correlation in the form of equation 2.14 (red line).

Solvents	Best fit			Vapor constrained		
	n_c (a_0^{-3})	τ_{eff} (E_H/a_0^{-2})	RMS Error (kcal/mol)	n_c (a_0^{-2})	τ_{eff} (E_H/a_0^{-2})	RMS Error (kcal/mol)
Water	1.0×10^{-3}	9.50×10^{-6}	0.95	9.0×10^{-4}	1.02×10^{-5}	1.38
Chloroform	2.4×10^{-5}	-9.23×10^{-6}	0.82	5.6×10^{-4}	-1.11×10^{-5}	1.30
Carbon tetrachloride	1.2×10^{-4}	-8.99×10^{-6}	1.02	2.9×10^{-4}	-8.61×10^{-6}	1.21
Isobutanol	1.5×10^{-3}	-8.96×10^{-6}	0.76	1.8×10^{-3}	-8.28×10^{-6}	0.83
Carbon disulfide	2.9×10^{-5}	-7.96×10^{-6}	1.01	3.4×10^{-4}	-1.32×10^{-5}	2.32
Ethyl ether	2.6×10^{-4}	-1.08×10^{-5}	1.13	5.0×10^{-4}	-1.12×10^{-5}	1.35
	Average of RMS errors: 0.95			Average of RMS errors: 1.40		
	$\gamma_0 = -1.927 \times 10^{-3} E_H/a_0^{-2}$			$\gamma_1 = -1.313 \times 10^{-2}$		

Table 2.1: PCM parameters and RMS errors for the solvents used in the determination of the values for γ_0 and γ_1 .

The only apparent outlier in the fit set is CS_2 , whose anomolous behavior we suspect is related to its being the only molecule in the fit set which has no net dipole moment while simultaneously having a significant non-zero quadrupole moment. The case of ethylene glycol, another solvent with the same characteristic, we explore in detail later in the paper.

Based on the above observations, we propose as an empirical model the following approximate universal form for the effective cavity tension

$$\tau_{\text{eff}} = \tau_{\text{bulk}} + \gamma_0 + \gamma_1 \left[\frac{N_{\text{b}} C_{\text{solv}}}{R_{\text{vdw}}^5} \right], \quad (2.16)$$

where the first term τ_{bulk} is the bulk surface tension of the solvent and is a measure of the energy cost to form macroscopic cavities in the liquid, the second term $\gamma_0 \equiv -1.927 \times 10^{-5} E_{\text{H}}/a_0^{-2}$ is a microscopic correction corresponding to the vertical intercept of the linear correlation, and the final term ($\gamma_1 \equiv -1.313 \times 10^{-2}$) incorporates the effects of long-range dispersion as the slope of the correlation. Figure 2.4 illustrates our best fit values for γ_0 and γ_1 and compares the resulting linear model values for τ_{eff} with those which came from the original data-set fits, showing that we indeed can predict quite well appropriate values for this parameter without additional fitting to solvation data whatsoever.

Regarding the magnitude of our slope fit parameter γ_1 , comparing equations 2.14 and 2.16, we are able to extract from our fit a measure of the Grimme van der Waals scale factor, $s_6 = 32 \times 3 \times \gamma_1 = 1.26$. To place this value for s_6 in context, we note that, in the Grimme framework[65], this parameter is generally fit to account first for the fact that some of the dispersion interaction (the short-range part) is accounted in standard approximate exchange-correlation functionals and, second, for the fact that a pair-potential model for the van der Waals interaction misses multiple molecule interactions. In theory, the s_6 pa-

parameter would have a value of unity, but is known to change by as much as 45 % between different electronic exchange-correlation functionals[65], placing our fit result squarely in the expected range.

In addition to the readily available bulk surface tension τ_{bulk} , only three solvent-dependent quantities are required to determine τ_{eff} , namely the bulk number density of the solvent N_b (readily available from bulk thermodynamic data), the effective Van der Waals coefficient C_{solv} (computed by summing the readily available and tabulated [65] atomic static dipole polarizabilities), and the effective Van der Waals radius of the solvent R_{vdw} , which can be obtained using simple *ab initio* calculations as described above.

With the non-electrostatic contributions now determined, we need only to define the electrostatic contributions to complete our model. For these electrostatic interactions, we employ the non-linear dielectric response model of Gunceler et al[50]. In addition to n_c , this model requires solvated dipole moments, which we have determined self-consistently within our model fluids using the procedure outlined immediately aforementioned work [50]. The numerical results for these dipole moments are given in table 2.3. Finally, to determine n_c , rather than employing a database of solvation energies, we fit the model for each fluid to a single experimentally determined datum, the self-solvation energy, which can be easily determined from the vapor pressure[68], which is generally much more readily available than tabulated solvation energy data. The resulting numerical values for n_c for the six solvents in our training set are reported in table 2.1; whereas the values for additional solvents of technological importance, are reported in table 2.2.

Solvents	$n_c (a_0^{-3})$	$\tau_{\text{eff}} (E_H/a_0^{-2})$	RMS Error (kcal/mol)
Acetone	8.6×10^{-5}	-4.91×10^{-6}	
Acetonitrile	1.8×10^{-4}	-6.29×10^{-7}	
Dichloromethane	9.3×10^{-4}	-2.74×10^{-6}	0.97
Dimethyl sulfoxide	9.5×10^{-4}	8.42×10^{-6}	2.09
Ethylene carbonate	1.8×10^{-3}	1.55×10^{-5}	
Ethanol	1.3×10^{-3}	-5.10×10^{-6}	1.40
Glyme	8.3×10^{-5}	-8.03×10^{-6}	
Methanol	6.5×10^{-4}	-5.23×10^{-6}	
Propylene Carbonate	9.8×10^{-4}	9.53×10^{-6}	
Tetrahydrofuran	1.6×10^{-3}	-1.69×10^{-6}	1.04
Ethylene Glycol	5.4×10^{-4}	1.15×10^{-5}	see next section

Table 2.2: Parameters for additional solvents of potential interest that were not used in the construction of the model.

	Water	Chloroform	Carbon tetrachloride	Isobutanol
Vacuum	0.727	0.442	0.000	0.627
Liquid	0.940	0.491	0.000	0.646
	Carbon disulfide	Ethyl ether	Acetone	Dichloromethane
Vacuum	0.0	0.409	1.185	0.676
Liquid	0.0	0.487	1.387	0.890
	Ethylene Carbonate	Glyme	Methanol	Tetrahydrofuran
Vacuum	1.929	0.000	0.649	0.720
Liquid	2.674	0.000	0.791	0.909
	Acetonitrile	Dimethyl sulfoxide	Ethanol	
Vacuum	1.581	1.606	0.604	
Liquid	1.892	2.192	0.762	

Table 2.3: Effective dipole moment of solvent molecules in vacuum and liquid phase (calculated self-consistently) All values in atomic units (ea_0).

In figure 2.5, calculated solvation energies for 10 solvents,² of which 4 were not part of the fitting set, are compared with two other solvation models available in the literature. RMS errors in our work are between 0.8-1.4 kcal/mol for most solvents considered, except for two pathological cases that have errors greater than 2.0 kcal/mol. The coefficient of determination, a standard measure of predictive power, is 0.76. Solvation energies calculated with our approach are competitive with but somewhat worse than SMD[47], a commonly used

² The 10 solvents are: Carbon tetrachloride, Chloroform, Carbon disulfide, Dimethyl sulfoxide, dichloromethane, ethanol, ethylene glycol, ethyl-ether, isobutanol and tetrahydrofuran.

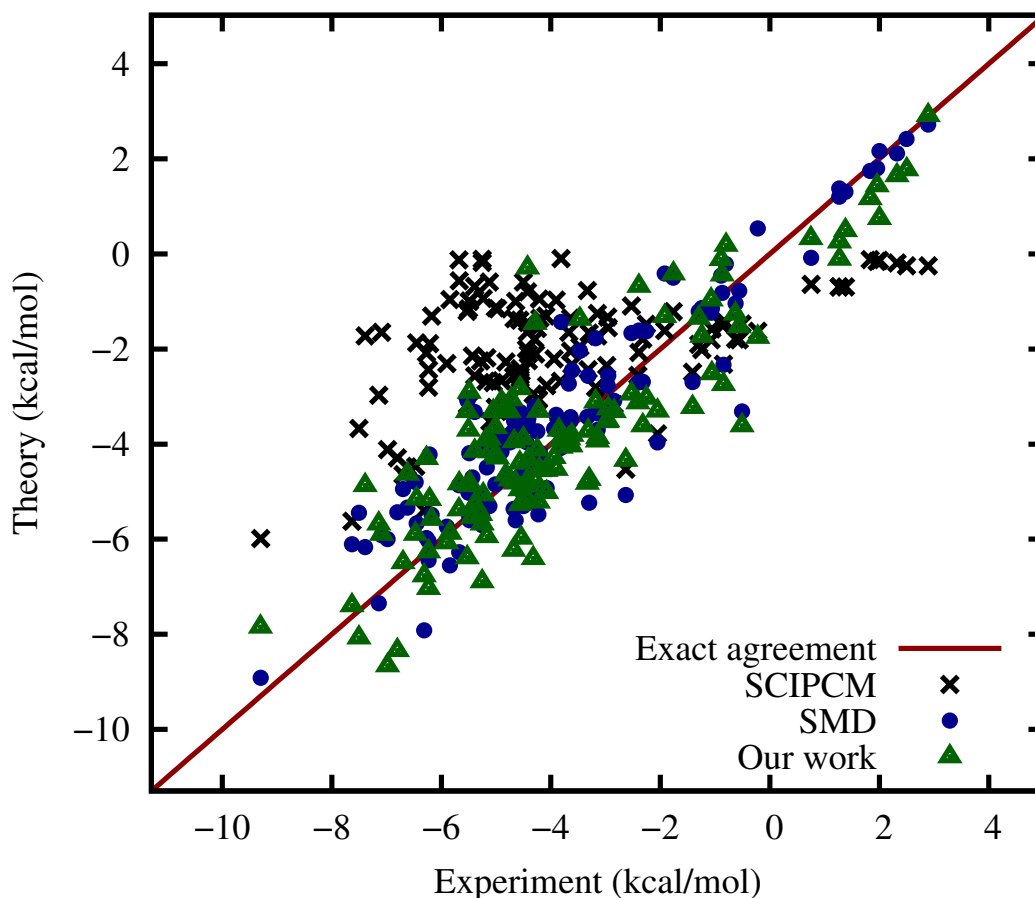


Figure 2.5: Theoretical versus experimental solvation energies for 124 solutes in 10 solvents computed in three theories: SMD[47], SCIPCM[69], and our work.

and very successful solvation model that uses the union-of-spheres approach for determining cavities. (SMD has RMS errors between 0.6-1.7 kcal/mol and a coefficient of determination of 0.83 for the same set of solvents and solutes.) An interesting observation is that even though both theories tend to undersolvate, SMD has a slightly larger bias (mean error 0.296 kcal/mol) than our work (mean error 0.027 kcal/mol), which might be due to the large number of polar solutes in our training set. SCIPCM[69], another iso-density model that shares some traits with our work, is not competitive for non-aqueous solvents and has

a negative coefficient of determination for them. We believe that this is due to the insufficient accounting of non-electrostatic effects in SCIPCM. These results are very encouraging because, to our knowledge, this is the first attempt to universalize iso-density PCMs whereas SMD, and other universal models from the same tradition, have almost two decades of research and optimization behind them [45, 46, 47].

Despite the apparent success of the iso-density approach, there are several important inadequacies which require further work to overcome. The most important, in our opinion, is the fact that the dispersion interaction is treated only at an effective surface tension level. This makes it difficult for the theory to distinguish between similarly sized solutes if the electrostatic interaction is very weak. This is not a problem for polar solutes (such as alcohols or thiols), but may be a problem for some less polar ones. For example, this theory would predict very similar solvation energies for hydrocarbons and their corresponding fluorocarbons, when in fact, the solvation energies might be very different.

Furthermore, there are also inadequacies resulting from the underlying electrostatic model. In this work, we used the nonlinear continuum model of Gunceler et al [50]. This model correctly captures nonlinear dielectric response resulting from the rotational saturation of permanent dipoles in the solvent. However, problems arise if the solvent molecule has no dipole moment, but has a significant nonzero quadrupole moment. One example of this is CS_2 , but an even more extreme example would be ethylene glycol. The problem arises because ethylene glycol is essentially two dipolar units (each resembling a methanol molecule) attached together, each of which units will experience strong orientation-dependent electrostatic interactions with nearby solutes even

Solute	Experiment	Model	Error	Model (corrected)	Error (corrected)
benzene	0.83	-4.41	-5.24	1.41	0.56
chlorobenzene	-0.26	-5.54	-5.28	1.52	1.78
fluorobenzene	0.69	-4.84	-5.53	1.09	0.40
naphthalene	-2.15	-5.91	-3.76	1.80	3.95
toluene	0.74	-4.83	-5.57	1.93	1.19

Table 2.4: Model predictions and experimental values for solvation energy in the pathological case of ethylene glycol. Second set of results ("corrected") are for a simple model to confirm the origin of the pathology. (See text.) All values are in kcal/mol.

though the entire molecule has net zero dipole moment and thus there is little orientation dependence within a simple dipole interaction model. To establish whether this indeed is the issue, we consider the performance of a simple, alternate model where we consider the two molecular fragments with dipole moments as completely independent and uncorrelated. We thus consider a fluid with twice the molecular density of ethylene glycol but with the dipole moment of the molecular fragments, methanol in this case. Such a model clearly ignores the strong correlations between these fragments, nonetheless, as seen in table IV, this procedure improves solvation energies, indicating that the quadrupole moment is indeed the source of the problem. We believe thus that more sophisticated electrostatics models, such as those using a non-local response model [70], will have greater success in such pathological cases where the solute consists of molecules with zero net dipole moment but which yet consist of fragments with significant dipoles.

2.4 Surface solvation energy of Lithium Fluoride

With the model construction complete, we consider a demonstration application to a periodic system. Here, we illustrate the capability to compare the effects of different solvents by calculating the cleavage energy of the lithium fluoride (100) surface. LiF is a rocksalt crystal which plays an important role in the passivation of electrode surfaces in lithium-metal batteries [50], and whose surface energy is one of the several parameters that are often included in models of dendrite growth on such interfaces [71]. The surface cleavage energy, in this context, is the energy cost of creating additional surface from bulk material, defined as the energy difference (per unit surface area) between a surface slab³ of LiF and an equivalent number of formula units in the bulk. A larger (positive) surface energy indicates that a greater amount of energy is needed to create a given surface within a particular solvent.

Our results, calculated both in vacuum and in five different solvents, are given in table 2.5. For the (100) LiF surface in vacuum, we find that the surface energy is 1.90 eV/nm^2 . For the same surface in a solvent, we find that the surface energy is lower, by as much as nearly a factor of five. A lower surface energy (compared to the same surface in vacuum) means that the interaction between the LiF surface and the solvent is attractive and stronger than the bulk surface tension of the solute. We find the one solvent parameter that correlates most strongly with the surface energy to be the critical electron density n_c , which determines the distance of closest approach between the solute and solvent. For solvents such as THF and PC, where this distance is very small (and hence n_c is large), the surface energy is low, whereas for solvents such as glyme, where this

³in the limit that the slab thickness goes to ∞

Solvent	E
Vacuum	1.90
Acetonitrile	1.74
Ethyl ether	1.65
Glyme	1.66
PC	0.83
THF	0.41

Table 2.5: Surface cleavage energy of an LiF (100) surface, in eV/nm². Vacuum denotes the surface energy in the presence of no solvent. PC and THF indicate propylene carbonate and tetrahydrofuran respectively.

distance is large (small n_c), the surface energy is high.

2.5 Conclusion

In conclusion, this work presents progress towards an universal isodensity solvation model for *ab initio* plane-wave calculations in a wide range of polar and nonpolar solvents based only on readily obtainable bulk thermodynamic data and *ab initio* computables, *without the need for a database of solvation energies* to fit the model parameters for each new solvent of interest. This work thus opens to investigation a wide range of solvents previously inaccessible to iso-density solvation studies, opening new application areas, in particular those at solid-liquid interfaces, to plane-wave *ab initio* study.

2.6 Computational details

We performed all plane-wave calculations with JDFTx [30], an open-source implementation of joint density-functional theory. We employed the revTPSS meta-gga approximation [72] for the electronic exchange-correlation and norm-conserving pseudopotentials generated using the Opium pseudopotential generation package[37] to represent the ionic cores. Kohn-Sham orbitals are expanded using planewaves up to a cutoff of 30 Hartrees. We obtained molecular geometries from the CCCBDB database[73]. For solvation energies in SMD [47] and SCIPCM [69] models, we used a 6-31G* basis set.

CHAPTER 3
STABILITY AND SURFACE DIFFUSION AT LITHIUM-ELECTROLYTE
INTERPHASES WITH CONNECTIONS TO SUPPRESSION OF
DENDRITE SUPPRESSION ¹

3.1 Introduction

Development of more efficient energy storage technologies is needed to build a more sustainable future. Understanding physical processes at the atomic scale on electrode-electrolyte interfaces is an important intermediate step towards realizing this goal. Motivated by the desire to help enable many new applications, ranging from grid storage to long-ranged electric cars, researchers have also been using the tools of *ab initio* electronic structure to help develop better rechargeable lithium batteries [75, 76, 77, 78, 79, 80, 81, 82, 83, 84, 85, 86, 87, 88, 89, 90, 91, 92].

The current state-of-the-art in rechargeable batteries is lithium-ion technology, where the presence of a graphitic anode host results in deadweight (carbon) to be carried along with the battery. Metallic anodes would be a better choice due to their increased energy density ($\sim 3860 \text{ mAhg}^{-1}$) [93, 94], but they suffer from localized nucleation while charging and form needle-like structures called *dendrites* [94, 95, 96]. Despite many years of concentrated effort, there are still many unanswered questions about the underlying physical mechanisms of lithium dendrite initiation and growth. This is partly due to the complex nature of the passivation layer, also called the solid-electrolyte in-

¹ This work led to an invention disclosure to CCTEC, which resulted in a successful patent application [74]. Co-author credits: This work was done in collaboration with Yalcin Ozhabes. The preprint is available at arXiv:1504.05799

terphase (SEI), that forms when the metallic electrode comes in contact with the electrolyte [97, 98, 99]. Existing ideas and models on dendritic electrodeposition of lithium suggest that chemical inhomogeneities in the SEI layer result in spatially varying rates of deposition on the surface, which then lead to instabilities because any protrusion tends to concentrate electric field lines [100, 101, 102, 103, 104, 105, 106].

Recent experiments have shown that the composition of the SEI layer has a dramatic effect on the performance of the battery cell. Based on our previous theoretical work [76, 77], Tu et. al. have managed to suppress dendrite growth in liquid and nanoporous electrolytes by passivating the surface of the anode with lithium-halides [107]. Likewise, researchers from Stanford have succeeded in designing an interfacial layer from carbon nanospheres which improves cycling efficiency [93]. Understandably, these results and many others stimulate a strong interest in studying the fundamental physical mechanisms within the SEI layer, and to date, many studies have investigated the bulk properties of these materials (e.g. bulk diffusion of lithium) [84, 85, 86].

The rich physics at the interface between anode and liquid electrolyte is much less understood, though there have been very promising new developments in this field as well [76, 78, 108, 93]. Very recently, Jäckle and Groß have published a comparative study of metallic lithium, sodium and magnesium surfaces [78]. Their DFT calculations suggest that surface diffusion is significantly faster on magnesium metal than on lithium metal, which may be important to understand why lithium forms dendrites while magnesium does not. While this work is very important, we believe (and the authors themselves also point out) that more investigation in this area is needed because that work does not ad-

dress the presence and the effect of the electrolyte and, critically, the fact that metallic electrodes do not present pure surfaces to the electrolyte but rather complex non-metallic passivating layers known as SEI.

In this paper, we focus on the physical processes on the surfaces of various SEI materials for metallic lithium anodes. In particular, we provide an explanation of the physical mechanisms by which halogen additives (especially F^-) to the electrolyte suppress dendrites and improve cycling efficiency [107, 109, 110, 111, 112, 113]. To this end, we utilize density functional theory to calculate surface cleavage energies and surface diffusion barriers for the most commonly reported SEI materials in the literature [114, 115, 116], and then use these results to help understand the experimentally observed trends. Our hope is that such understanding will accelerate the development of novel anode materials to improve battery performance. Our results support the growing belief [76, 77, 101, 107, 78] that anode materials with high surface energy and surface mobility are desirable. We also detail our previous claim [76], recently supported by experiment [107], that Lithium-halide SEI layers have these desirable properties and that they are effective in suppressing dendrite growth on metallic lithium anodes.

3.2 Computational Methods

To perform first principles DFT calculations, we use the open source JDFTx software[30] which is based on the direct minimization of an analytically continued total energy functional [117]. Ultra-soft pseudopotentials [118] from the GBRV library[119] are generated using the Vanderbilt pseudopotential code

[120]. To account for electronic exchange and correlation, we use the PBE flavour of generalized gradient approximation [14]. Throughout this methods section, we work in standard atomic units; i.e. bohr (B) for distances and hartree (H) for energies. All results in the sections below will be presented in more familiar SI units.

For the Brillouin zone sampling of bulk units, we use a k-point grid of $4 \times 4 \times 4$ which we determined by converging the total energy to a level of 0.1 mH. The energy cut-off for the plane wave basis was 20 Hartree which was also consistent with the same convergence threshold. The nuclei were relaxed until the root mean square of the forces were below 0.1 mH/Bohr.

To test our choice pseudopotentials as well as other calculation parameters, we calculated lattice constants of various Lithium SEI materials. The results, plotted in figure 3.1, were satisfactory. (It is our belief that DFT has the largest error in the lattice constant of LiOH because LiOH has a layered structure where long-ranged dispersion interactions play an important role.)

To calculate the surface formation energies, we create slabs varying in size from compound to compound. To determine the thickness of each slab, we take the number of layers that are necessary to converge the surface energy to a level of 0.1 mH per unit cell. The vacuum layer (or solvent for fluid calculations) between the slabs is 20 Bohr, allowing us to collapse the three dimensional k-point grid to a planar grid. The center layer is held fixed and the rest of the slab is relaxed with the same convergence criteria mentioned for the bulk calculations. Where needed, we use a truncated Coulomb kernel [122] along the slab axis to prevent spurious electrostatic interactions between slabs. Then we calculate surface formation energies by taking the difference of the slab energy and the

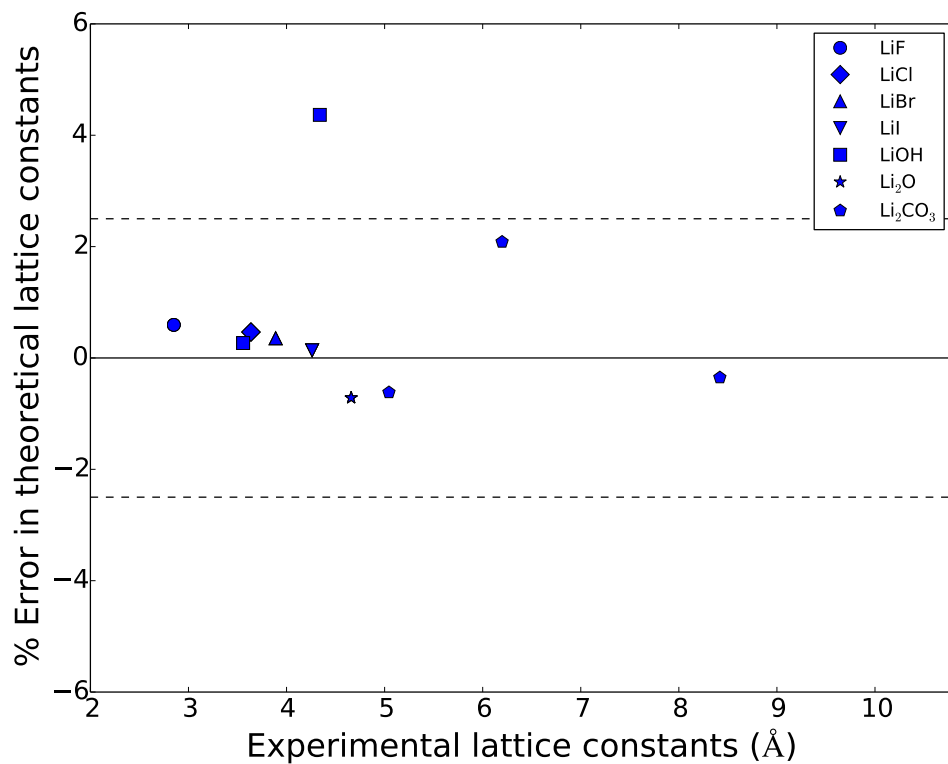


Figure 3.1: The percentage error in DFT lattice constants, plotted as a function of the experimental lattice constants. The solid black line represents exact agreement of theory and experiment. The dashed black lines represent $\pm 2.5\%$ deviations from experiment.

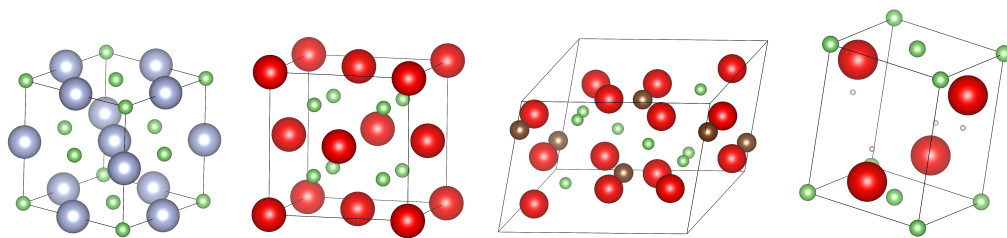


Figure 3.2: From left to right: rocksalt (Li-halides), anti-fluorite (Li₂O), zabuyelite (Li₂CO₃) and LiOH. Pictures were made using VESTA [121].

energy of equal number of formula units in the bulk and then dividing by the surface area.

$$E_{\text{surf}} = \frac{1}{2A}(E_{\text{slab}} - E_{\text{bulk}}) \quad (3.1)$$

For all crystals, we pick the surface with the lowest surface energy. (100 for LiF, 001 for LiOH and Li₂CO₃, 111 for Li₂O)

To study surface diffusion, we consider the hopping process of an adatom that moves from one equilibrium position to the other and whose rate depends on the energy barrier along that path. We determine the diffusion path by comparing the binding energies of the adatom at the high symmetry points along the surface, letting the adatom relax in the direction parallel to the slab normal. Once we determine the endpoints of the diffusion pathway, we carry out a series of intermediate calculations by putting the adatom in a series of sites equally spaced on the line connecting the two binding sites. For these calculations, the entire slab relaxes except the middle layer, while the adatoms are restricted to stay on the plane perpendicular to the diffusion path. To minimize the interactions between periodic images of adatoms, we use 3×3 supercells.

Standard plane-wave electronic structure methods have difficulty handling interfaces between battery electrodes and the electrolyte [123], largely due to the need to thermodynamically sample the configuration space of the liquid electrolyte. As a result, there have been fewer *ab initio* investigations of lithium metal anode-electrolyte interfaces compared to, for example, the investigations of the bulk properties of lithium intercalation compounds [79, 80, 81, 82, 83, 92].

In principle, one can sample the configuration space of the electrolyte using *ab initio* molecular dynamics [108, 91], and further accelerate the calculation using hybrid techniques such as QM/MM [20]. However, calculation of free en-

ergies with these methods are difficult and these approaches often do not easily scale to the large number of materials we want to study. An alternative approach is that of continuum solvation models [25, 77, 124], where the individual molecules in the liquid electrolyte are replaced with a continuum field, and thus free energies can be computed with a single density-functional calculation. Fortunately, recent developments in continuum solvation models [25, 77, 125, 124] have made it feasible to efficiently study the solid-liquid interfaces for a large number of material/electrolyte combinations.

In this work, we use a nonlinear polarizable continuum model which models the electrolyte environment as a continuous field of interacting dipoles [77]. This approach can also capture dielectric saturation effects, which are important near the surfaces of highly polar materials such as the Lithium SEI surfaces we consider here. In this nonlinear continuum model, the density profile of the electrolyte ($s(\vec{r})$) is computed self-consistently from the electron density of the surface slab ($n(\vec{r})$) as

$$s(\vec{r}) = \operatorname{erfc} \frac{\ln(n(\vec{r})/n_c)}{\sigma \sqrt{2}}, \quad (3.2)$$

where σ ($= 0.6$) determines the width of the transition region that is set to be resolvable on the FFT grid and n_c is a (solvent-dependent[124]) critical electron density value that determines the location of the solute-solvent interface. For the non-electrostatic terms in the surface-electrolyte interaction, (such as cavitation entropy and long-ranged van der Waals) we make use of the effective surface tension approximation [25], which modifies the bulk (macroscopic) surface tension of the electrolyte to approximate these contributions.

3.3 Surface energies and diffusion

The formation of dendrites represents an increase in surface area. The thermodynamic perspective would thus indicate that SEI materials with greater surface energies should offer greater dendrite resistance. Furthermore, dendrite nucleation may be driven by cracks in the SEI [94], so that a stable SEI with a high surface formation energy would offer resistance to this mechanism as well.

However, the kinetics during electrodeposition might very well drive the system far from equilibrium. Therefore, one must also consider the mechanism by which surface energy would tend to suppress dendrites, namely surface diffusion. Following the same train of thought, one expects that materials with fast surface diffusion, for example those with small diffusion barriers for adatoms, would be less likely to form dendrites.

This section is broken into four parts: In the first part, we obtain order-of-magnitude estimates for those diffusion barrier heights which would make diffusion an important process during electro-deposition. We find that, indeed, most SEI materials in the following sections do have diffusion barriers in the relevant range. In the second part, we investigate a binding-site switching mechanism that results in unusually low diffusion barriers for some lithium halides. In the third part, we summarize our results for the surface energies and diffusion barrier heights for many candidate lithium SEI materials, and discuss the trends we observe. We investigate multiple classes of materials: rocksalt halides (LiF, LiCl, LiI, LiBr), layered (LiOH) and multivalent (Li_2O , Li_2CO_3). In the final part of this section, we present an intriguing correlation between our diffusion barrier results and the experimentally observed time to short circuit.

3.3.1 Comparing rates of deposition and diffusion

It is important to know whether, at experimental conditions, surface diffusion can be competitive with electrodeposition. We now probe this question with a simple order-of-magnitude analysis. We assume that diffusion is a random walk where the hop rate is given by the Arrhenius equation $R = R_0 e^{-\frac{\Delta E}{kT}}$, where kT is thermal energy, ΔE is the diffusion barrier and R_0 is a base attempt rate related to the material's phonon frequencies. To determine the balance between surface diffusion and deposition, let q_e be the charge of the arriving ions, J be the current density and a be the dimension of the surface unit cell. Under these conditions, we expect that dendrites form when the local current density becomes high enough to overcome surface diffusion, specifically when the mean distance traveled by a diffusing atom ($d(t) = \sqrt{Rta}$) in the (mean) time interval between two deposition events at the same site ($t = q_e / (Ja^2)$) is smaller than the growing dendrite tip. In this simple scenario, the critical barrier at which the rate of electrodeposition equals the rate of diffusion, is given by $\Delta E_c = 2kT \ln \left[\frac{1}{L} \sqrt{\frac{R_0 q_e}{J}} \right]$, where L is the size of the dendritic protrusion.

Experiments typically use current densities on the order of 1.0 mA/cm², but owing to the highly non-uniform rate of deposition on the surface, especially near any protrusion, the relevant current densities can be orders of magnitude higher. Indeed, measurements of lithium dendrite growth [126, 127] have yielded the current densities at the dendrite tip in the 100–1000 mA/cm² range. As for R_0 , following previous studies[78], we assume a standard phonon frequency of ~ 10 THz. For any microscopic protrusions in the order of 1-100 micrometers, we see that the critical diffusion barriers that result in competitive rates are of a few tenths of an electron volt. At 100 mA/cm² current density the

critical barrier for a protrusion of size 5 micrometers is approximately 0.1 eV, which would mean that for such a system diffusion on a surface with a barrier above this value would be too slow to mitigate the growth of dendrites regardless of thermodynamic unfavourability. In fact, we do find that surface diffusion barriers on typical SEI materials are in this range and so a detailed study of surface diffusion is necessary for understanding dendritic processes. Finally we note that, one must take this very simple analysis with care, as quantitative predictions other than order-of-magnitude estimates are likely to be beyond its capabilities.

3.3.2 Change in the binding sites of Li-halides

Below we find that of all the SEI materials we have studied, the lithium-halides are the most promising from the above point of view, with diffusion barriers ranging from 0.03 to 0.15 eV. The physical reason for these low barriers are as follows. Even though the bulk structure of all the lithium-halide materials we consider here is the same (rocksalt), the binding site for adatoms changes as the anion size increases. For halides with small anions (F and Cl) the binding site for the adatom is directly above the anion (“anion site”), and in the transition state for diffusion, the adatom sits between two anions and two cations (“in-between site”). See figure 3.3 (a) for an illustration. On the contrary, for large anions, the roles of these two sites are reversed and the binding site sits at the “in-between site” (slightly off-center) while the transition state has the adatom at the “anion site”. (See figure 3.3 (b)) Now, the diffusion barrier is equal to the energy difference between the binding site and the transition-site. Because of this, halide surfaces that are in the neighbourhood of this change (LiCl and LiBr), where the

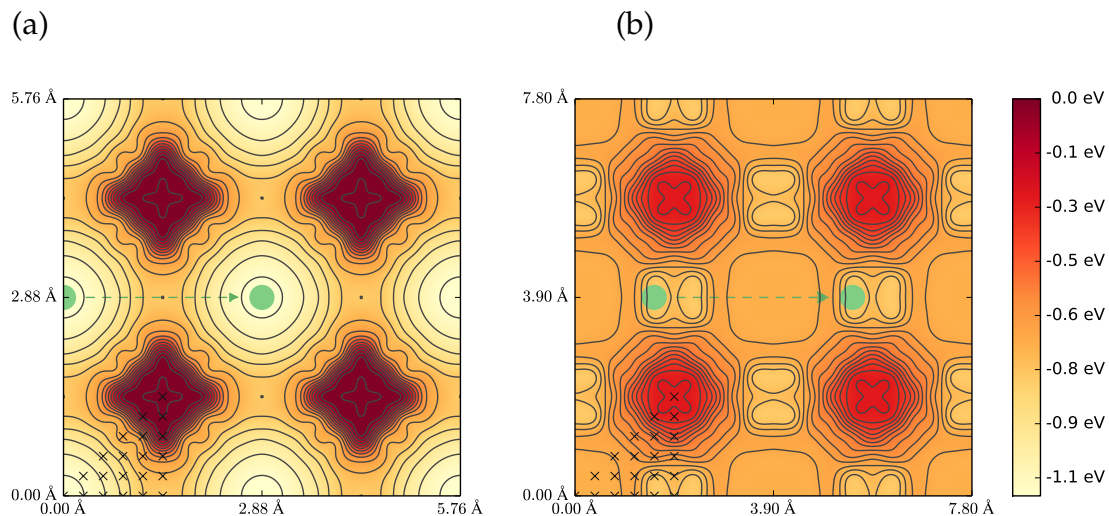


Figure 3.3: Surface binding energies versus its binding site. LiF is in the left, LiBr is on the right. The lowest energy binding sites are indicated with a green circle and the diffusion path is as shown with the green arrows. The black cross markers indicate our data points, the whole contour plot is generated using symmetries of the surface and cubic interpolation.

sign of this difference changes, have very low diffusion barriers. On the other hand, LiF, which is far from this change, have a relatively larger barrier, but still small compared to non-halide SEI materials.

The reason for the change in the binding site with anion size is steric interactions. For the two smaller halogens, the in-between site is too close to the two cations, which makes it energetically less favorable. However, as the anions get bigger, the distance from the in-between site to the cations increases and the adatom prefers to place itself in this halfway point where it can also interact with two anions simultaneously. Finally we note that even though the binding site changes as one goes from LiCl to LiBr, the diffusion path remains the same.

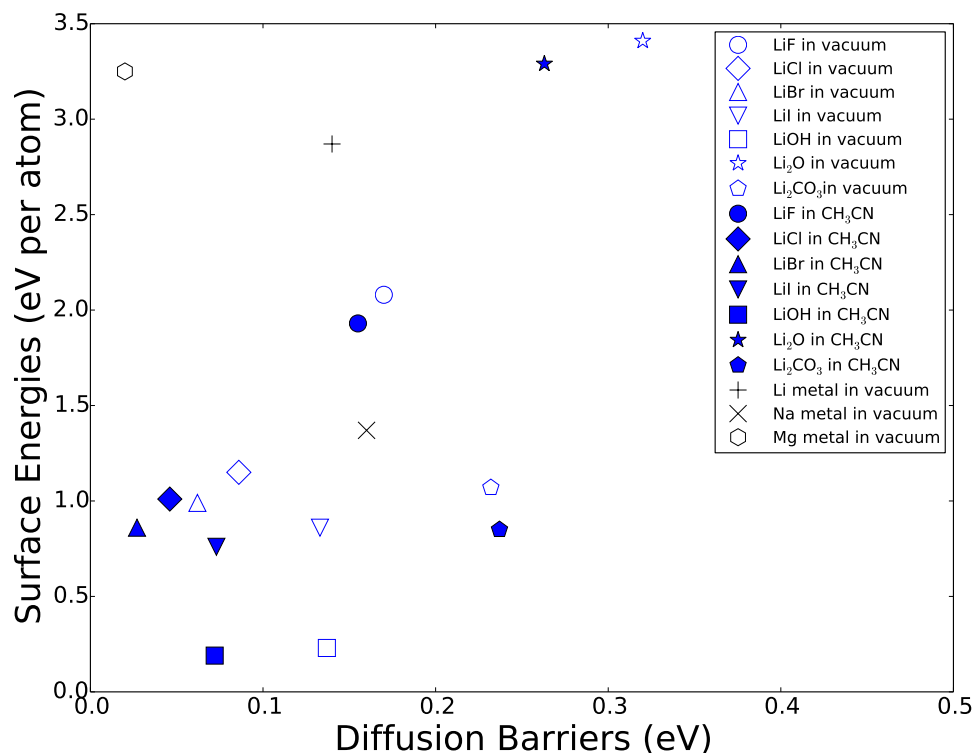


Figure 3.4: The surface diffusion barrier (x-axis) and the surface energy (y-axis) of various Lithium SEI materials. Hollow data points represent surfaces in contact with vacuum whereas filled data points represent the same surfaces in contact with the electrolyte (CH_3CN , modeled with a polarizable continuum model). The black markers indicate the bare metal calculations by Jäckle and Groß [78].

3.3.3 Predictions for battery performance

Figure 3.4 summarizes all of our results, not only for the diffusion barriers for all of our surfaces (including halides, as well as the hydroxide, carbonate and oxide) but also for the corresponding surface energies. The data show that the presence of the electrolyte has significant impact, especially on the surface diffusion barriers. The surface energies of all ionic crystals go down (often by

5 – 15%), owing to the strong electrostatic interaction between the surface and the solvent. The surface diffusion barriers, however, change more dramatically, by up to as much as a factor of 2. The diffusion barrier for all materials but one (Li_2CO_3) decrease when the electrolyte is included in the calculation. These changes in diffusion barriers are significant because the rate depends exponentially on the barrier height and because these energy changes are on the order of several kT (which, at room temperature is approximately 0.025 eV).

The data also suggest a strong positive correlation between surface energies and surface diffusion barriers for most, but not all, SEI materials. The most severe trend breakers are magnesium metal (black hexagon), lithium metal (black plus) and LiOH (blue square). Of these, the metals break the trend likely due to their very different electronic structure, where Li is not in an oxidized (positively charged) state. LiOH likely breaks the trend because its layered structure and large intra-layer distance cause it to have a very low surface energy along the z-axis.

Li_2CO_3 , present in the SEI layer formed in the presence of many commonly used electrolytes (propylene carbonate, ethylene carbonate and others), is a less severe trend breaker. It has low surface energy and high diffusion barrier, both of which are undesirable quantities in a SEI material. Lithium halides, on the other hand, have lower surface diffusion barriers than Li_2CO_3 while also having either equal or higher surface energies. Our hypothesis, first put forth in an earlier work [76], is that the low barriers may help explain the experimentally observed phenomenon [107] in which the formation of an lithium-halide SEI is effective in suppressing dendrites. We further hypothesize that these mechanisms may be relevant not only in experiments where the electrolyte has

been seeded with a Li-halide crystal [107], but also in experiments where other additives containing fluorine (e.g. hydrofluoric acid or fluoroethylene carbonate) [112, 113, 111] have been used to improve stability and suppress dendritic growth.

As for LiOH and Li₂O, which are also occasionally observed in experiments, [107] LiOH appears to be undesirable because of its low surface energy, whereas Li₂O appears to be undesirable because of its high diffusion barrier. However, the superiority of Li-halides over LiOH/Li₂O is not as conclusive because the halides are superior in only one of the two indicators.

Finally, among halides, figure 3.4 shows that the stability (i.e. surface energy) decreases as one goes down the column of the periodic table, from F to Cl to Br to I. This is likely due to some combination of the decrease in the electronegativity of the ions (which weakens the strength of the ionic bonds) and the steric interactions increasing the size of the lattice (which decreases the electrostatic stability of the lattice). Decreased stability is an undesirable property in battery materials as it tends to lower the voltage at which the surface breaks down.

3.3.4 Comparisons with measurements of short-circuit time

From a practical perspective, the ultimate figure of merit is the length of time before the battery short circuits. Figure 3.5 plots this quantity, as measured by Lu, Tu, and Archer [107] in a symmetric cell, as a function of our calculated diffusion barriers. Because diffusion is an activated process, we choose a logarithmic scale for the vertical axis. Moreover, for Li₂CO₃, Li₂O and LiOH there are no separate data, instead, for this single measurement that we have, where there are no halide additives, the surface of the anode contains spatially-varying frac-

tions of all three of these species. The observed breakdown is likely due to the most-dendrite prone among these three materials, and thus represents a lower bound for the lifetime of each of the materials. Due to the notably lower barrier which we calculate for the hydroxide, we strongly suspect that the observed cycle lifetime is associated either with the carbonate or the oxide. Finally, because the barriers we calculate for these latter two materials are so close, we can not determine unambiguously which of these two materials fails first. Accordingly, the figure includes the experimental lifetime twice, once for each one of these two materials.

The data in figure 3.5 show a clear linear trend consistent with an Arrhenius-like behaviour. However, the slope does not appear to be exactly unity, demonstrating the importance of other factors beyond the diffusion barrier. Additionally, one point, lithium fluoride, appears to be an outlier, requiring additional explanation. LiF has the highest barrier among the halides but the second longest time to short circuit. We suspect that this deviation from the trend may be tied to it having the most stable surface among the halides (see figure 3.4), thus affording it additional stability. Lithium fluoride's high surface energy derives not only from the high electronegativity of the fluoride atom, but also from its very small lattice constant and surface area per formula unit. (LiCl, the second smallest halide, has a surface area $\sim 60\%$ larger than LiF.)

While it is not surprising that a single quantity (the diffusion barrier) is not enough to fully explain the experimental lifetimes, we find it encouraging that there is such strong correlation between diffusion barriers and the experimental lifetimes.

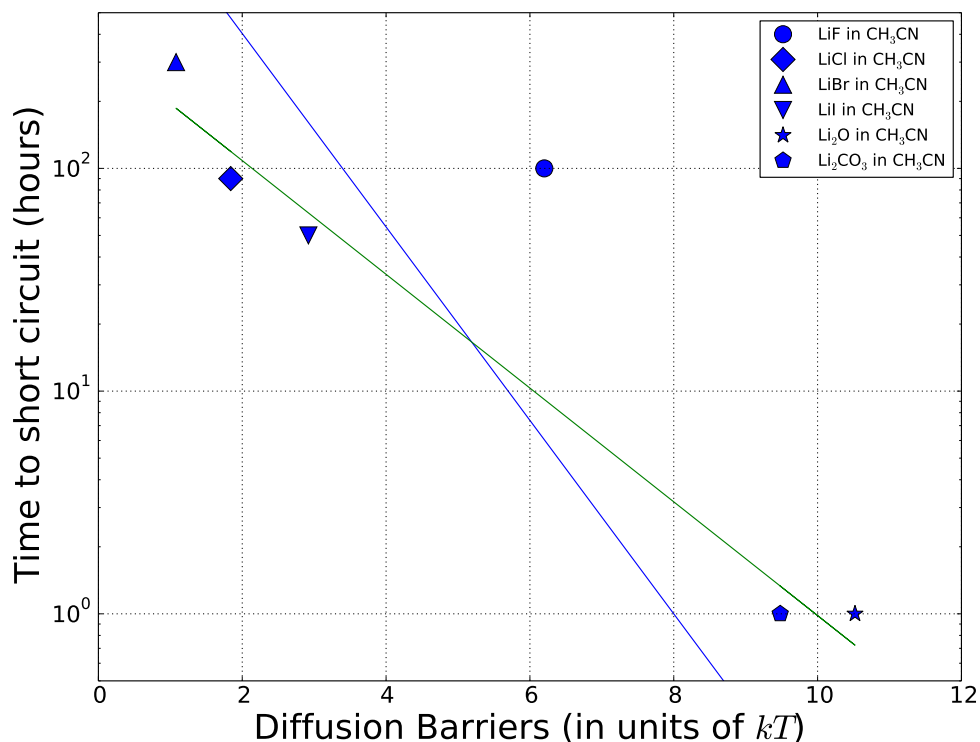


Figure 3.5: Battery short circuit times (from Lu, Tu, and Archer [107]) plotted as a function of the surface diffusion barrier. The green line is the best fit line, excluding the one outlier. The blue line shows has the slope for an Arrhenius process.

3.4 Conclusion

Recent experiments, prompted by earlier theoretical work[76], confirm the success of Lithium-halide additives in suppressing dendrite growth[107, 109, 110], consistent with the findings of previous experiments with other fluoride-containing electrolyte additives [112, 113, 111]. Prompted by this, we set out to explore more deeply the mechanisms of dendrite suppression at the atomic level.

We performed density-functional calculations to determine the surface energies and the surface diffusion barriers of lithium solid-electrolyte interphase materials. Our calculations show that a lithium-halide SEI layer results in increased stability of the surface (higher surface energy) and faster diffusion along the surface (lower surface diffusion barrier for adatoms), both of which are likely important in explaining the above phenomenon. Furthermore, our results provide an explanation for the unusually low diffusion barriers on halide surfaces, tracing this effect back to a change in the binding site. This change in binding site, in turn, is driven by the trends in the electronegativity and the sizes of the anions in the halide crystals. Finally, we observe a clear, approximately Arrhenius correlation between battery time to short circuit and surface diffusion barriers, that can be used as a guide to suggest new material systems to further enhance stability against dendrite formation.

This work, which focused on solid-electrolyte interphase materials, leaves many directions yet to be explored. In mitigating dendrite growth, multiple diffusion pathways are available, including surface diffusion, bulk diffusion, and diffusion at the SEI-metal interface. A study similar to this one, but for the SEI-metal interface, would be illuminating. Finally, with the potential importance of surface diffusion established, results from *ab initio* studies should be incorporated into macroscopic models of dendrite growth.

CHAPTER 4

JOINT DENSITY FUNCTIONAL THEORY OF ROOM TEMPERATURE IONIC LIQUIDS: ION PAIRING AND DIFFERENTIAL CAPACITANCE

Room temperature ionic liquids (RTILs) [128, 129, 130] are salts which remain liquid even at room temperature. Typically consisting of large molecular cations and anions, RTILs have many interesting physical properties, including very high viscosity and almost negligible vapor pressure. From a practical perspective, there is much recent interest in ionic liquids because of their suitability as electrolytes for a wide range of electrochemical applications as a safer and less toxic alternative to organic solvents, particularly for use in super-capacitor applications, where the lack of Faradaic reactions allow for very high rates of charging/discharging and for more charge/discharge cycles compared to batteries [130, 131, 132].

Physically, the very large sizes of the ions create a system where Coulombic screening and steric length-scales are comparable, and may be tuned, leading to startlingly capacitive behaviour, including so-called "double-hump" differential capacitance [133, 134]. Furthermore, as self-dissociating solvents, RTILs provide a unique laboratory to study ion pairing in liquids, as we explore here.

The nature of ion pairing in these systems is still a matter of debate and has been the subject of many recent experimental and theoretical studies [135, 136, 137, 138, 139, 140, 141, 142]. The consensus opinion on the microscopic structure of room temperature ionic liquids is that they consist (mostly) of dissociated pairs of ions and that these ions are free to move independently from one another (Figure 4.1, left panel). This consensus view is supported by NMR spin echo and electrochemical impedance measurements of the molar conductivity

ratio [135], one measure of cation-anion aggregation. Based on such analysis, the consensus belief had been that about 1/2 to 2/3 of the ions (depending on the ionic liquid) are free to move independently and contribute to electrical conductivity at room temperature. However new surface-force measurements have challenged this consensus view and suggest that ionic liquids behave as *dilute* electrolytes, with less than 1% of ions actually free to screen external electric fields [137, 139]. This seemingly irreconcilable view on the microscopic structure of ionic liquids has sparked a controversy in the literature [138, 140, 143].

Not only the extent, but also the nature of the ion aggregation has been the subject of intense debate and experimental study. While aggregation may be in the form of simple anion-cation pairs, it may also be caused by the "presence of a coordinated network of ions" [138]. In this matter, we believe that the Fourier transform infrared spectroscopy (FTIR) experiments by Koddermann et. al. are very important [136]. Their results for [MEIM][Tf₂N] ionic liquid separate cations in the RTIL into two groups based on vibrational signature, consistent with the view that the cations exist either as free ions or bonded to a single anion.

Previous theoretical studies of room temperature ionic liquids have employed a wide range of theoretical tools, including mean field theory [133], Monte Carlo simulation [140, 144], *ab initio* quantum chemistry [141, 142, 145, 146, 147, 148, 149], classical molecular dynamics [150, 151, 152, 153] and classical density-functional theory [154, 155]. While it is possible to study the electronic structure of RTILs and solutes/surfaces in contact with RTILs using vacuum/gas-phase calculations or *ab initio* molecular dynamics simulations, continuum solvation theories offer a much more physical and computationally

expedient path because they remove the need for costly thermodynamic integration and provide direct information on screening effects. As such, there has been recent interest in the development of quantum mechanical continuum solvation models and their use to study RTILs, employing for example the COSMO [146] or SMD [156] solvation models. However, quantum mechanical solvation models of RTILs developed to date are not suited for plane-wave basis sets and only model solute-RTIL interactions as the one between a solute and a dielectric or metal interface, ignoring the ionic screening due to the free ions.

In this work, we develop a fully self-consistent quantum-mechanical solvation theory of room temperature ionic liquids based on joint density-functional theory that can be used to study ionic liquids and species or surfaces solvated in ionic liquids. Unlike existing models that are developed in the context of gaussian basis sets, our model is developed for use in a plane wave basis, and thus can also be used to study solid/RTIL interfaces. For molecules solvated in ionic liquids, this theory is competitive with others in the literature [146, 156].

We then employ this theory to study ion pairing for several different ionic liquids and calculate their fractional dissociation from theory to aid in the resolution of weak vs strong electrolyte debate. The results we obtain support the consensus view [135, 140] that ionic liquids are strong electrolytes (fractional dissociation order of unity) and provide evidence against the interpretation of recent experiments [137, 139] which suggest low fractional dissociation (less than 0.1%).

We next employ our theory to investigate the idea of assigning non-integer (less than unity) effective charges to dissociated ions, which has become popular recently in the literature as a way of increasing the agreement between molecu-

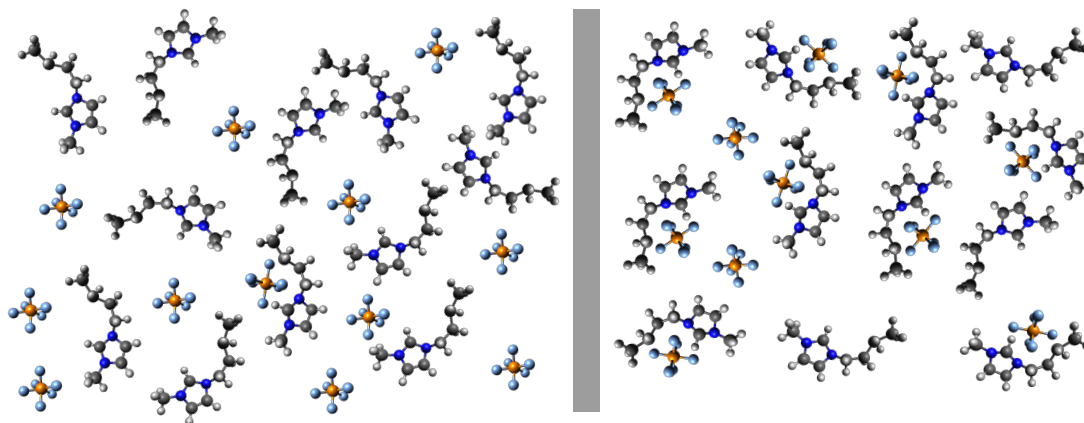


Figure 4.1: Two of the competing microscopic pictures for an RTIL. On the left hand side, most ions forming the RTIL have been dissociated and are free to move independently, with only a small fraction existing in pairs. On the right hand side, most ions have formed into pairs, with a very small fraction existing in dissociated form. Note that fractions and interatomic distances have been greatly exaggerated.

lar dynamics simulations and experimental measurements [150, 151, 152, 157]. In this case, we find the idea of a partial charge transfer between anion and cation to be inconsistent with the free energies calculated using JDFT, lending support to the alternative hypothesis [151] that screening originating from the ionic polarizabilities and not partial charge transfer, is the reason why effective non-integer charges improve accuracy.

Finally, we study a noble metal surface (Au 111) immersed in an ionic liquid, and probe its electrochemical behavior under applied potential. When in contact with [BMIM][PF₆], we find excellent agreement between JDFT and the experiment for the charging curve and the differential capacitance of the surface [158], with JDFT outperforming even the highly optimized and state-of-the-art

classical molecular dynamics simulations of the same system [153].

4.1 Solvated electronic structure

Gas-phase binding (pairing) energies of RTIL ions have been studied in the literature with a wide range of *ab initio* and quantum chemical methods, including density functional, Hartree-Fock and post-Hartree-Fock techniques [141, 142, 147, 148, 149]. The results of these studies establish the success and accuracy of dispersion-corrected density-functional theory in ionic liquid systems through direct comparison to more accurate post-Hartree-Fock methods, thereby validating our use of dispersion-corrected density-functional theory for the present study.

Above studies, moreover, find that pair binding energies in vacuum are in the range of 300-400 kJ/mol (about 3-4 eV), which would indicate essentially zero fractional dissociation in the liquid, which we know from experiment not to be the case. Self-consistent inclusion of screening effects in the liquid is therefore essential to understanding RTILs.

Joint density-functional theory (JDFT) in fact provides a very economical yet accurate method for including such effects. JDFT is an in-principle exact variational principle that expresses the free energy of a solute-solvent system in terms of the mean (thermodynamically averaged) spatial densities of the solvent constituents and the solute electron density. In this work, we follow the linear polarizable continuum approximation to JDFT, the foundations of which we discussed previously [77]. Within this approximation, the response of the fluid around an ion or an ion pair is broken down into three separate contribu-

tions: (1) the dielectric response, accounting for the reorientation of the permanent dipoles (formed from neutral ion pairs) as well as the polarizability of the individual ions in the RTIL; (2) the ionic screening due to the motion of charge monopoles (ions) in the solution; (3) Further non-electrostatic terms including the formation free energy of the cavity and also long-ranged dispersion.

In the approximation we use here, the solvent density profile $s(\vec{r})$ is determined self-consistently [24, 77] from the solute electron density as

$$s(\vec{r}) = \operatorname{erfc} \frac{\ln(n(\vec{r})/n_c)}{\sigma \sqrt{2}}, \quad (4.1)$$

where $s = 1$ indicates the presence of fluid, $s = 0$ indicates the interior of the solute cavity, n_c is the critical electron density contour determining the solute-solvent interface and σ is the width of the transition, usually set to make the transition resolvable on the numerical grid employed in the calculations. (following previous examples [77], we use $\sigma = 0.6$). The local dielectric constant of the solvent is then simply

$$\varepsilon(\vec{r}) = 1 + (\varepsilon_b - 1)s(\vec{r}), \quad (4.2)$$

where ε_b is the dielectric constant of the bulk fluid. This approximation is very similar to the one made in the SCCS solvation model [25], and has been successfully applied to a wide range of molecular solvents (such as H₂O, CCl₄ and CHCl₃).

Once the dielectric response of the fluid is determined, the total electrostatic free energy density of the system (contributions (1) and (2) above) can be written as

$$A_{es} = \int d^3r \left[\phi(\vec{r}) [n(\vec{r}) + n_{nuc}(\vec{r})] - \frac{\varepsilon(\vec{r})}{8\pi} |\nabla\phi(\vec{r})|^2 + A_\kappa(\vec{r}) \right] \quad (4.3)$$

where $n_{nuc}(\vec{r})$ and $n(\vec{r})$ are, respectively, the total nuclear charge density and the total electronic charge density of the solute, $\phi(\vec{r})$ is the mean electrostatic potential and $A_\kappa(\vec{r})$ is the free energy contribution from the screening by the free ions in solution, which is one of the new contributions in this work.

The first of three approximations which we consider for the ionic screening term $A_\kappa(\vec{r})$ is the linearized Poisson-Boltzmann approach. In this approach [49] $A_\kappa(\vec{r})$ is

$$A_\kappa(\vec{r}) = \frac{\varepsilon(\vec{r})\kappa^2}{8\pi} \phi^2(\vec{r}) \quad (4.4)$$

where $l_D = \kappa^{-1}$ is the Debye screening length, given in the linear or point-particle limit (abbreviated ln) by

$$l_D = \sqrt{\frac{\varepsilon_b k_b T}{2ce^2}}. \quad (4.5)$$

Here, c is the concentration of free (mobile) anions or cations in the solution, $k_b T$ is the thermal energy and e is the electron charge. Here we implicitly assumed that all ions have charge $\pm 1 e$, though generalization to other charges is straightforward. The above Debye screening approximation, while powerful and extremely useful for traditional electrolytes, does not build anion or cation size information into the theory, which for RTILs is especially important due to the large sizes of the ions. Accordingly, we propose two alternative approaches to account for such steric effects. In the first approach, we maintain the form of equation 4.4, but modify the Debye screening length to include the sizes of the ions. This approach, we abbreviate as ln-md (linear - modified Debye). In the second approach, we modify the form of the free energy functional to produce a fully-nonlinear Poisson-Boltzmann theory.

Bo Li et. al. have analyzed the free energy-functional for dissolved ions based on the variational mean-field approach [159]. Upon linearization, they

find a modified debye screening length (l_{mD})

$$l_{mD} = \sqrt{\frac{\epsilon_b kT}{e^2}} \left[\sum_j (q_j/e)^2 c_j - \frac{(\sum_j (q_j/e) V_j c_j)^2}{\sum_j V_j^2 c_j} \right]^{-1/2}, \quad (4.6)$$

where c_j is the concentration, and $V_j = \frac{4}{3}\pi R^3$ is the volume associated with each species. It is important to note that the sum includes not only ions, but also solvent molecules as well (for which, $q_j = 0$). For us there is only one anion and one cation species of the same concentration c which yields

$$l_{mD} = \sqrt{\frac{\epsilon_b kT}{2ce^2}} \left[1 - \frac{(\sum_j (q_j/e) V_j (c_j/c))^2}{2 \sum_j V_j^2 (c_j/c)} \right]^{-1/2} \quad (4.7)$$

$$\equiv l_D (1 - \gamma)^{-1/2} \quad (4.8)$$

where the modified Debye screening length is related to the original via a structural factor γ . Both in the limit of point ions (but finite sized solvent) and in the limit of equally sized ions ($V_{anion} = V_{cation}$), we have $\gamma \rightarrow 1$ and the modified Debye length l_{mD} reduces to the standard result. Whereas Bo Li et. al. have developed this approximation in the context of ions (such as NaCl) dissolved in solvent, in our case the distinction between ions and solvent is not very clear. Here, interpret the aggregated (paired) ions as comprising the solvent background.

As we will see later, the above modifications to linear Debye theory proves to be insufficient, necessitating a move beyond the linearized Poisson-Boltzmann approach. Thus in the third and the final approximation we use, we go beyond linearized Poisson-Boltzmann theory in favor of a fully nonlinear Poisson-Boltzmann approach that has been modified to include steric interactions. Specifically we take

$$A_\kappa(\vec{r})[\{\eta_j\}] = kT s(\vec{r}) \sum_j c_j \left[\eta_j(\vec{r}) (\ln \eta_j(\vec{r}) - 1) - \frac{(\rho(\vec{r}) - \rho_0)^2}{\rho_0(1 - \rho_0)(1 - \rho(\vec{r}))^2} \right] \quad (4.9)$$

where $\eta_j(\vec{r})$ is the enhancement factor of the local ion concentration ($\eta_j = 1$ corresponds to the average concentration c_j), $\rho(\vec{r}) = c_j \eta_j(\vec{r}) V_j$ is the local packing fraction, and $\rho_0 = c_j V_j$ is the average packing fraction throughout the fluid. (We here use a slightly different notation for the packing fraction than in our previous publications [77], because we here reserve the variable x for the dissociation fraction). Here, the first term in equation 4.9 generates precisely the full nonlinear Poisson-Boltzmann theory for point ions. The second term is a mean-field steric repulsion term that enforces the packing limit of ions, following the form of similar terms in fundamental measure theory (FMT) of hard sphere fluids [160]. Similar free energy expressions have been used by Bo Li [161] and Vlachy [162] in the context of classical simulations.

Finally, we have used precisely the form 4.9 in the context of typical ions in standard aqueous electrolyte solutions [77]. In that particular case, neither the nonlinearity nor the steric repulsion were found to make a significant impact. However, in ionic liquids, the radii of ions are significantly larger, thus we anticipate that the disagreement between the nonlinear theory and its linear counterpart will also be larger.

The last part of the fluid free energy functional to specify represents the non-electrostatic components of the free energy, which include the dispersion energy (van der Waals interaction) and the free-energy cost of forming the solute cavity. These we approximate using an effective (solvent-dependent) surface tension τ multiplied with the total area of the solute solvent interface, or simply

$$A_{nes} = \tau \int d^3r |\vec{\nabla} s|. \quad (4.10)$$

4.2 Self-consistent determination of model parameters

Simplicity of theory and ease of parametrization are especially important for models of ionic liquids because different choices for the anion and the cation make possible a very large number of different ionic liquids whose fundamental physical properties remain to be understood. It is therefore important for any quantum-mechanical solvation model to be as flexible as possible, allowing easy reparametrization for a large number (potentially hundreds) of different RTILs. The solvation theory outlined in the previous section with only three parameters achieves this. These three parameters are specifically (1) n_c is the critical electron density that controls the location of the solute-solvent interface; (2) τ is the energy cost (or gain) of making the solute cavity; (3) $c = xc_0$ is the concentration of dissociated ion pairs (c_0 is the bulk concentration of all ions).

Note that this last parameter reflects the self-consistency issue discussed in the previous section. Namely fraction x of free (mobile) ions determines the screening length and thus the bulk concentration of charged species and is therefore a parameter that goes into the solvation model, as well as a result that we want to extract. To determine the value of this parameter, we require that the fraction of free (mobile) ions associated with the screening in the theory must equal the fraction which the theory predicts; specifically, so that the free energy cost of breaking an ion pair in solution leads to the same ion concentration x assumed in the screening length.

To determine concentration x from the ion pairing strength ΔE , we employ a statistical model where ions exist either as pairs with binding energy ΔE or in

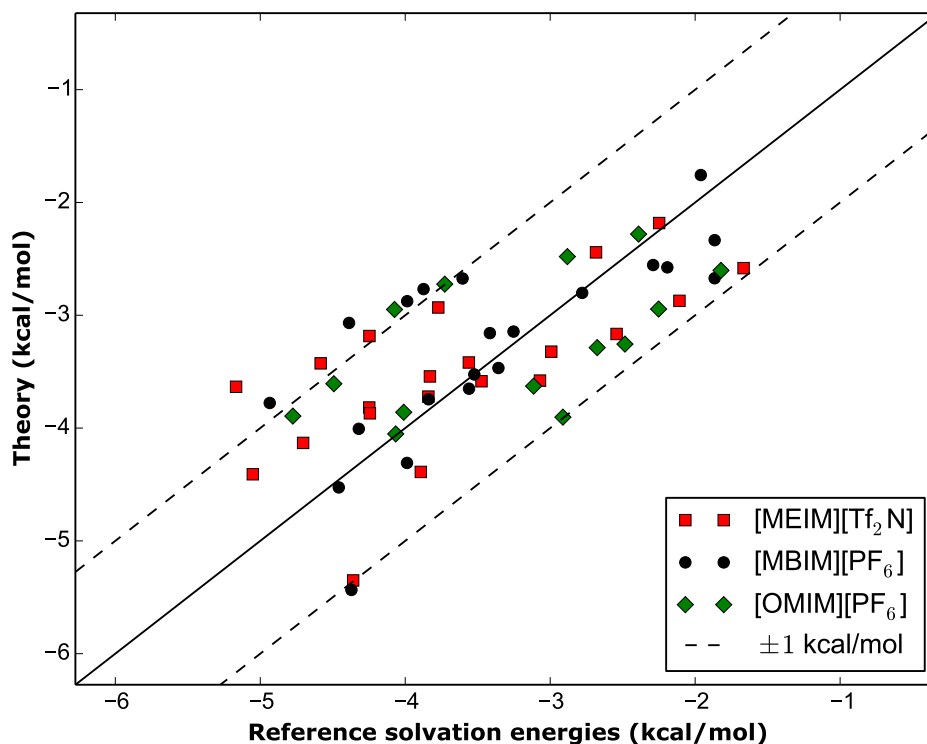


Figure 4.2: The solvation energies of neutral molecules, in three different room-temperature ionic liquids. Diagonal black solid line is the line of exact agreement; diagonal dashed lines show ± 1 kcal/mol errors. Errors for each solvent are reported in table 4.1.

dissociated form. The free energy of the system is then

$$\begin{aligned}
 F(x) &= E(x) - TS(x) \\
 &= Nx\Delta E - kT \ln \Omega(x) \\
 &= N[x\Delta E + 2kT(x \ln x + (1-x) \ln(1-x))]
 \end{aligned}$$

where N is the total number of cations (or equivalently anions) existing either in paired or dissociated state, x is the fractions of cations (or anions) in the dissociated state and k_b is the Boltzmann constant. (The factor of two arises from

	ME (kcal/mol)	MAE (kcal/mol)	SMD-GIL MAE (kcal/mol) [156]
[MEIM][Tf ₂ N]	-0.13	0.58	0.30
[MBIM][PF ₆]	-0.14	0.49	0.61
[OMIM][PF ₆]	-0.02	0.64	-

Table 4.1: The mean (ME) and mean absolute (MAE) errors for 57 molecules in 3 ionic liquids: [MEIM][Tf₂N] (1-methyl-3-ethylimidazolium bis(trifluoromethylsulfonyl) amide), [MBIM][PF₆] (1-Butyl-3-methylimidazolium hexafluorophosphate) and [OMIM][PF₆] (1-Methyl-3-octylimidazolium hexafluorophosphate). Results for individual molecules are plotted in Figure 4.2. In the last column, mean absolute errors of the SMD-GIL solvation model [156] for the same ionic liquids is presented for comparison. A dash (-) means that the data is not available at the given reference.

the fact that both cations and anions contribute to the entropy of the dissociated state.) Minimization of the free energy then gives the dissociation fraction as

$$x = \frac{1}{1 + e^{\Delta E(x)/2kT}}. \quad (4.11)$$

where we include the fact that the pairwise dissociation energy ΔE will be dependent on the fractional dissociation x due to Debye-Huckel screening effects which our ab-initio results show to be significant.

Our objective is to find the self-consistent solution (fixed point) of equation 4.11. Unfortunately, x is not the only parameter that must be determined. The value x we calculate using the solvation theory depends not only on the x assumed, but also on the two other solvation parameters n_c and τ , as well. We therefore determine n_c and τ using the solvation free energies of *neutral* solutes in RTILs, whose solvation energies are insensitive to the ion concentration x . (Such solvation energies can be readily obtained [163, 164, 165] from the experimental partition coefficients found in the literature, which are often measured using gas-liquid chromatography [166, 167].) We therefore begin with an ini-

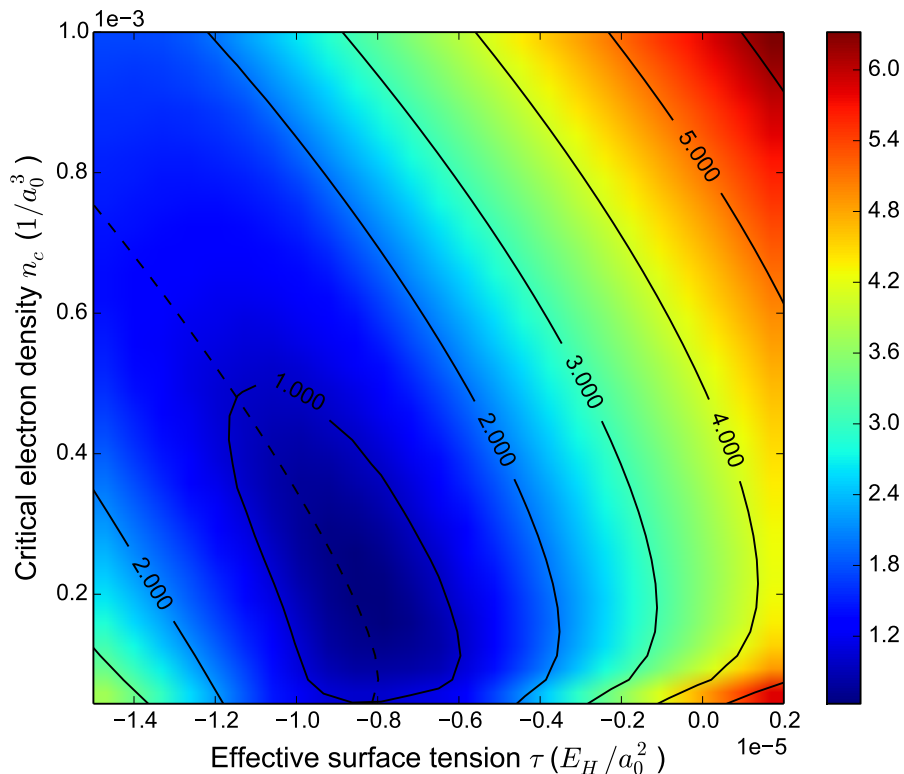


Figure 4.3: 2D scan of the mean absolute error in the solvation energies of neutral molecules in [MEIM][Tf₂N]. The solid black lines are contours of the mean absolute error. The dashed black line is the zero contour for the mean error.

tial estimate for the dissociation fraction x and for that given x , we parametrize the model using the solvation energies of neutral molecules to obtain n_c and τ . (We do this in the same way as in previous works [77], where we select n_c and τ to minimize mean absolute errors for solvation energies). With the resulting parameters, we then calculate the ion dissociation energy ΔE and use this in equation 4.11 to determine an improved value for the dissociation fraction x . We find the iteration to be stable and repeat until the change in x is below 0.1%.¹ For reasonable starting concentrations (from $c = 1$ to $c = 1 \times 10^{-3}$ M), the

¹ As we see later, $\Delta E(x)$ depends monotonically on x , so an alternative approach to the one

	n_c ($1/a_0^3$)	τ (E_h/a_0^2)	x_{ln}	x_{nl}	$\Lambda_{imp}/\Lambda_{NMR}$ [135]	x [137, 139]
[MEIM][Tf ₂ N]	1.386×10^{-4}	-4.773×10^{-6}	0.139	0.101	0.75	8.3×10^{-5}
[MBIM][PF ₆]	1.879×10^{-4}	-3.877×10^{-6}	0.255	0.148	0.68	-
[OMIM][PF ₆]	2.591×10^{-4}	-5.745×10^{-6}	0.282	0.160	-	-

Table 4.2: Self-consistent values for the critical electron density contour (n_c), the effective interfacial tension (τ) and the fractional dissociation (x) for 3 ionic liquids. n_c and τ values are given in atomic units, x is dimensionless. The last two columns show the results two disagreeing experimental measurements ($\Lambda_{imp}/\Lambda_{NMR}$ is the molar conductivity ratio). A dash (-) means that the data is not available at the given reference.

iteration converges in less than 10 cycles (usually five to six). Table 4.2 reports the self-consistent values obtained for 3 different room temperature ionic liquids: [MEIM][Tf₂N] (1-methyl-3-ethylimidazolium bis(trifluoromethylsulfonyl) amide), [MBIM][PF₆] (1-Butyl-3-methylimidazolium hexafluorophosphate) and [OMIM][PF₆] (1-Methyl-3-octylimidazolium hexafluorophosphate). To simplify the self-consistency procedure for nonlinear ionic screening, we make use of the fact that the free energy of neutral solutes are insensitive to the level of theory used for ions, and use the same self-consistent n_c and τ values as we find from the linearized version of the theory.

Figure 4.2 shows the quality of fit for our theoretical solvation energies of neutral solutes in three different RTILs, and table 4.1 reports the overall errors. These have been calculated at the self-consistent value for x for each solvent.

Our fits for the solvation energies of most molecules are within the typical ± 1 kcal/mol target accuracy, and the mean absolute value errors in table 4.1 are competitive with state-of-the-art solvation models in the literature. For example, the SMD (Solvation Model based on Density) solvation models give mean

we employ here is to perform a binary search to find the zero of $f(x) = x_{j+1} - x_j$.

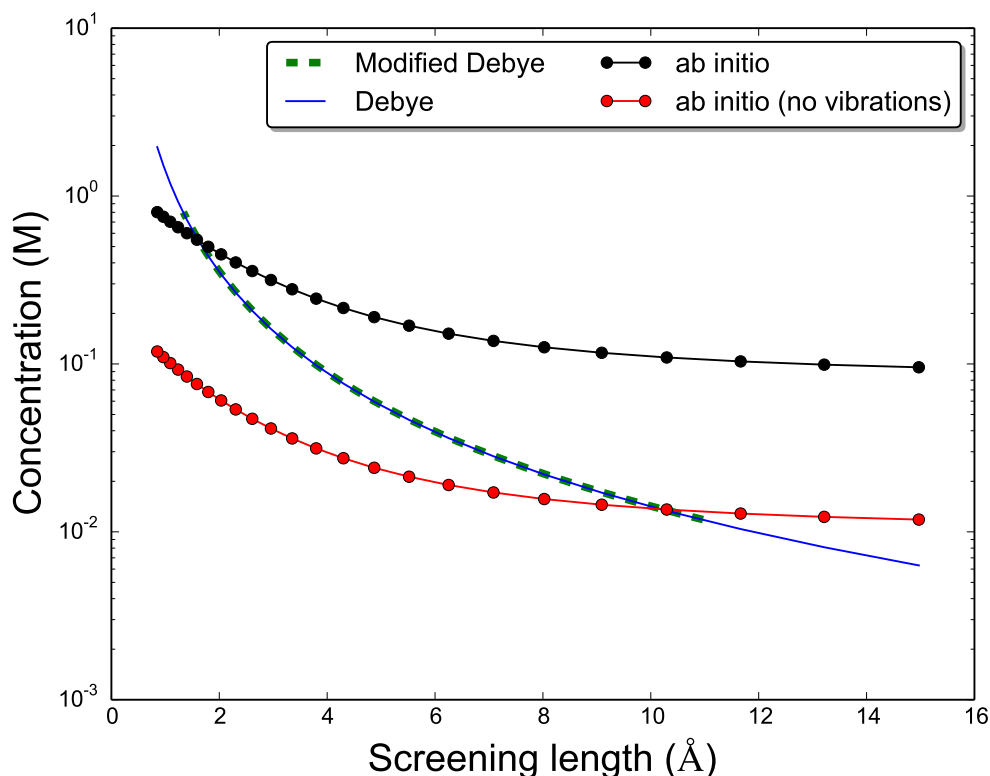


Figure 4.4: The concentration of free (mobile) ions plotted as a function of the screening length. Red and black data points show the *ab initio* results, with and without the vibrational free energy. Solid blue and dashed green lines show the same, calculated using the Debye expressions in equation 4.5 and equation 4.6 respectively. The intersection of curves correspond to self-consistent solutions. For the ab-initio results, lines between the data points are only to guide eyes.

absolute errors as high as 2.23 kcal/mol and as low as 0.20 kcal/mol, depending on the details of the model used (SMD-PGP vs SMD-GIL²) and an overall error

² SMD-PGP and SMD-GIL stand for partial generic parameters and generic ionic liquid respectively. The SMD model normally requires a large number of fluid descriptors as input (e.g. Abraham hydrogen bond acidity and basicity parameters). Such data is not readily available for the large numbers of possible ionic liquids. As such, in the SMD-GIL model the authors average over all ionic liquids for which there is data, and use those 'generic' values in their calculations. In the SMD-PGP model, generic values are used only for those parameters whose values are not known. See the work by Bernales et. al. [156] for more information.

of 0.43 kcal/mol and 0.51 kcal/mol respectively. The sensitivity of our solvation energy errors with respect to changes in the model parameters is explored in Figure 4.3.

In addition to producing solvation energies competitive with other models in the literature, our approach has distinct advantages. It can easily be implemented in a plane-wave code (as opposed to cavity-based models such as SMD) and its capabilities are not restricted to calculating solvation energies. Indeed, in the following section, we will use our theory to predict the interfacial capacitance of a solid in RTIL.

Although we found determination of the solvent parameters n_c and τ to be relatively straightforward, determination of the ion strength parameter x proved to be more subtle. Table 4.2 shows, for example, the resulting free ion concentration of the RTIL [MEIM][Tf₂N] as a function of the screening length when considering or ignoring the vibrational free energy (black and red points, respectively) and compares these results to the associated concentrations from the linear Debye screening length expression in equations 4.5 and 4.6 (blue curve and green rectangles, respectively).

Our results show foremost that vibrational free energy has a very large effect on the ion concentration, affecting it almost two orders of magnitude because this energy can change as much as $4 k_b T$ (The reason for this is explored later). On the other hand, we find that the choice among the two linear Debye theories (original and modified) essentially has no effect on the final ion concentration³. Finally, we do find that the steric interactions inherent in the nonlinear screening

³ This is because the factor $(1 - \gamma)^{-1/2}$ is nearly unity for most ionic liquids, regardless of the value of x . For example, at $x = 0.25$, $(1 - \gamma)^{-1/2}$ values for the three ionic liquids we consider here are only 1.0016, 1.0078 and 1.0171 respectively.

expression 4.9 have a noticeable lowering effect on ion concentration x (table 4.2) approaching a factor of two, but still a far weaker effect than that of the vibrational free energy.

4.3 Discussion

Table 4.2 gives our predicted dissociation fractions to be in the range 0.1 - 0.3, depending on the ions and the level of theory used, clearly establishing that the RTILs we investigate here to be strong, and not weak, electrolytes. This result is in line with the consensus view in the literature, and contrasts sharply with recent surface-force measurement experiments.

While the results in table 4.2 are in line with the consensus view, there remain noticeable difference between the values of x we compute and the molar conductivity ratios ($\Lambda_{imp}/\Lambda_{NMR}$) used in the Tokuga et. al.'s experiment [135] as a measure of x . On one hand, this is not surprising, given that dissociation fraction x depends exponentially on the dissociation energy, so that errors of just 1 kcal/mole can affect x by a factor of nearly *five* with any error in our calculation of the dissociation energy being 'exponentially enhanced'. Thus, the accuracy of our results should be judged using a logarithmic (i.e. energy) scale. Furthermore, the molar conductivity ratio, while a measure of ion aggregation, may not directly correspond to the fraction of free ions. Indeed, Tokuga et. al. themselves note [135] that $\Lambda_{imp}/\Lambda_{NMR}$ is only correlated with the fraction of free ions, and that it gives only an estimate of x because, for example, the strong interactions between the ions can affect the ionic activity, leading to a conductivity ratio different from the dissociation fraction. Moreover, given the low

	PBE (vacuum)	PBE (solv)	PBE0 (vacuum)	PBE0 (solv)
ΔE	0.054	-4.27	-0.46	-5.02
$e \frac{\Delta E}{kT}$	8.1	$\sim 10^{-72}$	$\sim 10^{-8}$	$\sim 10^{-88}$

Table 4.3: For the [MEIM][Tf₂N] RTIL, The energy difference between neutral and ± 1 charged "ion" pairs, calculated using PBE and PBE0 functionals. All energies are in electron-volts (eV). Positive numbers mean that neutral species are lower in energy whereas negative numbers mean that charged species are more stable.

energy-cost breaking up an ion pair (a few kT) and the large electric fields at the electrochemical double layer, it is possible for the concentration of ions to change appreciably when an electric field is applied (during an electrochemical impedance spectroscopy experiment), perhaps explaining why the molar conductivity ratios observed in Tokuga et. al.'s experiment are larger than the equilibrium dissociation fractions we calculate.

4.4 Solvation of metal surfaces

We now exploit our method's ability to treat periodic systems to study the solvation of a noble metal surface in a RTIL. In particular, we focus on the 111 surface of gold (Au) immersed in [MBIM][PF₆] and [MEIM][Tf₂N]. We first study the voltage-dependent differential capacitance of [MBIM][PF₆] and compare with experiments from the literature [153, 158, 168], and we then consider the voltage-dependent interfacial energy of the gold-[MEIM][Tf₂N] interface as a potential candidate for the origin of the long-ranged force observed in surface-force apparatus experiments previously interpreted to imply RTILs to be weak ionic liquids [137, 139].

To determine the differential capacitance of the gold-RTIL interface, we per-

form calculations with gold in a slab geometry including a RTIL model fluid and using a truncated coulomb kernel [122] (along the slab normal) to prevent the interactions of periodic images. The differential capacitance per unit area (C) of the metal-RTIL interface is then

$$C(V) = \frac{1}{2A} \frac{\delta Q}{\delta V} = \frac{\Delta Q/A}{\mu(Q + \Delta Q) - \mu(Q - \Delta Q)} \Big|_{Q(V)}, \quad (4.12)$$

where, $\mu(Q)$ is the chemical potential of electrons in the system, Q is the net charge of the metal slab, ΔQ is a small change in the net charge induced by changing the number of electrons in the explicit DFT calculation of the slab (here, we take $\Delta Q = 0.0025e^-$ per surface unit cell), and the factor of two accounts for the presence of two surfaces in our calculation. Note that, whereas in calculations involving a charged solid or a surface slab in vacuum the absolute reference for the potential is not necessarily well defined (even when truncated coulomb kernels are used), we have demonstrated [77] that the presence of a bulk fluid with ionic screening in the calculation does indeed define an absolute reference for the potential.

Figures 4.5 and 4.6, show our results for the charge-voltage relation and the differential capacitance respectively of the gold-[MBIM][PF₆] interface under external potential. They also show experimental measurements for a number of systems [158, 168] and the results of a molecular dynamics study [153]. We first note that a very wide range of differential capacitances are reported for [MBIM][PF₆] using different electrode materials ($\sim 3\text{-}30 \mu\text{F}/\text{cm}^2$). Indeed not only the values, but also the voltage dependencies, are very different depending on the electrode material. For gold and platinum surfaces, Silva [168], Lockett [158] and Hu [153] measure flat or mostly flat differential capacitances in the $\sim 3\text{-}10 \mu\text{F}/\text{cm}^2$ range. However, for glassy carbon electrodes, both Silva and Lockett observe a dependence on the electrode potential, with the capacitance being

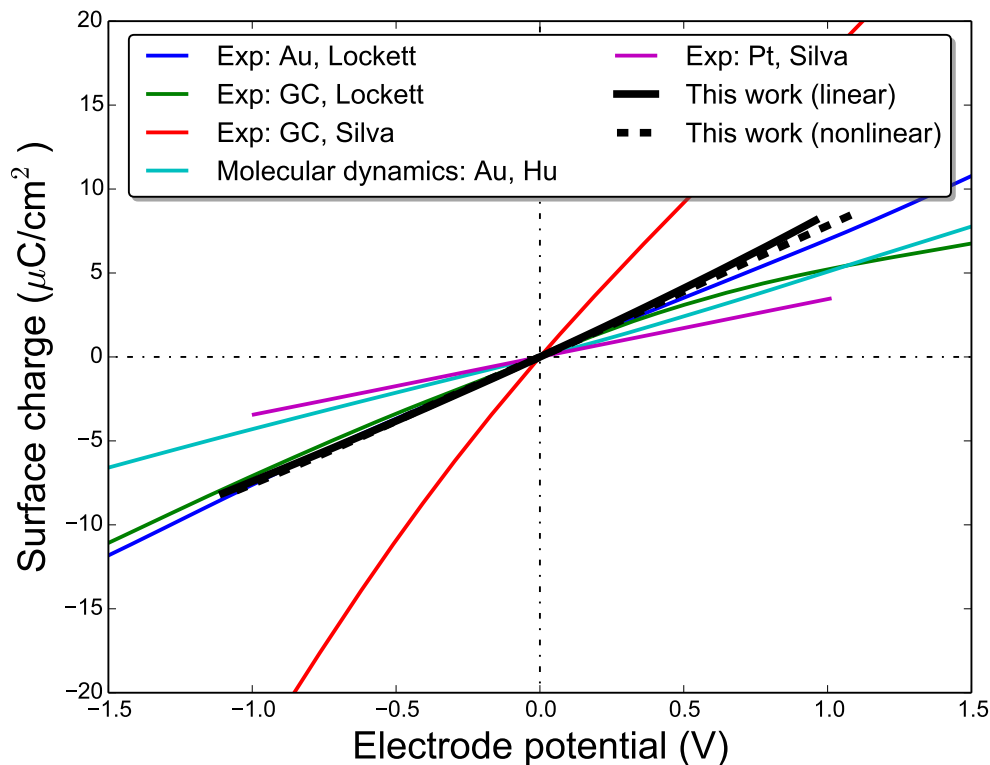


Figure 4.5: The surface charge on Au (111) surface in contact with [MBIM][PF₆] RTIL, as measured by experiments (Silva [168] and Lockett [158]), as calculated by classical molecular dynamics simulations (Hu [153]) and as calculated by us (JDFT). Au, Pt and GC stand for gold, platinum and glassy carbon electrodes respectively. We determined surface charge by integrating capacitance (see Figure 4.6) over the potential.

lower at positive and higher for negative potentials. However, Silva measures a much larger capacitance ($\sim 15\text{-}30 \mu\text{F}/\text{cm}^2$) than Lockett ($\sim 3\text{-}8 \mu\text{F}/\text{cm}^2$).

Our results indicate that the steric effect in the non-linear theory makes a noticeable impact on the electrochemical behavior, particularly on the differential capacitance. Including these effects, we predict a nearly-constant differential capacitance, in good agreement with the measurements performed by Lockett

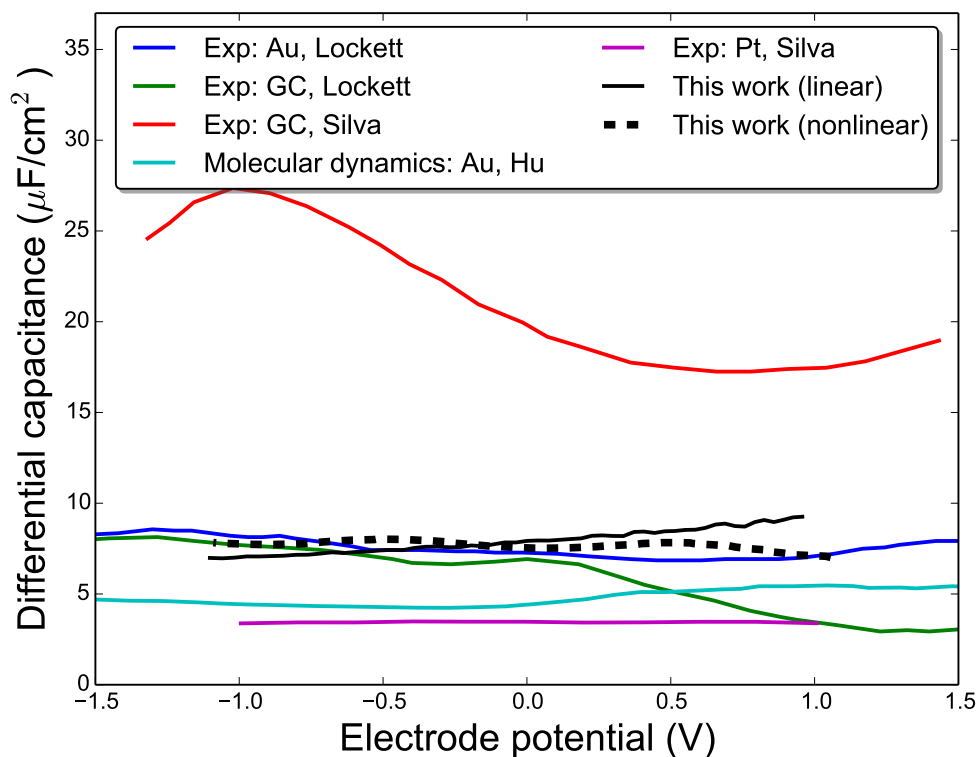


Figure 4.6: The differential capacitance of [MBIM][PF₆] RTIL, as measured by experiments (Silva [168] and Lockett [158]), as calculated by classical molecular dynamics simulations (Hu [153]) and as calculated by us (JDFT). Au, Pt and GC stand for gold, platinum and glassy carbon electrodes respectively.

with a gold electrode. Both Lockett's measurement and our calculations predict capacitances that are higher than those predicted by classical molecular dynamics [153]. Finally, we note that both our linearized theory and the molecular dynamics results exhibit an apparent artifact of increased capacitance at higher potentials.

There are a number of reasons why experiments might exhibit such a large range of capacitances for the same ionic liquid. Even noble metal surfaces in

ionic liquids are known to reconstruct at applied potentials [169], and any resulting surface roughness would affect the differential capacitance inferred from experiment. In addition, it is well known that extracting DC capacitance from AC impedance measurements is not straightforward and might introduce artifacts of its own [170]. These effects depend very strongly on the experimental conditions and setup, making comparison of capacitances from different experiments non-trivial. Finally, some surfaces may exhibit specific adsorption of ions, which we have not considered here. Nevertheless, our results show impressive agreement.

Finally we consider [MEIM][Tf₂N], one of the ionic liquids present in the recent surface force apparatus experiments [139] whose authors challenged the consensus view of RTILs as strong electrolytes by measuring long (multi-nanometer) Debye screening lengths. Here, we present evidence suggesting that the apparent long-ranged tail of the force between two charged surfaces could have arisen instead from a change in the wetted surface area.

We begin by calculating the change in the energy of the system as more surface is wetted. We calculate this surface solvation energy as

$$F_{\text{sol}}(V) = F(0) - E_{\text{vac}} - \int_0^{Q(V)} V'(q) dq, \quad (4.13)$$

where E_{vac} is the energy of the surface in vacuum, $F_{\text{sol}}(0)$ is the energy of the *neutral* surface in RTIL and $V(q)$ is the potential of the surface in charge state q . The final term represents the total free-energy stored in the electrochemical double-layer.

Figure 4.7 shows the resulting charging curve and the surface solvation energy in black and red respectively for gold 111 in [MEIM][Tf₂N]. The maximum surface energy occurs at the potential of zero charge, with a value of ap-

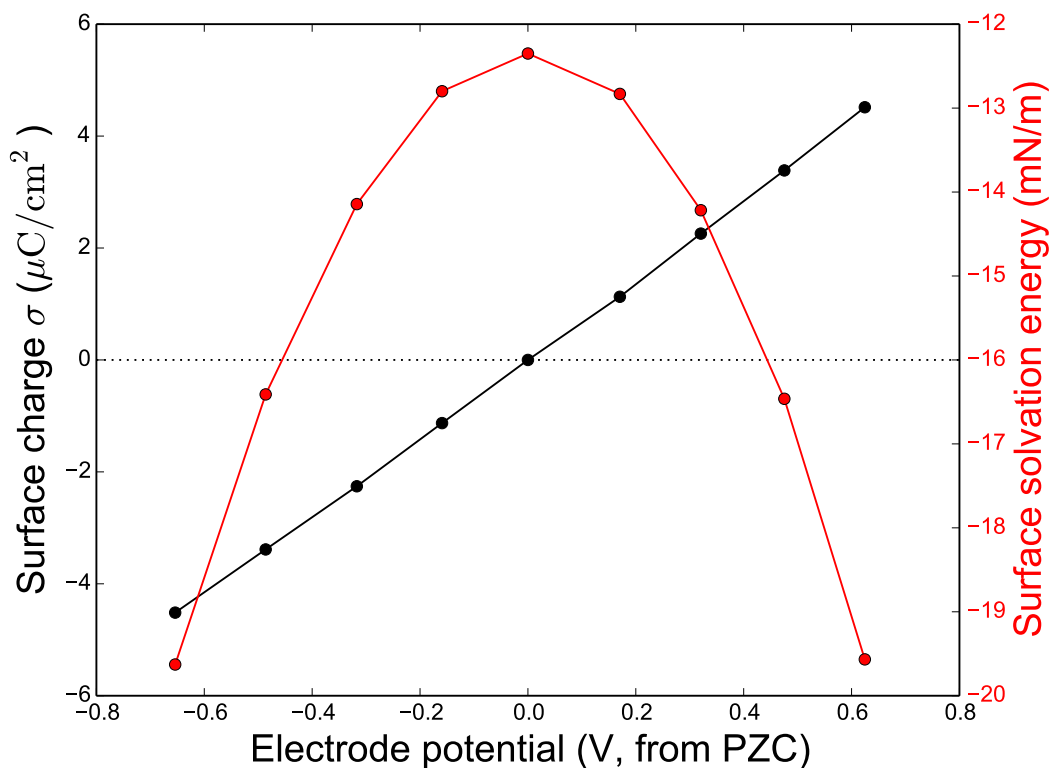


Figure 4.7: In black, is the charging curve of the [MEIM][Tf₂N] RTIL in contact with a gold (111) electrode. In red, is the surface solvation energy (per unit area), as a function of the electrode potential. Lines are only to guide eyes.

proximately 12.5 mN/m. The surface solvation energy becomes more negative (nearly quadratically) as the voltage varies from the PZC, indicating stronger wetting as the surface charges. For the relevant electrochemical window, we observe that the energy gained (per unit area) by wetting the gold 111 surface is in the range of 12 to 20 mN/m.

Gebbie et. al. [139], for the same ionic liquid, measure a long-ranged tail of the F/R ratio with a peak value of approximately 1 mN/m. Given that the radii of curvature for the surfaces they use are ~ 5 cm, and assuming the Derjaguin

approximation [171], we conclude that the peak forces they measure are ~ 0.05 mN. Assuming that the surface solvation energy is 20 mN/m, we see that the same force could have arisen from the wetting of a cylindrical probe of radius ~ 0.4 mm. Given the dimensions of the experimental apparatus, we believe that this wetting effect is of sufficient size to mimic the apparent long-ranged interaction observed. While this analysis does not, in any way conclusively prove that wetting is the mechanism behind the long-ranged tail observed in experiment, our results do indeed suggest that this avenue is worth pursuing.

4.5 Conclusion

In summary, we here develop a fully self-consistent continuum solvation theory of room-temperature ionic liquids (RTILs) based on joint density-functional theory. This theory, tested with three different RTILs, is accurate to 0.5-0.6 kcal/mol for the solvation energy of neutral solutes. Our approach also sheds light on the ongoing controversy in the literature on the atomistic structure of RTILs. Free energies of ion-pair binding energies we calculate using our new theory, once vibrational free energies are accounted, are in agreement with the consensus view that RTILs are strong electrolytes and offer evidence against the recent surface force apparatus measurements that claim otherwise. Furthermore, our results also offer physical evidence against a popular approach in the literature that assumes partial effective charges on the individual ions. Finally, exploiting our technique's ability to handle periodic systems, we study the behaviour of a noble metal surface in RTILs finding that the steric effects have a measurable effect on the interfacial capacitances of RTILs, and that the inclusion of steric effects improve the agreement between theory and experiment.

4.6 Appendix A: Importance of the vibrational and zero-point energy

As mentioned above, the total vibrational free-energy changes appreciably between the paired and the dissociated state. Most other studies of solvated species do not consider this effect as changes in the vibrational energy of molecules tend to be small compared to the total solvation energy. In this study of ion-pairings in RTILs, likely due to the large size of each ion and the unusual nature of the vibrational coupling between large ions, (compared to the small molecular systems studied in previous works), we find that the changes in vibrational energies can no longer be ignored safely.

Here, we first calculate the eigenvalues (and frequencies ω_j) of the vibrational modes using a Hessian determined by central finite differences. The total vibrational free energy neglecting vibrational couplings is then

$$F_{\text{vib}} = \sum_j \left[\frac{1}{2} \hbar \omega_j + kT \ln \left(1 - e^{-\frac{\hbar \omega_j}{kT}} \right) \right] \quad (4.14)$$

where the first term in the summation is the zero-point energy and the summation is performed over all the vibrational modes in the ion or ion pair (indexed by j).

To determine the origin of the change in the vibrational energy, Figure 4.8 shows, for the [MEIM][Tf₂N] RTIL, net change in each vibrational mode's energy with positive values indicating larger mode energies for dissociated ions, along with an accumulated sum. This analysis shows a net decrease in dissociated vibrational energy (and thus a higher ionic strength) coming from the aggregate of many (small) changes in modes from the lower partition of the spectrum

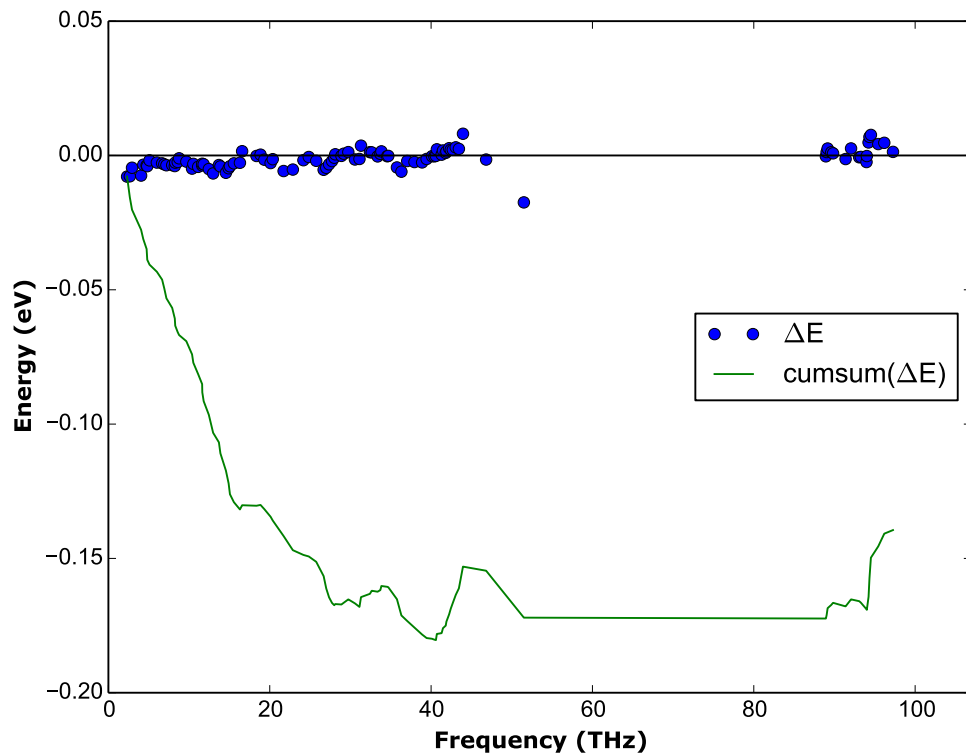


Figure 4.8: The change in the vibrational modes of an [MEIM][Tf₂N] ion pair: The blue curve shows the change in the eigenvalue for each vibrational mode, a positive value meaning that the bound ion pair has a smaller eigenvalue than dissociated ion pair. The green curve is the cumulative sum of the blue curve. Eigenvalues are sorted, ascending in energy.

($\hbar\omega < 0.15$ eV), which we associate with longer wavelength vibrations of our large ions becoming stiffer in the bonded state.

4.7 Appendix B: Possibility of fractional (non-integer) effective ion charges

Some authors have suggested the possibility of non-integer, or less than unity, effective charges on the dissociated ions [150, 151, 152, 157], because, for example, such charges can help classical force-field models reach better agreement with experimental measurements of physical properties such as viscosity [150]. There seems to be further support for this proposition from *ab initio* calculations. For example, Holloczki et. al. [150] have performed DFT calculations with the Conductor-like Screening Model (COSMO [172]) and found that the ionic charges that minimize the total energy are in the range of ($\pm 0.5 - 0.8$) for most ionic liquids.

Due to quantization of charge, microscopically, this can only happen if some fraction of the dissociated pieces ("ions") are ± 1 charged while others are neutral. For example, the [MEIM][Tf₂N] ionic liquid is typically thought to dissociate into [MEIM]⁺ and [Tf₂N]⁻, but such fractionalization would require also the presence of [MEIM]⁰ and [Tf₂N]⁰ in the fluid.

Here, we argue instead that this picture is inconsistent with the free energies needed to stabilize the ions and the neutral species within the fluid. Our calculations for the [MEIM][Tf₂N] RTIL indeed confirm that the neutral species have lower energy in vacuum (table 4.3, second column) only within the semilocal exchange-correlation functionals used by us (and by Holloczki et. al. [150]) but not within more accurate hybrid functionals such as PBE0 (table 4.3, fourth column), which correct the self-interaction errors that destabilize negative ions within semilocals. Moreover, we note that charged species are even more stabi-

lized by screening when solvated in an ionic liquid (table 4.3, third column), to where any errors introduced by the semilocal exchange-correlation functional are dwarfed by the solvation energy, which is about an order of magnitude larger.

These results, lend support to an alternative explanation for the apparent charge fractionalization [151], which argues that it is not neutral species in solution which give rise to the effective fractional ionic charges, but rather the high-frequency dielectric response of the ionic liquid. The high-frequency dielectric constant of most ionic liquids are in the range 1.5 - 2.0, implying that, as far as the timescales relevant to molecular motion is concerned, the interaction of any two charges in the ionic liquid are already screened by the electron rearrangements within the solvent molecules, the effect of which can be absorbed into reduced effective charges in the molecular dynamics simulations; consistent with the observation that molecular dynamics simulations with polarizable force fields (but unit charges) also predict accurate viscosities [151].

4.8 Appendix C: Computational/numerical details

All DFT calculations in this section were performed with JDFTx [173], an open-source implementation of plane-wave density-functional theory. We used PBE functional to treat the electronic exchange and correlation [174], Grimme's correction for dispersion interactions [65], a plane-wave basis set with a cutoff of 30 Hartrees and a truncated Coulomb kernel [122] to prevent the interaction of periodic images. Vibrational energies were computed using central finite differences.

Species	R (Å)
[MEIM] ⁺	3.84
[MBIM] ⁺	4.19
[OMIM] ⁺	4.74
[PF ₆] ⁻	3.37
[Tf ₂ N] ⁻	4.23
[MEIM][Tf ₂ N]	5.00
[MBIM][PF ₆]	4.72
[OMIM][PF ₆]	5.15
Na ⁺	1.59
Cl ⁻	2.96

Table 4.4: The hard sphere radii for the different species. Values for Na⁺ and Cl⁻ have been included for comparison purposes.

We approximated the hard-sphere radius R of each ion or ion pair (used in equation 4.6) by integrating the total volume of each solvent molecule up to a specific critical electron density contour. The value for the critical electron density is $n_c = 1.8 \times 10^{-4} a_0^{-3}$ (in atomic units), which we have previously shown to give an accurate estimation of the volume-of-exclusion parameter in the van der Waals equation of state [175]. Numerical values for the species relevant here are given in table 4.4.

Compared to the linear ionic theory, the fully nonlinear Poisson-Boltzmann is significantly more involved as it introduces new degrees of freedom ($\eta_j(\vec{r})$'s) over which the free energy expression must be minimized. Furthermore, the singularity in the FMT-like term in equation 4.9 introduces a numerical problem that must be handled. In our case, we use nonlinear conjugate gradients to minimize over the fluid degrees of freedom. We note that for this method to be stable, the algorithm must backtrack and reduce the step size if η goes over the hard-sphere packing limit during the line search.

CHAPTER 5
ELECTRONIC EXCITED STATES FROM STATIONARY-POINT
KOHNSHAM THEORY¹

Density functional theory (DFT) [176, 177], while extremely powerful in the prediction of many ground state properties, has not been as capable in predicting properties of electronic excitations [178]. As evidenced by many previous attempts to extend DFT to treat excited states [179, 180, 181, 182, 183, 184, 185], the ability to predict electronic excitations accurately and efficiently is crucial for many applications in condensed matter physics, materials science and chemistry. Straightforward applications of density-functional theory often result in very poor results, while more sophisticated approaches built upon DFT can increase the computational cost by several orders of magnitude.

This work discusses stationary-point density-functional theory (SPDFT), a very simple yet powerful framework for calculating excited state energies and electron densities. In the simplest approximation to this approach, one enforces a fillings structure that does not have a Fermi-Dirac form during self-consistent field (SCF) calculations. Within this approximation, this corresponds to the Δ SCF method used to calculate electron affinities and ionization energies; indeed, several works refer to SPDFT as Δ SCF [186, 187, 188]. In varying forms and in diverse communities, such approaches have been used for many years [186, 188, 189, 187, 190, 191, 192, 193, 194, 195]. For example, x-ray absorption spectroscopy community uses this approach to calculate the core-hole effect [192, 193]. However, stationary-point density-functional theory has not found nearly as widespread acceptance in the electronic structure community

¹Co-author credits: This work was done in collaboration with Ravishankar Sundararaman and Megan Holtz. All experimental uv-vis measurements were performed by Megan Holtz.

as, for example, time-dependent density-functional theory has and the theoretical foundations of this alternative approach have not been explored in similar depth.

The contributions of this work are as follows. The first section argues that using Δ SCF for calculating electronic excitations can indeed be put on a rigorous basis and corresponds specifically to one particular approximation to finding the stationary points of the generalized Hohenberg-Kohn energy functional, which are known to give exactly a subset of the excited states of an electronic system [196]. Next, we benchmark the method against the most popular excited states methods in the electronic structure community, GW and TDDFT, for a wide class of systems (including multi-determinant systems, localized and extended systems) and identify the inherent advantages and limitations of the approach. We then go on to propose a new algorithm to overcome common numerical instabilities that plague Δ SCF particularly in degenerate open-shell systems. Last, we propose possible avenues for potential future improvements to the method.

5.1 Existing excited-state methods

The field of excited-state methods in density-functional theory has a long history, and the literature on the subject is too broad to fully outline here. Instead, to put our work in context, we briefly discuss those approaches most relevant to our work.

Because the excited-state problem is challenging due to the self-interaction error in the mean-field term, one popular approach prescribes mixing some

Hartree-Fock exchange into the exchange-correlation function where the non-local exchange operator partially remedies the problem. Such hybrid functionals have been very successful in the prediction of bandgaps of solids [181, 182, 197, 198]; however, the computation of the exchange operator is very computationally demanding, especially in plane-wave calculations. The approach we describe here does not require the evaluation of the Fock operator, and thus scales better than hybrid functionals.

Another set of approaches are the techniques based on Green's function methods, like GW and Bethe-Salpeter methods [179]. These have been very successful in extended systems, and show promise in molecules as well [199], but also typically demand much more computational resources than the ground-state problem, frequently requiring a computation over thousands of empty bands and k-points [200] and proving to be even more expensive than the hybrid functional approach. In contrast, the method we discuss here only requires marginally larger number of bands than the ground-state calculation.

Yet another alternative is Time Dependent Density-Functional Theory (TDDFT), which is based on calculating the time-dependent response of the electron density to a periodic perturbing potential. TDDFT has proved to be very accurate in describing excitations in molecular systems and is significantly more efficient than more the sophisticated many-body techniques, and, with highly specialized computational methods, begins to approach the cost of non-hybrid ground state calculations [180, 201]. Nevertheless, TDDFT has difficulty with the bandgap of extended (bulk solid) systems, and with charge-transfer excitations [202, 203, 204]. Below, we demonstrate that contrary to what some authors suggest [186], the method we discuss here is distinct from and generally

more accurate than TDDFT, albeit also failing, under current known approximations, to resolve the bandgap problem in extended systems.

A fourth kind of approach is that of orbital-dependent functionals, where the exchange-correlation energy is made an explicit functional of the Kohn-Sham orbitals. These methods have a long history going back to the Perdew-Zunger self-interaction correction [205], and have recently been gaining in popularity and are also under active development [206].

5.2 Theory

In the self-consistent field (SCF) method, an initial set of orbitals is used to construct the Kohn-Sham Hamiltonian, which is then solved to construct a new and hopefully improved set of Kohn-Sham orbitals and total electronic density, and this process is repeated until self-consistency. During this iterative procedure, orbitals are generally considered occupied, or 'filled', according to the Aufbau principle; i.e. those with lower eigenvalues are filled before the those with higher eigenvalues, until all electrons are accounted.

In the Hartree-Fock and DFT communities, it has been proposed that enforcing a non-Aufbau fillings structure during SCF can be a way to access excited states [186, 188, 189, 187, 190, 191, 192, 193, 194, 195]. At each SCF step, instead of filling the lowest single-particle orbitals, or filling states with a Fermi-Dirac distribution (accomplishing essentially the same result), the orbitals are occupied in a non-Aufbau (or non-Fermi-Dirac) fashion so as to leave holes in the electronic structure. For example, in a two-electron, two-orbital system, one could find the lowest energy optical excitation (ΔE) by promoting an electron from the

lower energy orbital to the higher energy orbital, and then subtracting the total self-consistent energies of the excited and ground states to obtain the *excitation* energy.

$$\Delta E = E_{\text{tot}} \left(\begin{array}{c} \text{---} \uparrow \\ \text{---} \uparrow \end{array} \right) - E_{\text{tot}} \left(\begin{array}{c} \text{---} \\ \text{---} \uparrow \end{array} \right).$$

When the Hartree-Fock method is viewed as a variational approximation to the many-body wavefunction, this procedure is equivalent to finding the stationary points of the total energy functional in the subset of the full the Hilbert space consisting of all single Slater determinants. Therefore, in the context of the Hartree-Fock approximation, the ΔSCF method has a rigorous basis, within which the approximation being made is clear. There is, however, no immediately obvious way to justify such a procedure within density-functional theory, except for the fact that it somehow does give good results [186, 191]. In order to explain this observation, Kowalczyk et. al. [186] have suggested that, within density-functional theory, this procedure somehow is related to an adiabatic approximation of time-dependent density functional theory. However, our results below indicate that subtraction of non-Aufbau total energies yields excitation energies that differ significantly from and generally more accurate than TDDFT energies. Moreover, below we argue that this ΔSCF procedure, within DFT, finds the stationary points of a well-defined approximation to the Hohenberg-Kohn functional, whose stationary points should, in principle, give the exact energies and electron densities of the corresponding excited states.

We present our argument for this in three stages: First, we review how, as proved some 30 years ago by Perdew and Levy [196], the stationary points of

the *pure-state* (as opposed to *ensemble*) Hohenberg-Kohn energy functional $E[n]$, i.e. the densities for which $\delta E/\delta n = 0$, correspond to stationary points of the many-body energy functional $\langle \Psi | \hat{H} | \Psi \rangle$ and thus to *some* of the excited states of the many-body system. We then extend Perdew and Levy's approach so as to be able to capture *all* excited states of a many-body system, demonstrating in the process that more recent findings on how a single density may be an excited state for multiple potentials [207] presents no difficulty for the framework we propose. Finally, we show how to extend Perdew and Levy's connection between Hohenberg-Kohn stationary points and Kohn-Sham orbitals to our approach, demonstrating that solution to the self-consistent Kohn-Sham equations in an appropriate external potential indeed corresponds to the relevant stationary points.

5.2.1 Stationarity of the Hohenberg-Kohn functional

In his classic paper [9], Levy proposed the following form for the Hohenberg-Kohn energy functional [176]

$$E[n(\vec{r})] = \min_{\Psi \rightarrow n(\vec{r})} (\langle \Psi | \hat{T} + \hat{U}_{ee} | \Psi \rangle) + \int n(\vec{r}) V(\vec{r}) d^3r \quad (5.1)$$

$$= F[n(\vec{r})] + \int n(\vec{r}) V(\vec{r}) d^3r, \quad (5.2)$$

where $\min_{\Psi \rightarrow n(\vec{r})}$ is a minimization over all wavefunctions Ψ that give the electron density $n(\vec{r})$. The minimum of $E[n(\vec{r})]$ then gives the energy and electronic density of the ground state. Perdew and Levy later showed that not only the minimum, but also the stationary points have physical meaning and that they corresponded to (some of the) excited states [196]. This is much less known than the original Levy constrained search procedure, so we shall provide a descrip-

tion here, with generalizations that enable locating all of the excited electronic states of the system.

According to the Rayleigh-Ritz variational principle, the eigenfunctions (Ψ_j) of the many-body hamiltonian (\hat{H}) are in one-to-one correspondence with the stationary points of the many-body energy functional,

$$\left. \frac{\delta}{\delta\Psi} \langle \Psi | \hat{H} | \Psi \rangle \right|_{\Psi_j} = 0 \quad \text{where} \quad \hat{H}\Psi_j = E_j\Psi_j, \quad (5.3)$$

where, $\Psi(\vec{x}_1, \vec{x}_2, \dots)$ is the many body wavefunction, and $\delta\Psi$ is any norm and anti-symmetry conserving variation in Ψ .

We extend Perdew and Levy's work by defining the set of many-body wavefunctions $\Psi^{(\alpha)}[n]$ for each density $n(\vec{r})$ that make the internal energy, $F = \langle \Psi | \hat{T} + \hat{V}_{ee} | \Psi \rangle$ stationary *within* the manifold of normalized and anti-symmetric Ψ that yield the density n . Due to this construction, the projection of the wavefunction gradient of the internal energy F and the total energy E (i.e. $\frac{\delta E}{\delta\Psi}$ and $\frac{\delta E}{\delta\Psi}$) to the tangent space of this manifold of constant electronic density is zero (Because n is constant over the manifold, $\frac{\delta n}{\delta\Psi} = 0$ for these variations). Figure 5.1 illustrates this as the geometric fact that $\frac{\delta E}{\delta\Psi}$ is normal to the constant- n manifolds (illustrated as $d = 1$ manifolds) at the identified stationary points $\Psi^{(\alpha)}[n]$ on these manifolds. For some, but certainly not all, $\Psi^{(\alpha)}[n]$, the remaining components of the gradient $\frac{\delta E}{\delta\Psi}$ (along the dimensions normal to the constant n manifold) will also be zero, making those particular $\Psi^{(\alpha)}[n]$ stationary points of the total energy, and therefore eigenfunctions of the many-body hamiltonian. We argue next that this occurs precisely for those $\Psi^{(\alpha)}[n]$ whose corresponding density n makes a new, generalized Hohenberg-Kohn functional stationary. We later argue that the stationary points of this generalized function indeed capture *all* of the excited states of the system.

To generalize the Hohenberg-Kohn energy functional in (5.1), we replace the minimization in the internal energy term with the finding of stationary points,

$$E^{(\alpha)} [n(\vec{r})] \equiv \text{stat}_{\Psi \rightarrow n(\vec{r})}^{(\alpha)} \langle \Psi | \hat{T} + \hat{V}_{ee} | \Psi \rangle + \int n(\vec{r}) V(\vec{r}) d^3r \quad (5.4)$$

$$= F^{(\alpha)} [n(\vec{r})] + \int n(\vec{r}) V(\vec{r}) d^3r. \quad (5.5)$$

Note that, in general, there is no unique stationary point and so the $\text{stat}^{(\alpha)}$ operator in (5.5) enumerates these points in a consistent way so that each associated $\Psi^{(\alpha)}[n]$ is a continuous function (at least over some neighbourhood of all n but for a set of measure 0). By convention, we shall always associate $\alpha = 0$ with the minimum value of the internal energy functional. We thus now have defined a new collection (enumerated by α) of Hohenberg-Kohn internal and total energy functionals $F^{(\alpha)} [n(\vec{r})]$ and $E^{(\alpha)} [n(\vec{r})]$ respectively.

Now consider a stationary point in $E^{(\alpha)} [n(\vec{r})]$, so that, to first order, $\delta E = E^{(\alpha)} [n + \delta n(\vec{r})] - E^{(\alpha)} [n(\vec{r})] = 0$ for all physical δn . From the above definition of $\Psi^{(\alpha)}[n]$, it is already clear that $\frac{\delta E}{\delta \Psi} (\Psi^{(\alpha)}[n]) = 0$ has zero component in the tangent space to the constant- n manifold. From figure 5.1, the normal space to the manifold at $\Psi^{(\alpha)}[n]$ is actually the the tangent space to $\Psi^{(\alpha)}[n]$ viewed as a function of n , so that any normal component to $\frac{\delta E}{\delta \Psi}$ would correspond to $\frac{\delta E^{(\alpha)}}{\delta n}$ and thus be zero, making $\Psi^{(\alpha)}[n]$ an excited state. Algebraically, if we consider any variation $\delta \Psi$, we may always define the associated density change $\delta n \equiv n(\Psi^{(\alpha)}[n] + \delta \Psi)$, an associated out-of-manifold variation $\delta \Psi_{\perp} \equiv \Psi^{(\alpha)}(n + \delta n) - \Psi^{(\alpha)}(n)$ and an associated tangent-space variation $\delta \Psi_{\parallel} = \delta \Psi - \delta \Psi_{\perp}$. Note that, to first order,

$$\begin{aligned} n(\Psi^{(\alpha)}[n] + \delta \Psi_{\parallel}) &= n(\Psi^{(\alpha)}[n] + \delta \Psi - \delta \Psi_{\perp}) \\ &= n(\Psi^{(\alpha)}[n] + \delta \Psi) - (n(\Psi^{(\alpha)}[n] + \delta \Psi_{\perp}) - n(\Psi^{(\alpha)}[n])) \\ &= n + \delta n - (n + \delta n - n) \\ &= n \end{aligned}$$

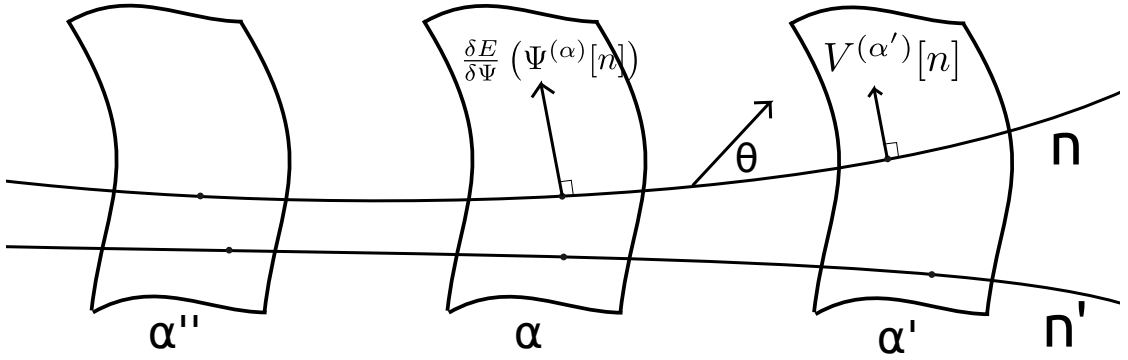


Figure 5.1: Cartoon representing the Hilbert space. The three surfaces represent subspaces formed by $\Psi^{(\alpha)}[n]$ for different n and α . Horizontal curves represent contours of constant electronic density n . The arrows represent the direction of the gradient of total energy wrt changes in the wavefunction. For wavefunctions belonging to one of the α -subspaces, this gradient is non-zero only in-plane, i.e. in the tangent space of the constant-density contour (this is shown with a perpendicular sign). For these wavefunctions, there exists some potential $V^{(\alpha)}$ that cancels this component exactly, making it an eigenfunction of the many-body hamiltonian. For an arbitrary wavefunction that is not necessarily in an α plane, the gradient is free to have non-zero components in all dimensions. This is illustrated with an angle θ between the gradient and the constant-density contour.

Finally, $\frac{\delta E}{\delta \Psi} \delta \Psi = \frac{\delta E}{\delta \Psi_{\parallel}} \delta \Psi_{\parallel} + \frac{\delta E}{\delta \Psi_{\perp}} \delta \Psi_{\perp} = 0$ because the parallel component is zero by the definition of $\Psi^{(\alpha)}[n]$ and the perpendicular component is $E(\Psi^{(\alpha)}[n] + \delta \Psi_{\perp}) - E(\Psi^{(\alpha)}[n]) = E[n + \delta n] - E[n] = 0$ from the stationarity of $E[n]$.

Alternately, all excited states, i.e. stationary points of E with respect to Ψ , are also stationary points of $E^{(\alpha)}[n]$. This follows directly because all stationary points of $E(\Psi)$ are also stationary within the corresponding n -manifold, and thus appear as $\Psi^{(\alpha)}[n]$ for some α , and all off-manifold variations are clearly also zero so that $\frac{\delta E}{\delta n} = 0$. Algebraically, $\delta E = E[n + \delta n] - E[n] = \frac{\delta E}{\delta \Psi} [\Psi^{(\alpha)}[n + \delta n] - \Psi^{(\alpha)}[n]] = 0$ because $\frac{\delta E}{\delta \Psi} = 0$. Thus all stationary points of $E^{(\alpha)}[n]$

are in one-to-one correspondance to excited states.

The empirical evidence in the literature that excited-state potentials are not unique, and that a single density can be an excited-state of different potentials (and hence have different energies) [207] is fully consistent with and presents no difficulty for the findings above. Within our framework, this happens when the same density n happens to be a stationary point of the Hohenberg-Kohn functional $E^{(\alpha)}[n]$ for two different values of α .

5.2.2 Stationarity of the Kohn-Sham functional

Kohn-Shamification of the Hohenberg-Kohn functional begins by considering the Hohenberg-Kohn internal energy functional for the non-interacting system, whose energy is then purely kinetic. For the ground state case,

$$T [n (\vec{r})] = \min_{\Psi \rightarrow n(\vec{r})} \langle \Psi | \hat{T} | \Psi \rangle, \quad (5.6)$$

where the single-body nature of the operator \hat{T} ensures that Ψ may be selected to be a single Slater determinant. When a non-aufbau occupancy structure is forced on the calculation, the kinetic energy at self-consistency is no longer minimum at that density, but rather stationary [195], and so corresponds to

$$T^{(\alpha)} [n (\vec{r})] \equiv \text{stat}_{\Psi \rightarrow n(\vec{r})}^{\alpha} \langle \Psi | \hat{T} | \Psi \rangle, \quad (5.7)$$

where α denotes an index of the stationary state corresponding to the occupancy structure. By doing this, we have introduced α dependence to the Hohenberg-Kohn functional $E^{(\alpha)}$.

Generalizing Kohn and Sham, we then define $F^{(\alpha)}[n] = T^{(\alpha)}[n] + E_H[n] + E_{xc}^{(\alpha)}[n]$,

where the mean field Hartree energy is explicitly

$$E_H = \frac{1}{2} \int \int \frac{n(\vec{r})n(\vec{r}')}{|\vec{r} - \vec{r}'|} dr dr' \quad (5.8)$$

and the exchange-correlation functional is defined formally and exactly as

$$E_{xc}^{(\alpha)}[n] = E^{(\alpha)}[n] - T^{(\alpha)}[n] - E_H[n]. \quad (5.9)$$

The resulting variational principle is then equivalent to solving self-consistent single particle equations with non-Aufbau occupancies in a potential given by the sum of the external potential, the traditional Hartree potential and the variational derivative $\frac{\delta E_{xc}}{\delta n}$.

Note that there is now an additional α dependence in the exchange correlation functional. Ideally, we would index $E_{xc}^{(\alpha)}[n]$ to correspond to the same particle-hole excitations as implicit in the indexing $T^{(\alpha)}[n]$ so as to minimize the α -dependence of $E_{xc}^{(\alpha)}[n]$. Indeed, in the calculations in the next section, we will approximate $E_{xc}^{(\alpha)} \approx E_{xc}^{(0)}$, where $\alpha = 0$ denotes the ground state exchange-correlation functional. The accuracy of the resulting calculations lead us to believe that $T^{(\alpha)}$ alone does an acceptable, albeit imperfect, job in capturing the α dependence of $E^{(\alpha)}$.

Finally, this framework allows us to positively identify Δ SCF as a specific approximation to an *exact* underlying theory. Imposing a non-Aufbau fillings structure during SCF iteration in density-functional theory is precisely equivalent to finding the stationary-states of the generalized Hohenberg-Kohn functional under the approximation that $E_{xc}^{(\alpha)} \approx E_{xc}^{(0)}$.

#	ΔE_{KS}	ΔE_{stKS}	$\Delta E_{\text{stHK}} \text{ (pure)}$	ΔE_{exp}	$\Delta E_{\text{TDDFT}(6-311++G^{**})}$	$\Delta E_{\text{TDDFT}(\text{plane-wave})}$ [209]	ΔE_{BS} [199]	ΔE_{CASSCF} [210]
1	6.19	6.96	6.96	7.00	6.07	5.96	-	-
2	6.19	7.15	7.33	7.40	6.43	6.27	7.24	7.58
3	7.59	8.73	8.73	8.90	7.73	-	-	-
4	7.59	8.81	8.88	9.10	7.87	7.67	-	-
5	7.83	9.21	9.21	9.30	8.11	-	-	-
6	7.83	9.44	9.66	9.70	8.61	7.88	9.62	9.80
7	8.13	9.69	9.69	9.81	9.76	-	-	-
8	8.13	9.72	9.75	9.96	10.03	-	10.07	10.45

Table 5.1: First 8 excited states of the H₂O molecule. ΔE_{KS} is Kohn-Sham eigenvalue difference, ΔE_{stHK} is stationary-point Hohenberg-Kohn theory within NAKEA, ΔE_{TDDFT} is Tamm-Dancoff Time-Dependent DFT (performed with a 6-311++G** and plane-wave basis sets [209]), ΔE_{BS} is GW/BSE [199], ΔE_{CASSCF} is complete active space self-consistent field [210] and ΔE_{exp} is the experiment [208]. All DFT calculations were performed with the PBE exchange correlation functional [14].

5.3 Finite vs extended systems

Applications of stationary-point density-functional theory (SPDFT) within the non-Aufbau kinetic energy approximation (NAKEA) yield very good results for small molecules. To illustrate this, Table 5.1 and figure 5.2 compare the results for the first eight excited states of the water molecule against electron impact experiments [208] and other theoretical approaches [199, 209, 210]. The mean absolute error for the NAKEA is only 0.19 eV, significantly improving ground-state Kohn-Sham eigenvalues and well outperforming TDDFT. These results improve significantly even further after the spin purification scheme detailed in the next section, which decreases the mean absolute error to 0.12 eV. In this example, the only standard approaches which are competitive are the far more computationally demanding Bethe-Salpeter and CASSCF approaches.

Unfortunately, this success in small molecular systems does not continue for extended systems. Like TDDFT, bandgaps of solids with NAKEA revert to the

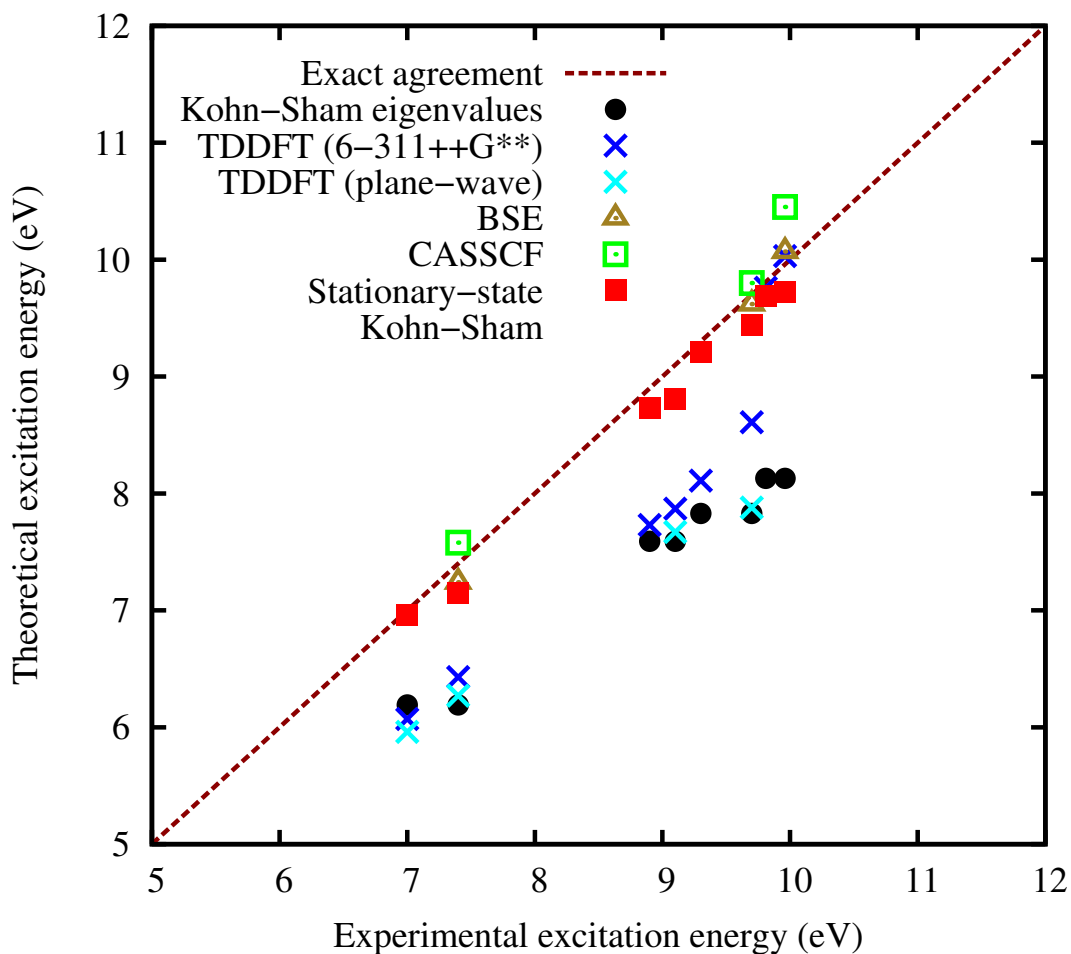


Figure 5.2: The first 8 excited states of the water molecule, calculated with different levels of theory. Raw data and references are in table 5.1.

Kohn-Sham gap of the ground state. Intriguingly, however, this reversion is much slower for NAKEA as system size increases. For example, in the case of the wide-bandgap insulator LiF, the experimental bandgap is 13.6 eV whereas the Kohn-Sham and NAKEA gaps we compute to be 8.4 eV. Figure 5.3 shows the convergence of the two methods to the same value with increasing k-point sampling. The scaling with $1/N_k^3$ (equivalently, one over the supercell volume) strongly suggest a volume scaling effect.

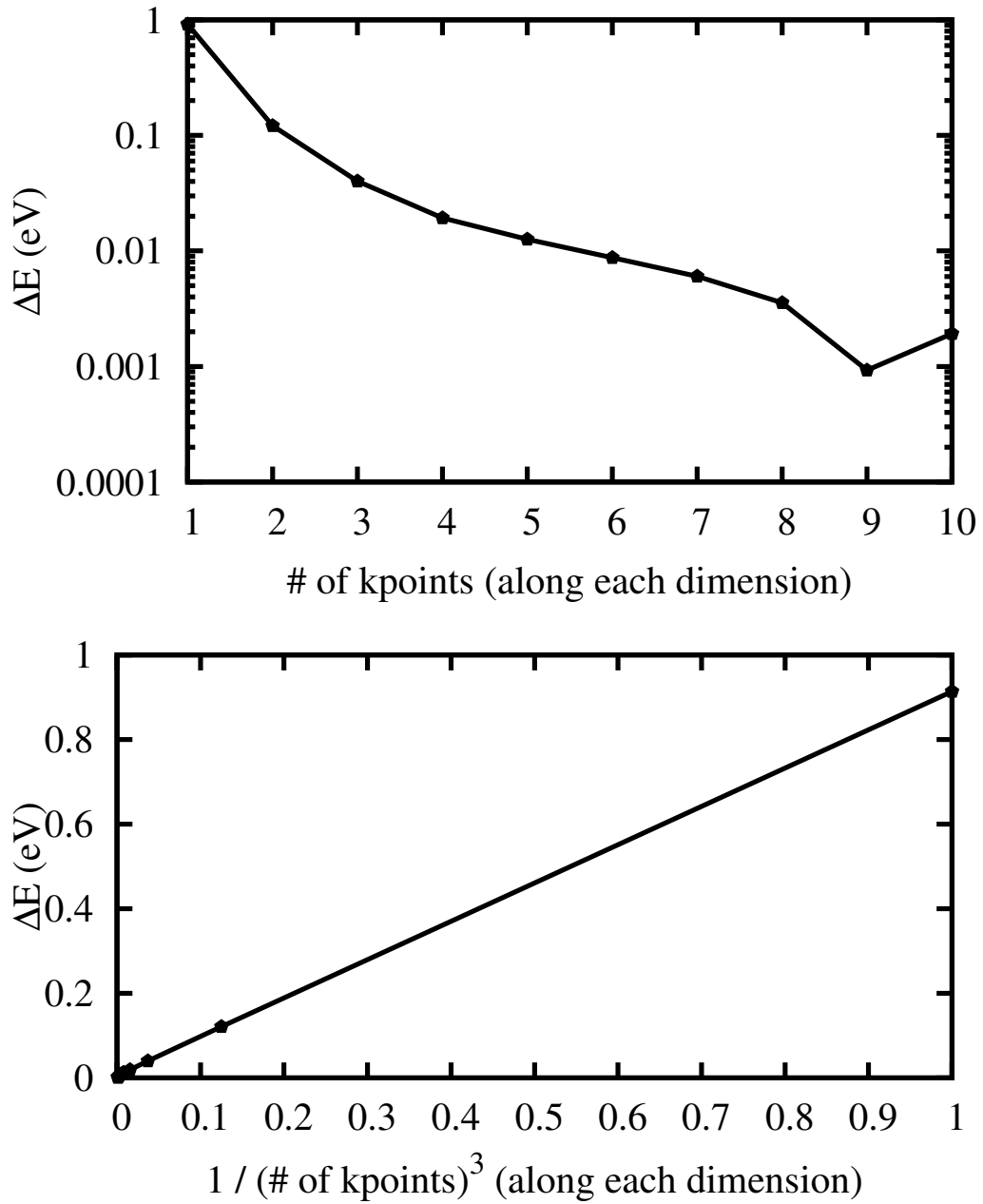


Figure 5.3: Bandgap of Lithium Fluoride calculated using Perdew-Zunger LDA. Difference (ΔE) between the results obtained from the two methods (ground state eigenvalues and NAKKA) is plotted as a function of the number of k-points along each dimension.

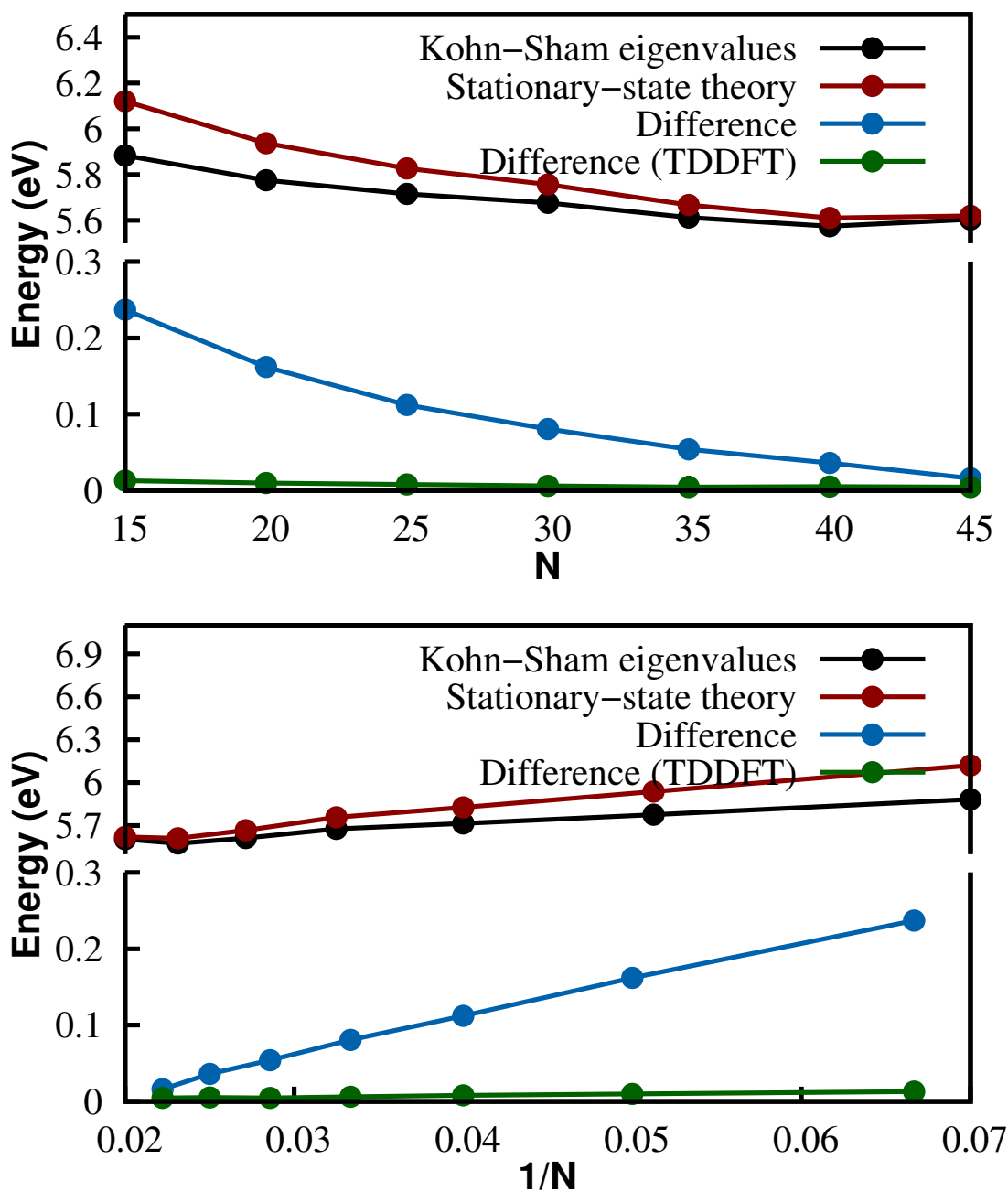


Figure 5.4: HOMO-LUMO gap of straight-chain alkanes of increasing length, calculated using different levels of theory. Lines connecting data points are only to guide eyes. All calculations are done with the PBE exchange-correlation functional. Blue and green data points are obtained by subtracting Kohn-Sham eigenvalue differences from results computed by using more advanced levels of theory. The same data is plotted as a function of the alkane length (N) and the inverse alkane length ($1/N$).

To quantify this behaviour in more detail, we turn to straight-chain alkanes, where we can approach the extended system limit in a systematic manner by varying the length of the chain. Figure 5.4 shows HOMO-LUMO gaps of different alkanes, starting with pentadecane ($N=15$), at intervals (ΔN) of 5, from both NAKEA and TDDFT. As the length of the chain increases, so that the HOMO and LUMO states become more delocalized, the gap energies predicted by both theories converge to gap energies predicted by the bulk Kohn-Sham eigenvalue differences. However, the data also clearly show that that NAKEA approaches the erroneous Kohn-Sham result significantly more slowly than TDDFT does. This clearly establishes that the two methods are not exactly equivalent, and is another indicator of the superiority of the stationary-point approach.

Finally, we note that Chan and Ceder have developed [183] a new technique that allows for efficient and accurate prediction of bandgaps by forcing the electrons to localize, and we believe that an extension of their approach to find better approximations for stationary-point Hohenberg-Kohn theory presents a very promising avenue for future research.

5.4 Issues with multiple-determinant (correlated) states

As one might expect, systems with strong correlations are often handled poorly by a straightforward application of stationary-point Hohenberg-Kohn theory within the non-Aufbau kinetic energy approximation (NAKEA). Even when the ground state may be approximated well with a single Slater determinant, there is no guarantee that the same will hold for the excited state. An example to this is singlet-triplet splitting, in which two electrons occupy two different spa-

tial orbitals and thus can be in a singlet or a triplet spin state, each with very different coulomb repulsion energies.

To illustrate to this phenomenon, we consider singlet and triplet oxygen. The oxygen molecule (O_2) in its ground state is paramagnetic, but also exhibits a singlet state which, due to the forbidden nature of the transition, is meta-stable [211], with an experimental excitation energy of 0.98 eV per molecule [212].

The Kohn-Sham eigenvalue difference between $S_z = 2$ and $S_z = 0$ states within the colinear spin-dependent PBE generalized-gradient approximation greatly overestimates this excitation energy, yielding 2.40 eV, a full 1.42 eV above the experimental value. Stationary-point Hohenberg-Kohn theory within the NAKKA greatly improves the result, reducing the error by nearly a factor of three, yielding a value of 0.43 eV, which is 0.56 eV below the experimental value.

Extraction of the true singlet-triplet splitting within colinear spin-dependent approximations is confounded by the fact that the $S_z = 0$ state actually contains both $S^2 = 0$ (singlet) and $S^2 = 1$ (triplet) contributions ². Fundamentally, this arises because a single determinant is not an eigenfunction of the total spin operator and thus can not distinguish between the singlet and the triplet contributions. The standard solution for this within the Hartree-Fock approximation is to make use of the *spin purification* scheme [186], which assumes that the $S_z = 0$ energy is an average of the singlet and triplet state energies, and then uses the $S_z = 2$ triplet state energy to extract the singlet state energy [186]. Applying this procedure to our results for the oxygen molecule yields the far improved value of 0.86 eV, an error of only 0.12 eV.

² The case of oxygen is even more complicated than described here. Two p-electrons are distributed among *three* p-orbitals, therefore more than one singlet-state exists.

5.5 Open-shell systems: The case of solvated ions

There is considerable interest in the excited states of systems containing transition metal ions as these occur commonly in chemical dyes and electrochemical energy storage systems. This section considers the excited state spectrum of solvated Cu^{2+} ions [213, 214, 215], comparing our theoretical results with uv-vis measurements. Unfortunately, self-consistent iteration for the excited states of these systems can be very unstable, even when using sophisticated schemes[216] for density mixing; because of the presence of degenerate or near-degenerate states near the Fermi level as typically occurs in systems with unpaired electrons, and is quite common for systems with transition metal ions where the d-shell is often partially filled.

Figure 5.5 illustrates the poor convergence of the self-consistent iteration to find the first excited state of Cu^{2+} solvated in water, surrounded by a first solvation shell [213, 214, 215] with the rest of the environment treated implicitly using a nonlinear polarizable continuum model [50]. (The need to include the first solvation shell explicitly in the quantum mechanical calculations arises from the significant hybridization between the orbitals of the copper ion and the orbitals in the neighboring solvent molecules, consistent with the recent observation [217] that including explicit solvent molecules, as opposed to only a continuum solvent, increases the accuracy of excited state calculations.) In this case, an unpaired electron has been excited from a highest occupied molecular orbital (HOMO) to a lowest unoccupied molecular orbital (LUMO). However, there is a degeneracy in the partially-filled d states and this causes the observed very slow convergence (Figure 5.5).

In ground-state calculations of such systems, one would typically address the slow convergence using a Fermi function to smear the fillings; thereby producing a smoother energy landscape and much more rapid converge. However, naive application of such a Fermi-fillings would naturally yield Aufbau-like fillings and only allow for the calculation of the ground state. Accordingly, we have developed an eigenvalue shifting scheme, where prior to calculating the fillings, we add a rigid upward shift to the eigenvalue of the hole state and a rigid downward shift to the eigenvalue of the excited electron state³. Figure 5.5, compares the convergence of this new approach with that of the traditional self-consistent iteration approach and shows how the new approach significantly improves convergence.

To gauge the accuracy of Stationary-point Hohenberg-Kohn theory within NAKEA in these open-shell systems, we performed uv-vis measurements of CuSO₄ in both water and in methanol, and compared the results directly with our own theoretical predictions for the spectral peaks. In methanol, as with water, we include the first shell of solvent molecules in the density-functional calculation; and approximate all solvent beyond the first shell using a continuum solvation model. Figure 5.6 displays these results. As expected, Kohn-Sham eigenvalue differences (with semilocal functionals) underestimate the excitation energies of spectrum peaks (i.e. overestimate the wavelengths). Stationary-point Hohenberg-Kohn theory within NAKEA represents a significant improvement by about a factor of four in the error. However, noticeable differences between theory and experiment still remain, providing motivation for finding new approximations beyond the NAKEA.

Note that when calculating the total energy of the excited state, we here al-

³ The numerical value of this shift in our calculations was 10 Hartrees.

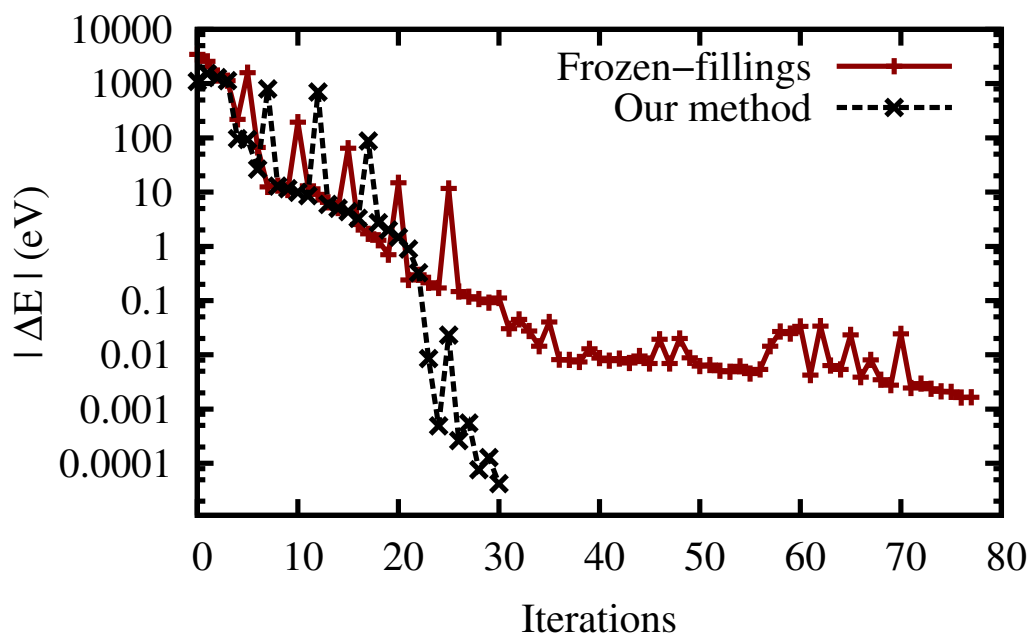


Figure 5.5: Convergence of calculation of the first excited state of Cu^{2+} ion solvated in water, with an explicit first solvation shell: traditional approach in red and the shifted-eigenvalue Fermi function approach in black. Actual data in points, lines are only to guide eyes.

low the state of the surrounding continuum model to relax along with the electronic wavefunctions. However, the time scales in optical excitations are too fast for the orientations of the surrounding fluid molecules to realign. There has been much recent interest and successful attempts [218, 219, 220, 221, 222, 223] to use continuum solvation models together with other excited-state methods (e.g. TDDFT or post-Hartree-Fock) by using a different and/or a frequency-dependent dielectric response function; and we believe that a similar approach may help increase the accuracy of stationary-point Hohenberg-Kohn theory in solvated systems.

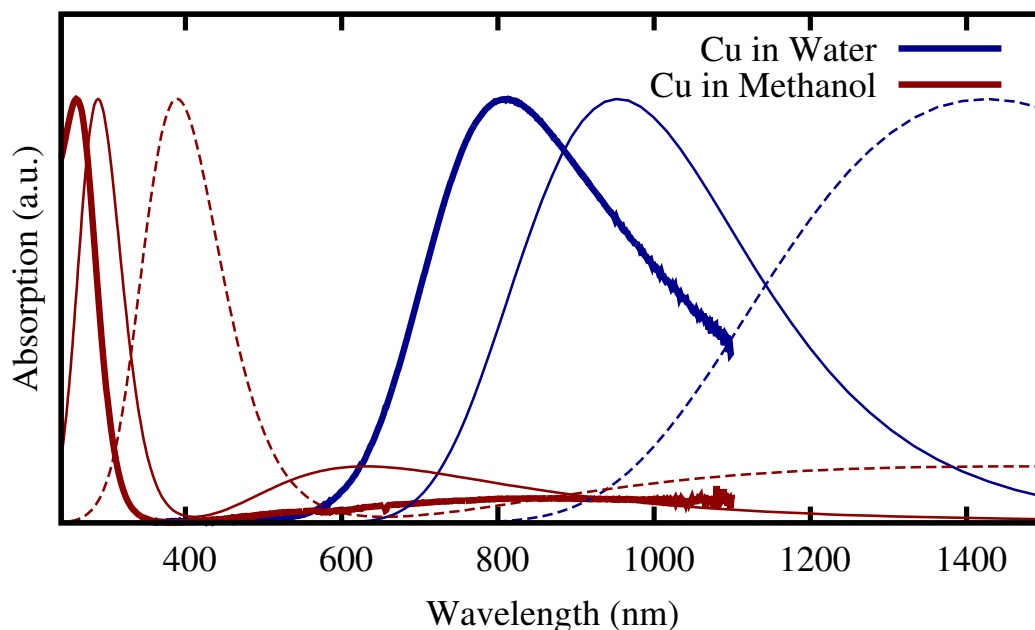


Figure 5.6: Experimental measurements and theoretical predictions for the uv-vis spectrum of CuSO_4 in water and methanol. Kohn-Sham eigenvalue differences (dashed lines), stationary-point Hohenberg-Kohn theory (solid lines) and uv-vis experiment (thick solid lines). Theoretical results include Gaussian broadening of 0.2 eV (water) and 0.4 eV (methanol), determined by best agreement with experiment.

5.6 Applications in lithium battery research ⁴

In this section, we discuss an application of stationary-point Hohenberg-Kohn theory to the study of lithium battery materials and electrolytes [224]. Specifically, Holtz et. al. have developed new electron microscopy techniques for *in-situ* imaging of lithium battery electrodes and electrolytes while the battery is in operation [224]. The EELS (Electron Energy-Loss Spectroscopy) signatures

⁴Part of this work was done in collaboration with Ravishankar Sundararaman and Megan Holtz, and was published in Nano Letters (2014) [224]. We first observed the lack of efficient theoretical tools for excited states during said work [224], which motivated the study that later developed into this chapter.

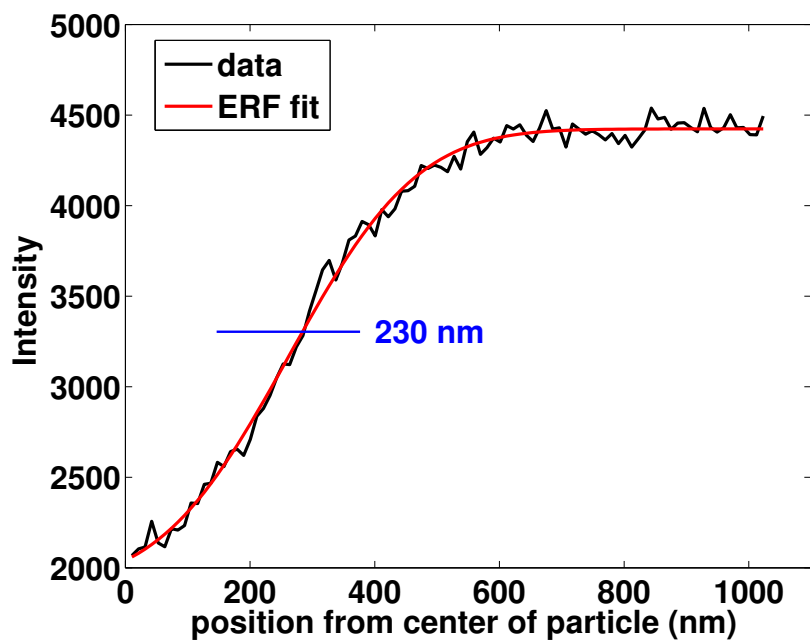


Figure 5.7: The intensity of the 6 eV EELS signal observed by Holtz et. al. [224], measured as a function of the distance from the cathode nanoparticle. Experimental data courtesy of Megan Holtz [224].

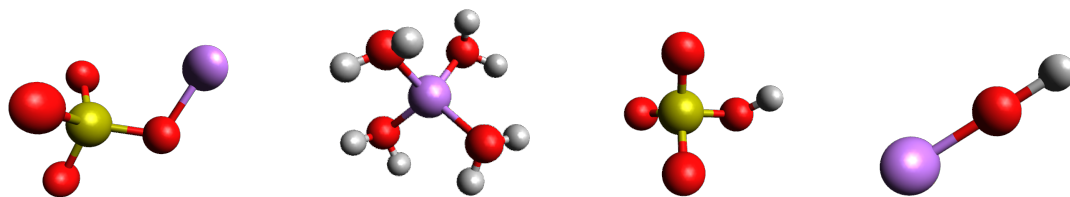


Figure 5.8: A selection of the most probable species involved in experiment by Holtz et. al. From left to right: LiSO_4^- , $\text{Li}[\text{H}_2\text{O}]_4^+$, HSO_4^- and LiOH . Pictures were made using Avogadro [225].

Hydrated Ion	PBE Gap (vacuum)	PBE Gap	HSE06 Gap	STHK Gap	UV-vis peak
LiSO_4^-	2.6	4.6	6.3	5.9	6.2
$\text{Li}[\text{H}_2\text{O}]_4^+$	7.0	6.9	8.9	8.0	-
HSO_4^-	3.2	5.2	7.1	6.2	-
LiOH	3.4	4.2	5.9	5.7	6.1

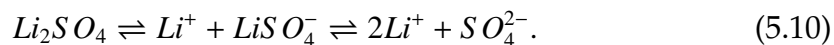
Table 5.2: HOMO-LUMO gaps calculated by different exchange correlation functionals, including stationary-point Hohenberg-Kohn theory (SPHK). All values in electron-volts (eV). Dashes (-) in the UV-vis column indicate values must be above the ~ 7 eV HOMO-LUMO gap of liquid water.

they measure arise from the interaction of valence electrons (in the electrode and/or the electrolyte) with the incoming electron beam. However, positive identification of the species whose signatures they measure requires accurate knowledge of the energy levels and HOMO-LUMO gaps of possible candidate species. Stationary-point Hohenberg-Kohn theory, as described in this chapter, can be extremely useful in this regard.

Holtz et. al. use a battery cell with a $(\text{Li})\text{FePO}_4$ cathode and an aqueous H_2SO_4 electrolyte. When the cathode lithiates, it changes from FePO_4 to LiFePO_4 , suppressing the 5 eV EELS peak caused by FePO_4 . In this way, the authors were able to image the lithiation/delithiation of the cathode. However, in addition to the 5 eV signal originating from within the cathode, the authors also noted another signal, centered at 6 eV, originating from the electrolyte immediately next to the cathode. This signal is absent in water and in H_2SO_4 electrolyte, indicating that it is related to the lithiation/delithiation process. Furthermore, measurement of the spatial dependence of this signal during delithiation reveals an intensity profile consistent with the existence of a concentration gradient in the electrolyte in the immediate neighbourhood of the cathode (Figure 5.7).

From the measured pH and the known equilibrium constants [226], in 0.5 M

Li_2SO_4 (1 M = 1 mol/Liter), there is significantly less than 10^{-6} M LiOH and 10^{-8} M HSO_4^- . Accordingly, we believe the relevant chemical equilibrium near the cathode to be



At equilibrium, we compute the concentrations of the above species as 0.63 M Li^+ , 0.37 M LiSO_4^- and 0.13 M SO_4^{2-} . Based on these experimental details, we suspect that either Li^+ or LiSO_4^- causes the intense spectral feature in the solution in the electron microscopy experiment. However, based on the experimental information alone, we can not positively or uniquely identify the source.

Table 5.2 summarizes HOMO-LUMO gaps for the aforementioned relevant species, as calculated using JDFT, where, as in the previous section, solvated species (and, for small cations, the first solvation shell) are placed inside the nonlinear dielectric continuum described in the second chapter. Based on these results, we conclude that LiSO_4^- , not Li^+ , is responsible for the unexpected anomaly observed in experiment. As the cathode lithiates or delithiates, the concentration of Li^+ near the cathode changes, which locally upsets the chemical equilibrium in equation 5.10, and moves the concentration of the LiSO_4^- away from its value in the bulk. These local changes in the LiSO_4^- concentration near the cathode are then detected in the EELS measurement, allowing Holtz et. al. [224] to indirectly image the lithium go in and out of solution.

To validate our theoretical predictions, we also report in Table 5.2 the locations of the UV-vis peaks of the same species dissolved in water. Note that UV-vis peaks can be identified only for some of the species because, beyond 7 eV, the strong signal coming from H_2O obscures all other features. For species where there is UV-vis data, experiment and theory are in good agreement. (Results

obtained with the PBE functional are only included for comparison purposes, we do not expect those results to give an accurate prediction of the energy gap.)

We believe that these results are significant for a number of reasons. First, they demonstrate the power in lithium battery research of combining *in-situ* experiments with *ab initio* calculations as an interpretive aid. Second, our results show that for these ions in aqueous solvent, stationary-point Hohenberg-Kohn theory with a semilocal functional (PBE) makes a significant improvement over the base Kohn-Sham eigenvalue differences, even performing almost as well as the more expensive HSE06 functional [182, 197] (HSE06, because it includes Fock exchange, scales as $O(N^4)$ while semilocal DFT, including when used with stationary-point Hohenberg-Kohn theory, scales as $O(N^3)$ where N is the number of electrons in the system). Finally our results reinforce our finding from the previous section (5.5) that the electrolyte has a profound effect on the electronic excitation spectrum and that the nonlinear continuum theory we use here (described in detail in chapter 2) is reasonably successful in capturing this effect. For a more through discussion on the issues relating to optical spectra of solvated species, we refer the reader to the previous section.

5.7 Computational Advantages/Disadvantages

A striking feature of stationary-point Hohenberg-Kohn theory is the ease with which it can be implemented into existing electronic structure software, requiring little to no change to the source code. Furthermore, because this approach (particularly with our shifted-eigenvalue Fermi-filling method) uses the same self-consistent methods as the ground state calculations, stationary-point

Hohenberg-Kohn methods can benefit from any advances in numerical methodology that are developed for ground-state calculations. Finally, stationary-point Hohenberg-Kohn theory can be trivially parallelized because the calculation of each individual excited state is independent from all others and requires no interprocess communication. This embarrassing parallelism is very useful, particularly when calculating the entire spectrum of a molecule.

The primary difficulty we have experienced with stationary-point Hohenberg-Kohn theory is stability, particularly as higher states are probed. In ground state calculations, iterative minimization techniques (such as those based on nonlinear conjugate-gradients) offer very stable convergence; however such approaches can not be used directly due to the fact that excited states are not necessarily local minima in energy.

5.8 Computational/Experimental Procedures

We performed all plane-wave DFT calculations with JDFTx [30], an open source implementation of density-functional theory; using a plane-wave basis with a cutoff of 30 Hartrees and a DIIS (direct inversion in iterative subspace [216]) technique to accelerate convergence of self-consistent field equations.

We performed time-dependent DFT calculations with NwChem [23], using a 6-311++G** basis set.

Finally, we obtained optical ultraviolet-visible (UV-VIS) absorption spectra using a HP 8453 diode array spectrometer at room temperature in the denoted solvents, with a conventional 1.0 cm quartz cell.

5.9 Conclusion

We reported a new excited-state electronic-structure technique, stationary-point Hohenberg-Kohn theory; and its practical implementation within a non-Aufbau kinetic energy approximation. The theory has rigorous foundations and the results obtained are very satisfactory for molecular systems, even when using semilocal exchange-correlation functionals. However, the method reduces to Kohn-Sham eigenvalue differences for extended systems, a defect which we hope to correct in future work through the introduction of new excited-state exchange-correlation functionals.

CHAPTER 6

OUTLOOK

This thesis focused on the development and implementation of quantum mechanical solvation models based on joint density-functional theory, with emphasis on non-aqueous solvents used in electrochemical applications. The results discussed in earlier chapters give insights into the power and versatility of joint density-functional theory, and in particular the polarizable continuum approximation. The same, in-principle exact, theoretical framework was used to develop accurate and efficient solvation theories for a wide range of solvents, ranging from organic solvents to room temperature ionic liquids (RTILs).

The second chapter developed a universal framework for generating polarizable continuum approximations for molecular solvents, which was then in the third chapter applied to the infamous lithium dendrite problem. The fourth chapter developed the first joint density-functional description of room temperature ionic liquids, while also contributing to the understanding of the controversial issue of ion pairing in RTILs. The fifth chapter developed the stationary-point Hohenberg-Kohn theory of excited states, which allowed us to study (among others) the optical spectra of solvated ions.

There are many threads from this work that should be pursued in the future. For example, it is worth combining *ab initio* molecular dynamics with joint density-functional theory. While JDFT is exact in principle and allows direct access to thermodynamic averages, it does not allow for direct access to the underlying distributions. This issue came up, for example, during the study of the optical spectra of solvated ions. The theory was able to accurately produce the locations of the spectral peaks, but not the widths of the peaks,

which are most likely determined by fluctuations in the configurations of solvent molecules around the solvated ion. A full *ab initio* molecular dynamics treatment of the system would yield the widths of the peaks as well as their location; however, such a brute force approach would demand enormous computational resources. The optimal choice is a hybrid approach where only a handful of solvent molecules (most likely only those in the first solvation shell) are described explicitly with molecular dynamics while those far away are described with JDFT.

The focus of this thesis was on implicit approximations to JDFT, which, compared to explicit approximations, lead to simpler, faster and more accurate theories that, due to their simpler structure, are more readily generalized to large numbers of solvents. However, this often comes at the expense of empiricism, with the potential danger of overfitting always present. Furthermore, there is also a danger that the resulting empiricism might limit the transferability of the theory to systems wildly different than those to which the theory is fit. One example to this was discussed in the second chapter, where the (highly empirical) effective surface tension approximation fails to adequately distinguish non-polar hydrocarbons from non-polar fluorocarbons.

Therefore, what is desired is a convergence between explicit and implicit approximations, where best elements from each are combined into a hybrid scheme. Already, the nonlinear dielectric theory in Section 2 is a small step in this direction. In nonlinear continuum theory, the computational efficiency of dielectric continuum models was combined with select elements from explicit models (fluid degrees of freedom representing solvent orientations) to construct a more physical model. There is an acute need for something similar in the

non-electrostatic sector (cavitation and dispersion), where, as mentioned above, there is large room for improvement.

JDFT can also strongly benefit from a tighter integration between its flagship implementation (JDFTx [30]) and other atomistic simulation and electronic structure projects (For example, it is already interfaced with the popular Atomistic Simulation Environment (ASE) toolkit, and the Vienna Ab-Initio Simulation Package (VASP)). Such collaborations make available very large classes of numerical algorithms (e.g. projector augmented wave or nudged elastic band) for use with JDFT, and make the ideas in this thesis more relevant by making them available in a format that is familiar and easily accessible to large numbers of researchers.

As demonstrated in Chapter 3, JDFT is a useful tool in high-throughput studies aiming to find better functional materials, especially for energy storage applications where the solvent (electrolyte) plays an important role. This, taken together with the recent development of free (open) databases such as the Materials Project [227], provide the capacity to quickly scan large numbers (potentially thousands) of materials for descriptors of desired properties. This search does not have to be random though. Machine learning algorithms have already made an impact in the electronic-structure community by giving the ability to quickly predict atomization energies [228], and the same algorithms, with descriptors calculated using JDFT, can be utilized to mine databases for novel functional materials.

Magnesium batteries can be an example application area to the above. Divalent metals such as magnesium would make very good rechargeable batteries. However, unlike lithium, stable and efficient electrolytes and cathode materials

suitable for use with Mg have not yet been developed. JDFT can be used to screen large number of potential candidates and aid experimental searches by drastically reducing the size of the parameter space. Coupling big-data mining with theory has been successful in many other areas of science, and this combination has the potential to make a similar impact in physics and materials science, particularly when combined with the advances made here in this thesis.

BIBLIOGRAPHY

- [1] P. A. M. Dirac. Quantum mechanics of many-electron systems. *Proceedings of the Royal Society of London. Series A, Containing Papers of a Mathematical and Physical Character*, 123(792):pp. 714–733, 1929.
- [2] David M Ceperley and BJ Alder. Ground state of the electron gas by a stochastic method. *Physical Review Letters*, 45(7):566, 1980.
- [3] B Tanatar and DM Ceperley. Ground state of the two-dimensional electron gas. *Physical Review B*, 39(8):5005, 1989.
- [4] Walter Kohn and Ann E Mattsson. Edge electron gas. *Physical review letters*, 81(16):3487, 1998.
- [5] Neil R Kestner and Oktay Sinanolu. Study of electron correlation in helium-like systems using an exactly soluble model. *Physical Review*, 128(6):2687, 1962.
- [6] Enrico Fermi. Un metodo statistico per la determinazione di alcune priorietà dell'atome. *Rend. Accad. Naz. Lincei*, 6(602-607):32, 1927.
- [7] Llewellyn H Thomas. The calculation of atomic fields. In *Mathematical Proceedings of the Cambridge Philosophical Society*, volume 23, pages 542–548. Cambridge Univ Press, 1927.
- [8] Pierre Hohenberg and Walter Kohn. Inhomogeneous electron gas. *Physical review*, 136(3B):B864, 1964.
- [9] Mel Levy. Universal variational functionals of electron densities, first-order density matrices, and natural spin-orbitals and solution of the v -representability problem. *Proceedings of the National Academy of Sciences*, 76(12):6062–6065, 1979.
- [10] Yan Alexander Wang and Emily A Carter. Orbital-free kinetic-energy density functional theory. In *Theoretical methods in condensed phase chemistry*, pages 117–184. Springer, 2002.
- [11] Walter Kohn and Lu Jeu Sham. Self-consistent equations including exchange and correlation effects. *Physical Review*, 140(4A):A1133, 1965.

- [12] Axel D. Becke. Densityfunctional thermochemistry. iii. the role of exact exchange. *The Journal of Chemical Physics*, 98(7):5648–5652, 1993.
- [13] Joachim Paier, Martijn Marsman, and Georg Kresse. Why does the b3lyp hybrid functional fail for metals? *The Journal of Chemical Physics*, 127(2):-, 2007.
- [14] J. P. Perdew, K. Burke, and M. Ernzerhof. *Phys. Rev. Lett.*, 77:3865, 1996.
- [15] John P Perdew, Adrienn Ruzsinszky, Gábor I Csonka, Oleg A Vydrov, Gustavo E Scuseria, Lucian A Constantin, Xiaolan Zhou, and Kieron Burke. Restoring the density-gradient expansion for exchange in solids and surfaces. *Physical Review Letters*, 100(13):136406, 2008.
- [16] Jeng-Da Chai and John D Weeks. Orbital-free density functional theory: Kinetic potentials and ab initio local pseudopotentials. *Physical Review B*, 75(20):205122, 2007.
- [17] Youqi Ke, Florian Libisch, Junchao Xia, Lin-Wang Wang, and Emily A Carter. Angular-momentum-dependent orbital-free density functional theory. *Physical review letters*, 111(6):066402, 2013.
- [18] Youqi Ke, Florian Libisch, Junchao Xia, and Emily A Carter. Angular momentum dependent orbital-free density functional theory: Formulation and implementation. *Physical Review B*, 89(15):155112, 2014.
- [19] Arieh Warshel. Multiscale modeling of biological functions: from enzymes to molecular machines (nobel lecture). *Angewandte Chemie International Edition*, 53(38):10020–10031, 2014.
- [20] S. C. L. Kamerlin, M. Haranczyk, and A. Warshel. *J. Phys. Chem. B*, 113:1253, 2009.
- [21] Mats Svensson, Stephane Humbel, Robert DJ Froese, Toshiaki Matsubara, Stefan Sieber, and Keiji Morokuma. Oniom: A multilayered integrated mo+ mm method for geometry optimizations and single point energy predictions. a test for diels-alder reactions and pt (p (t-bu) 3) 2+ h2 oxidative addition. *The Journal of Physical Chemistry*, 100(50):19357–19363, 1996.
- [22] M]ea Frisch, GW Trucks, HB Schlegel, GE Scuseria, MA Robb, JR Cheeseman, G Scalmani, V Barone, B Mennucci, GA Petersson, et al. gaussian 09, gaussian. *Inc., Wallingford, CT*, 4, 2009.

- [23] M. Valiev, E.J. Bylaska, N. Govind, K. Kowalski, T.P. Straatsma, H.J.J. Van Dam, D. Wang, J. Nieplocha, E. Apra, T.L. Windus, and W.A. de Jong. Nwchem: A comprehensive and scalable open-source solution for large scale molecular simulations. *Computer Physics Communications*, 181(9):1477 – 1489, 2010.
- [24] S. A. Petrosyan, A. A. Rigos, and T. A. Arias. *The Journal of Physical Chemistry B*, 109(32):15436–15444, 2005.
- [25] O. Andreussi, I. Dabo, and N. Marzari. *Journal of Chemical Physics*, 136:064102, 2012.
- [26] Deniz Gunceler, Kendra Letchworth-Weaver, Ravishankar Sundararaman, Kathleen A Schwarz, and TA Arias. The importance of nonlinear fluid response in joint density-functional theory studies of battery systems. *Modelling and Simulation in Materials Science and Engineering*, 21(7):074005, 2013.
- [27] Ravishankar Sundararaman and TA Arias. Efficient classical density-functional theories of rigid-molecular fluids and a simplified free energy functional for liquid water. *Computer Physics Communications*, 185(3):818–825, 2014.
- [28] J. Tomasi, B. Mennucci, and R. Cammi. *Chemical Reviews*, 105:2999, 2005.
- [29] Ravishankar Sundararaman and William A Goddard III. The charge-asymmetric nonlocally determined local-electric (candle) solvation model. *The Journal of chemical physics*, 142(6):064107, 2015.
- [30] R. Sundararaman, D. Gunceler, K. Letchworth-Weaver, and T. A. Arias. JDFTx. <http://jdftx.sourceforge.net>, 2012.
- [31] Paolo Giannozzi, Stefano Baroni, Nicola Bonini, Matteo Calandra, Roberto Car, Carlo Cavazzoni, Davide Ceresoli, Guido L Chiarotti, Matteo Cococcioni, Ismaila Dabo, et al. Quantum espresso: a modular and open-source software project for quantum simulations of materials. *Journal of Physics: Condensed Matter*, 21(39):395502, 2009.
- [32] Karlheinz Schwarz and Peter Blaha. Solid state calculations using wien2k. *Computational Materials Science*, 28(2):259–273, 2003.
- [33] Xavier Gonze, B Amadon, P-M Anglade, J-M Beuken, F Bottin,

- P Boulanger, F Bruneval, D Caliste, R Caracas, M Cote, et al. Abinit: First-principles approach to material and nanosystem properties. *Computer Physics Communications*, 180(12):2582–2615, 2009.
- [34] J Enkovaara, Carsten Rostgaard, Jens Jørgen Mortensen, Jingzhe Chen, M Duřak, Lara Ferrighi, Jeppe Gavnholt, Christian Glinsvad, V Haikola, HA Hansen, et al. Electronic structure calculations with gpaw: a real-space implementation of the projector augmented-wave method. *Journal of Physics: Condensed Matter*, 22(25):253202, 2010.
- [35] Jürgen Hafner. Ab-initio simulations of materials using vasp: Density-functional theory and beyond. *Journal of computational chemistry*, 29(13):2044–2078, 2008.
- [36] David J Singh and Lars Nordstrom. *Planewaves, Pseudopotentials, and the LAPW method*. Springer Science & Business Media, 2006.
- [37] Opium - pseudopotential generation project. <http://opium.sourceforge.net/>.
- [38] José M Soler, Emilio Artacho, Julian D Gale, Alberto García, Javier Junquera, Pablo Ordejón, and Daniel Sánchez-Portal. The siesta method for ab initio order-n materials simulation. *Journal of Physics: Condensed Matter*, 14(11):2745, 2002.
- [39] DR Bowler, R Choudhury, MJ Gillan, and T Miyazaki. Recent progress with large-scale ab initio calculations: the conquest code. *arXiv preprint cond-mat/0603063*, 2006.
- [40] Michael J Gillan, David R Bowler, Antonio S Torralba, and Tsuyoshi Miyazaki. Order-n first-principles calculations with the conquest code. *Computer physics communications*, 177(1):14–18, 2007.
- [41] Pablo Ordejón, David A Drabold, Richard M Martin, and Matthew P Grumbach. Linear system-size scaling methods for electronic-structure calculations. *Physical Review B*, 51(3):1456, 1995.
- [42] Kieron Burke. Perspective on density functional theory. *The Journal of Chemical Physics*, 136(15), 2012.
- [43] R. Car and M. Parrinello. *Physical Review Letters*, 55:2471, 1985.

- [44] Jacopo Tomasi and Maurizio Persico. *Chemical Reviews*, 94(7):2027–2094, 1994.
- [45] David J. Giesen, Michael Z. Gu, Christopher J. Cramer, and Donald G. Truhlar. *The Journal of Organic Chemistry*, 61(25):8720–8721, 1996.
- [46] Christopher J. Cramer and Donald G. Truhlar. *Accounts of Chemical Research*, 41(6):760–768, 2008.
- [47] Aleksandr V. Marenich, Christopher J. Cramer, and Donald G. Truhlar. *The Journal of Physical Chemistry B*, 113(18):6378–6396, 2009.
- [48] J.-L. Fattebert and F. Gygi. *International Journal of Quantum Chemistry*, 93:139, 2003.
- [49] K. Letchworth-Weaver and T. A. Arias. *Physical Review B*, 86:075140, 2012.
- [50] Deniz Gunceler, Kendra Letchworth-Weaver, Ravishankar Sundararaman, Kathleen A Schwarz, and T A Arias. *Modelling and Simulation in Materials Science and Engineering*, 21(7):074005, 2013.
- [51] C. Dupont, O. Andreussi, and N. Marzari. *The Journal of Chemical Physics*, 139(21):–, 2013.
- [52] Ravishankar Sundararaman, Deniz Gunceler, and T. A. Arias. *The Journal of Chemical Physics*, 141(13), 2014.
- [53] Iurii Timrov, Oliviero Andreussi, Alessandro Biancardi, Nicola Marzari, and Stefano Baroni. Self-consistent continuum solvation for optical absorption of complex molecular systems in solution. *The Journal of Chemical Physics*, 142(3), 2015.
- [54] Gerbrand Ceder. *MRS Bulletin*, 35:693–701, 2010.
- [55] Veronica M. Sanchez, Mariela Sued, and Damian A. Scherlis. *Journal of Chemical Physics*, 131:174108, 2009.
- [56] Gregory D. Hawkins, Christopher J. Cramer, and Donald G. Truhlar. *The Journal of Physical Chemistry B*, 102(17):3257–3271, 1998.
- [57] David J. Tannor, Bryan Marten, Robert Murphy, Richard A. Friesner,

- Doree Sitkoff, Anthony Nicholls, Murco Ringnalda, William A. Goddard, and Barry Honig. *J. Am. Chem. Soc.*, 116:11875–11882, 1994.
- [58] Bryan Marten, Kyungsun Kim, Christian Cortis, Richard A. Friesner, Robert B. Murphy, Murco N. Ringnalda, Doree Sitkoff, and Barry Honig. *J. Phys. Chem.*, 100:11775–11788, 1996.
- [59] Paulo F. B. Goncalves and Hubert Stassen. *Pure Appl. Chem.*, 76:231240, 2004.
- [60] Ming Wah Wong, Kenneth B. Wiberg, and Michael J. Frisch. *Journal of Computational Chemistry*, 16(3):385–394, 1995.
- [61] H. J. C. Berendsen, J. R. Grigera, and T. P. Straatsma. *J. Phys. Chem.*, 91:6269–6271, 1987.
- [62] B. Mennucci, J. Tomasi, R. Cammi, J. R. Cheeseman, M. J. Frisch, F. J. Devlin, S. Gabriel, and P. J. Stephens. *The Journal of Physical Chemistry A*, 106(25):6102–6113, 2002.
- [63] Herbert Federer. *Trans. Amer. Math. Soc.*, 93:418–491, 1958.
- [64] James A Sethian. Theory, algorithms, and applications of level set methods for propagating interfaces. *Acta numerica*, 5:309–395, 1996.
- [65] Stefan Grimme. *Journal of Computational Chemistry*, 27(15):1787, 2006.
- [66] R. C. Reid, J. M. Prausnitz, and B. E. Poling. *The Properties of Gases and Liquids, Fourth Edition*. McGraw-Hill, 1987.
- [67] R. C. Weast, editor. *Handbook of Chemistry and Physics (53rd Edition)*. Chemical Rubber Co, 1972.
- [68] Paul Winget, Gregory D. Hawkins, Christopher J. Cramer, and Donald G. Truhlar. *Journal of Physical Chemistry B*, 104(19):4726–4734, 2000.
- [69] James B. Foresman, Todd A. Keith, Kenneth B. Wiberg, John Snoonian, and Michael J. Frisch. *The Journal of Physical Chemistry*, 100(40):16098–16104, 1996.
- [70] Ravishankar Sundararaman and William A. Goddard III. The

charge-asymmetric nonlocally-determined local-electric (candle) solvation model. *arXiv:1410.2922*.

- [71] Mukul D Tikekar, Lynden A Archer, and Donald L Koch. Stability analysis of electrodeposition across a structured electrolyte with immobilized anions. *Journal of The Electrochemical Society*, 161(6):A847–A855, 2014.
- [72] J. P. Perdew, A. Ruzsinszky, G. I. Csonka, L. A. Constantin, and J. Sun. *Physical Review Letters*, 103:026403, 2009.
- [73] *NIST Computational Chemistry Comparison and Benchmark Database*. <http://cccbdb.nist.gov/>.
- [74] L.A. Archer, T. Arias, Y. Lu, Z. TU, D. Gunceler, and S. Choudhury. Dendrite inhibiting electrolytes for metal-based batteries, October 1 2015. WO Patent App. PCT/US2015/022,157.
- [75] Anubhav Jain, Shyue Ping Ong, Geoffroy Hautier, Wei Chen, William Davidson Richards, Stephen Dacek, Shreyas Cholia, Dan Gunter, David Skinner, Gerbrand Ceder, and Kristin a. Persson. The Materials Project: A materials genome approach to accelerating materials innovation. *APL Materials*, 1(1):011002, 2013.
- [76] Deniz Gunceler, Kathleen A Schwarz, Ravishankar Sundararaman, Kendra Letchworth-Weaver, and T A Arias. Nonlinear solvation models: Dendrite suppression on lithium surfaces. In *16th International Workshop on Computation Physics and Materials Science: Total Energy and Force Methods*, 2013.
- [77] Deniz Gunceler, Kendra Letchworth-Weaver, Ravishankar Sundararaman, Kathleen A Schwarz, and T A Arias. The importance of nonlinear fluid response in joint density-functional theory studies of battery systems. *Modelling and Simulation in Materials Science and Engineering*, 21(7):074005, 2013.
- [78] Markus Jäckle and Axel Groß. Microscopic properties of lithium, sodium, and magnesium battery anode materials related to possible dendrite growth. *The Journal of Chemical Physics*, 141(17), 2014.
- [79] Kristin Persson, Vijay A. Sethuraman, Laurence J. Hardwick, Yoyo Hinuma, Ying Shirley Meng, Anton van der Ven, Venkat Srinivasan, Robert Kostecki, and Gerbrand Ceder. *J. Phys. Chem. Lett*, 1:11761180, 2010.

- [80] Kristin Persson, Yoyo Hinuma, Ying Shirley Meng, Anton Van der Ven, and Gerbrand Ceder. *Phys. Rev. B*, 82(125416), 2010.
- [81] Sascha Thinius, Mazharul M. Islam, Paul Heitjans, and Thomas Bredow. *J. Phys. Chem. C*, 118(22732280), 2014.
- [82] Ken Tasaki. *J. Phys. Chem. C*, 118(14431450), 2014.
- [83] P. Ganesh, Jeongnim Kim, Changwon Park, Mina Yoon, Fernando A. Reboredo, and Paul R. C. Kent. *J. Chem. Theory Comput.*, 10(53185323), 2014.
- [84] Siqi Shi, Peng Lu, Zhongyi Liu, Yue Qi, Louis G. Hector Jr., Hong Li, and Stephen J. Harris. *Journal of American Chemical Society*, 134:1547615487, 2012.
- [85] Siqi Shi, Peng Lu, Zhongyi Liu, Yue Qi, Louis G. Hector Jr., Hong Li, and Stephen J. Harris. *Journal of Physical Chemistry C*, 114:2090320906, 2010.
- [86] Siqi Shi, Yue Qi, Hong Li, and Louis G. Hector Jr. *Journal of Physical Chemistry C*, 117:85798593, 2013.
- [87] Motoaki Nishijima, Takuya Ootani, Yuichi Kamimura, Toshitsugu Sueki, Shogo Esaki, Shunsuke Murai, Koji Fujita, Katsuhisa Tanaka, Koji Ohira, Yukinori Koyama, et al. Accelerated discovery of cathode materials with prolonged cycle life for lithium-ion battery. *Nature communications*, 5, 2014.
- [88] Gerbrand Ceder, Geoffroy Hautier, Anubhav Jain, and Shyue Ping Ong. Recharging lithium battery research with first-principles methods. *Mrs Bulletin*, 36(03):185–191, 2011.
- [89] Shyue Ping Ong, Vincent L Chevrier, Geoffroy Hautier, Anubhav Jain, Charles Moore, Sangtae Kim, Xiaohua Ma, and Gerbrand Ceder. Voltage, stability and diffusion barrier differences between sodium-ion and lithium-ion intercalation materials. *Energy & Environmental Science*, 4(9):3680–3688, 2011.
- [90] Kisuk Kang, Ying Shirley Meng, Julien Bréger, Clare P Grey, and Gerbrand Ceder. Electrodes with high power and high capacity for rechargeable lithium batteries. *Science*, 311(5763):977–980, 2006.

- [91] Kevin Leung and Joanne L. Budzien. Ab initio molecular dynamics simulations of the initial stages of solid-electrolyte interphase formation on lithium ion battery graphitic anodes. *Phys. Chem. Chem. Phys.*, 12:6583–6586, 2010.
- [92] Khang Hoang. *Phys. Rev. Applied*, 3:024013, Feb 2015.
- [93] Guangyuan Zheng, Seok Woo Lee, Zheng Liang, Hyun-Wook Lee, Kai Yan, Hongbin Yao, Haotian Wang, Weiyang Li, Steven Chu, and Yi Cui. Interconnected hollow carbon nanospheres for stable lithium metal anodes. *Nature Nanotechnology*, 9:618623, 2014.
- [94] Min Sik Park, Sang Bok Ma, Dong Joon Lee, Dongmin Im, Seok-Gwang Doo, and Osamu Yamamoto. *Scientific Reports*, 4(3815), 2014.
- [95] John B. Goodenough. Rechargeable batteries: challenges old and new. *Journal of Solid State Electrochemistry*, 16(6):2019–2029, 2012.
- [96] Kei Nishikawa, Takeshi Mori, Tetsuo Nishida, Yasuhiro Fukunaka, Michel Rossoa, and Takayuki Homma. *J. Electrochem. Soc.*, 157(11), 2010.
- [97] E. Peled. *Journal of the Electrochemical Society*, 126:2047–2051, 1979.
- [98] Soshi Shiraishi, Kiyoshi Kanamura, and Zenichiro Takehara. *J. Appl. Electrochem.*, 29:869–881, 1999.
- [99] Nicolas Dupre, Marine Cuisinier, and Dominique Guyomard. *The Electrochemical Society Interface*, pages 61–69, 2011.
- [100] J. N. Chazalvier. *Physical Review A*, 42(12), 1990.
- [101] Mukul D. Tikekar, Lynden A. Archer, and Donald L. Koch. *J. Electrochem. Soc.*, 161(6), 2014.
- [102] Matthew B. Pinsona and Martin Z. Bazant. *Journal of The Electrochemical Society*, 160(2):A243–A250, 2013.
- [103] Matthew Z. Mayers, Jakub W. Kaminski, and Thomas F. Miller. *The Journal of Physical Chemistry C*, 116(50):26214–26221, 2012.
- [104] Yaron S. Cohen, Yair Cohen, and Doron Aurbach. Micromorphological studies of lithium electrodes in alkyl carbonate solutions using

- in situ atomic force microscopy. *The Journal of Physical Chemistry B*, 104(51):12282–12291, 2000.
- [105] Venkatasailanathan Ramadesigana, Paul W. C. Northrop, Sumitava Dea, Shriram Santhanagopalanb, Richard D. Braatzc, and Venkat R. Subramania. *J. Electrochem. Soc.*, 159(3):R31–R45, 2012.
- [106] Katherine J. Harry, Daniel T. Hallinan, Dilworth Y. Parkinson, Alastair A. MacDowell, and Nitash P. Balsara. *Nature Materials*, 13:6973, 2014.
- [107] Yingying Lu, Zhengyuan Tu, and Lynden A. Archer. Stable lithium electrodeposition in liquid and nanoporous solid electrolytes. *Nature Materials*, 13:961969, 2014.
- [108] P. Ganesh, P. R. C. Kent, and De en Jiang. *Journal of Physical Chemistry C*, 116:24476–24481, 2012.
- [109] Yingying Lu, Shaomao Xu, Jonathan Shu, Wajdi Issam A. Aladat, and Lynden A. Archer. High voltage {LIB} cathodes enabled by salt-reinforced liquid electrolytes. *Electrochemistry Communications*, 51(0):23 – 26, 2015.
- [110] Yingying Lu, Zhengyuan Tu, Jonathan Shu, and Lynden A. Archer. Stable lithium electrodeposition in salt-reinforced electrolytes. *Journal of Power Sources*, 279(0):413 – 418, 2015. 9th International Conference on Lead-Acid Batteries {LABAT} 2014.
- [111] Kiyoshi Kanamura, Soshi Shiraishi, and Zenichiro Takehara. *Journal of the Electrochemical Society*, 143(7):2187–2197, 1996.
- [112] Ryo Mogi, Minoru Inaba, Soon-Ki Jeong, Yasutoshi Iriyama, Takeshi Abe, and Zempachi Ogumi. *Journal of The Electrochemical Society*, 149(12):A1578–A1583, 2002.
- [113] Shinichi Komaba, Toru Ishikawa, Naoaki Yabuuchi, Wataru Murata, Atsushi Ito, and Yasuhiko Ohsawa. *Applied Materials & Interfaces*, 3:41654168, 2011.
- [114] Perla B Balbuena and Yixuan Wang. *Lithium-ion batteries: solid-electrolyte interphase*. Imperial college press London, 2004.
- [115] Kang Xu. Nonaqueous liquid electrolytes for lithium-based rechargeable batteries. *Chemical Reviews*, 104(10):4303–4418, 2004.

- [116] Doron Aurbach, Yair Ein-Eli, Orit Chusid, Yaakov Carmeli, Matsliach Babai, and Herzl Yamin. The correlation between the surface chemistry and the performance of li-carbon intercalation anodes for rechargeable rocking-chairtype batteries. *Journal of The Electrochemical Society*, 141(3):603–611, 1994.
- [117] T. A. Arias, M. C. Payne, and J. D. Joannopoulos. *Phys. Rev. Lett*, 69(7):1077, 1992.
- [118] David Vanderbilt. Soft self-consistent pseudopotentials in a generalized eigenvalue formalism. *Phys. Rev. B*, 41:7892–7895, Apr 1990.
- [119] Kevin F. Garrity, Joseph W. Bennett, Karin M. Rabe, and David Vanderbilt. Pseudopotentials for high-throughput dft calculations. *Computational Materials Science*, 81(0):446 – 452, 2014.
- [120] <http://www.physics.rutgers.edu/~dhv/uspp/>.
- [121] K. Momma and F. Izumi. *J. Appl. Crystallogr.*, 44:12721276, 2011.
- [122] Ravishankar Sundararaman and T. A. Arias. *Phys. Rev. B*, 87:165122, 2013.
- [123] Sebastian Schnur and Axel Groß. Challenges in the first-principles description of reactions in electrocatalysis. *Catalysis Today*, 165(1):129 – 137, 2011.
- [124] Deniz Gunceler and TA Arias. Universal iso-density polarizable continuum model for molecular solvents.
- [125] Vernica M. Snchez, Mariela Sued, and Damin A. Scherlis. First-principles molecular dynamics simulations at solid-liquid interfaces with a continuum solvent. *The Journal of Chemical Physics*, 131(17), 2009.
- [126] Owen Crowther, , and Alan C. West. *Journal of The Electrochemical Society*, 155(11):A806–A811, 2008.
- [127] R. Edwin Garcia Aniruddha Jana, David R. Ely. *Journal of Power Sources*, 275:912–921, 2015.
- [128] Hermann Weingärtner. Understanding ionic liquids at the molecular level: facts, problems, and controversies. *Angewandte Chemie International Edition*, 47(4):654–670, 2008.

- [129] Robert Hayes, Gregory G Warr, and Rob Atkin. Structure and nanostructure in ionic liquids. *Chemical reviews*, 115(13):6357–6426, 2015.
- [130] Natalia V Plechkova and Kenneth R Seddon. Applications of ionic liquids in the chemical industry. *Chemical Society Reviews*, 37(1):123–150, 2008.
- [131] Michel Armand, Frank Endres, Douglas R MacFarlane, Hiroyuki Ohno, and Bruno Scrosati. Ionic-liquid materials for the electrochemical challenges of the future. *Nature materials*, 8(8):621–629, 2009.
- [132] Debbie S Silvester and Richard G Compton. Electrochemistry in room temperature ionic liquids: A review and some possible applications. *Zeitschrift für Physikalische Chemie*, 220(10):1247–1274, 2006.
- [133] Alexei A Kornyshev. Double-layer in ionic liquids: paradigm change? *The Journal of Physical Chemistry B*, 111(20):5545–5557, 2007.
- [134] Martin Z Bazant, Brian D Storey, and Alexei A Kornyshev. Double layer in ionic liquids: Overscreening versus crowding. *Physical Review Letters*, 106(4):046102, 2011.
- [135] Hiroyuki Tokuda, Seiji Tsuzuki, Md Abu Bin Hasan Susan, Kikuko Hayamizu, and Masayoshi Watanabe. How ionic are room-temperature ionic liquids? an indicator of the physicochemical properties. *The Journal of Physical Chemistry B*, 110(39):19593–19600, 2006.
- [136] Thorsten Köddermann, Christiane Wertz, Andreas Heintz, and Ralf Ludwig. Ion-pair formation in the ionic liquid 1-ethyl-3-methylimidazolium bis (triflyl) imide as a function of temperature and concentration. *ChemPhysChem*, 7(9):1944–1949, 2006.
- [137] Matthew A Gebbie, Markus Valtiner, Xavier Banquy, Eric T Fox, Wesley A Henderson, and Jacob N Israelachvili. Ionic liquids behave as dilute electrolyte solutions. *Proceedings of the National Academy of Sciences*, 110(24):9674–9679, 2013.
- [138] Matthew A Gebbie, Markus Valtiner, Xavier Banquy, Wesley A Henderson, and Jacob N Israelachvili. Reply to perkin et al.: Experimental observations demonstrate that ionic liquids form both bound (stern) and diffuse electric double layers. *Proc. Natl. Acad. Sci. USA*, 110:E4122, 2013.
- [139] Matthew A Gebbie, Howard A Dobbs, Markus Valtiner, and Jacob N Is-

- raelachvili. Long-range electrostatic screening in ionic liquids. *Proceedings of the National Academy of Sciences*, 112:7432–7437, 2015.
- [140] Alpha A Lee, Dominic Vella, Susan Perkin, and Alain Goriely. Are room-temperature ionic liquids dilute electrolytes? *The Journal of Physical Chemistry Letters*, 6(1):159–163, 2014.
- [141] Ekaterina I. Izgorodina, Uditha L. Bernard, and Douglas R. MacFarlane. Ion-pair binding energies of ionic liquids: Can dft compete with ab initio-based methods? *The Journal of Physical Chemistry A*, 113(25):7064–7072, 2009.
- [142] Patricia A Hunt, Ian R Gould, and Barbara Kirchner. The structure of imidazolium-based ionic liquids: Insights from ion-pair interactions. *Australian journal of chemistry*, 60(1):9–14, 2007.
- [143] Susan Perkin, Mathieu Salanne, Paul Madden, and Ruth Lynden-Bell. Is a stern and diffuse layer model appropriate to ionic liquids at surfaces? *Proceedings of the National Academy of Sciences*, 110(44):E4121–E4121, 2013.
- [144] Grigory Zarubin and Markus Bier. Static dielectric properties of dense ionic fluids. *The Journal of chemical physics*, 142(18):184502, 2015.
- [145] Mario G Del Pópolo, Ruth M Lynden-Bell, and Jorge Kohanoff. Ab initio molecular dynamics simulation of a room temperature ionic liquid. *The Journal of Physical Chemistry B*, 109(12):5895–5902, 2005.
- [146] Zhigang Lei, Chengna Dai, and Biaohua Chen. Gas solubility in ionic liquids. *Chemical reviews*, 114(2):1289–1326, 2013.
- [147] Stefan Zahn and Barbara Kirchner. Validation of dispersion-corrected density functional theory approaches for ionic liquid systems. *The Journal of Physical Chemistry A*, 112(36):8430–8435, 2008.
- [148] Stefan Grimme Waldemar Hujo and Barbara Kirchner. Performance of dispersion-corrected density functional theory for the interactions in ionic liquids. *Physical Chemistry Chemical Physics*, pages 4875–4883, 2012.
- [149] Barbara Kirchner. Ionic liquids from theoretical investigations. In *Ionic liquids*, pages 213–262. Springer, 2010.

- [150] Oldamur Hollóczy, Friedrich Malberg, Tom Welton, and Barbara Kirchner. On the origin of ionicity in ionic liquids. ion pairing versus charge transfer. *Physical Chemistry Chemical Physics*, 16(32):16880–16890, 2014.
- [151] Christian Schröder. Comparing reduced partial charge models with polarizable simulations of ionic liquids. *Physical Chemistry Chemical Physics*, 14(9):3089–3102, 2012.
- [152] Yong Zhang and Edward J Maginn. A simple aimd approach to derive atomic charges for condensed phase simulation of ionic liquids. *The Journal of Physical Chemistry B*, 116(33):10036–10048, 2012.
- [153] Zongzhi Hu, Jenel Vatamanu, Oleg Borodin, and Dmitry Bedrov. A molecular dynamics simulation study of the electric double layer and capacitance of [bmim][pf 6] and [bmim][bf 4] room temperature ionic liquids near charged surfaces. *Physical Chemistry Chemical Physics*, 15(34):14234–14247, 2013.
- [154] Jan Forsman, Clifford E Woodward, and Martin Trulsson. A classical density functional theory of ionic liquids. *The Journal of Physical Chemistry B*, 115(16):4606–4612, 2011.
- [155] Martin Turesson, Ryan Szparaga, Ke Ma, Clifford E Woodward, and Jan Forsman. Classical density functional theory & simulations on a coarse-grained model of aromatic ionic liquids. *Soft matter*, 10(18):3229–3237, 2014.
- [156] Varinia S Bernales, Aleksandr V Marenich, Renato Contreras, Christopher J Cramer, and Donald G Truhlar. Quantum mechanical continuum solvation models for ionic liquids. *The Journal of Physical Chemistry B*, 116(30):9122–9129, 2012.
- [157] Till Cremer, Claudia Kolbeck, Kevin RJ Lovelock, Natalia Paape, René Wölfel, Peter S Schulz, Peter Wasserscheid, Henry Weber, Jens Thar, Barbara Kirchner, et al. Towards a molecular understanding of cation–anion interactions probing the electronic structure of imidazolium ionic liquids by nmr spectroscopy, x-ray photoelectron spectroscopy and theoretical calculations. *Chemistry-A European Journal*, 16(30):9018–9033, 2010.
- [158] Vera Lockett, Mike Horne, Rossen Sedev, Theo Rodopoulos, and John Ralston. Differential capacitance of the double layer at the electrode/ionic liquids interface. *Physical Chemistry Chemical Physics*, 12(39):12499–12512, 2010.

- [159] Bo Li, Pei Liu, Zhenli Xu, and Shenggao Zhou. Ionic size effects: generalized boltzmann distributions, counterion stratification and modified debye length. *Nonlinearity*, 26(10):2899, 2013.
- [160] Roland Roth. Fundamental measure theory for hard-sphere mixtures: a review. *Journal of Physics: Condensed Matter*, 22(6):063102, 2010.
- [161] Bo Li. *SIAM Journal on Mathematical Analysis*, 40(6):2536–2566, 2009.
- [162] Vojko Vlachy. *Annual Review of Physical Chemistry*, 50:145–165, 1999.
- [163] Michael H Abraham and William E Acree Jr. Comparative analysis of solvation and selectivity in room temperature ionic liquids using the abraham linear free energy relationship. *Green Chemistry*, 8(10):906–915, 2006.
- [164] William E Acree Jr and Michael H Abraham. The analysis of solvation in ionic liquids and organic solvents using the abraham linear free energy relationship. *Journal of Chemical Technology and Biotechnology*, 81(8):1441–1446, 2006.
- [165] Fabrice Mutelet, Virginia Ortega-Villa, Jean-Charles Moïse, Jean-Noël Jaubert, and William E Acree Jr. Prediction of partition coefficients of organic compounds in ionic liquids using a temperature-dependent linear solvation energy relationship with parameters calculated through a group contribution method. *Journal of Chemical & Engineering Data*, 56(9):3598–3606, 2011.
- [166] Salwa K Poole and Colin F Poole. Experimental protocol for the assessment of solvent strength and selectivity of liquid phases used in gas chromatography. *Journal of Chromatography A*, 500:329–348, 1990.
- [167] Michael H Abraham, Gary S Whiting, Ruth M Doherty, and Wendel J Shuely. Hydrogen bonding: Xvii. the characterisation of 24 gas-liquid chromatographic stationary phases studied by poole and co-workers. including molten salts, and evaluation of solute-stationary phase interactions. *Journal of Chromatography A*, 587(2):229–236, 1991.
- [168] Fernando Silva, Cristiana Gomes, Marta Figueiredo, Renata Costa, Ana Martins, and Carlos M Pereira. The electrical double layer at the [bmim][pf6] ionic liquid/electrode interface—effect of temperature on the differential capacitance. *Journal of Electroanalytical Chemistry*, 622(2):153–160, 2008.

- [169] N Borisenko, Sh Zein El Abedin, and F Endres. In situ stm investigation of gold reconstruction and of silicon electrodeposition on au (111) in the room temperature ionic liquid 1-butyl-1-methylpyrrolidinium bis (trifluoromethylsulfonyl) imide. *The Journal of Physical Chemistry B*, 110(12):6250–6256, 2006.
- [170] Marcel Druschler, Natalia Borisenko, Jens Wallauer, Christian Winter, Benedikt Huber, Frank Endres, and Bernhard Roling. New insights into the interface between a single-crystalline metal electrode and an extremely pure ionic liquid: slow interfacial processes and the influence of temperature on interfacial dynamics. *Physical Chemistry Chemical Physics*, 14(15):5090–5099, 2012.
- [171] Jacob Israelachvili, Younjin Min, Mustafa Akbulut, Anna Alig, Gregory Carver, Wren Greene, Kai Kristiansen, Emily Meyer, Noshir Pesika, Kenneth Rosenberg, et al. Recent advances in the surface forces apparatus (sfa) technique. *Reports on Progress in Physics*, 73(3):036601, 2010.
- [172] Andreas Klamt and GCOSMO Schüürmann. Cosmo: a new approach to dielectric screening in solvents with explicit expressions for the screening energy and its gradient. *Journal of the Chemical Society, Perkin Transactions 2*, (5):799–805, 1993.
- [173] R Sundararaman, D Gunceler, K Letchworth-Weaver, and TA Arias. Jdftx, 2012.
- [174] John P Perdew, Kieron Burke, and Matthias Ernzerhof. Generalized gradient approximation made simple. *Physical review letters*, 77(18):3865, 1996.
- [175] Deniz Gunceler and TA Arias. Universal iso-density polarizable continuum model for molecular solvents. *arXiv preprint arXiv:1403.6465*, 2014.
- [176] P. Hohenberg and W. Kohn. Inhomogeneous electron gas. *Phys. Rev.*, 136:B864–B871, Nov 1964.
- [177] W. Kohn and L. J. Sham. Self-consistent equations including exchange and correlation effects. *Phys. Rev.*, 140:A1133–A1138, Nov 1965.
- [178] John P. Perdew. Density functional theory and the band gap problem. *International Journal of Quantum Chemistry*, 28(S19):497–523, 1985.

- [179] F Aryasetiawan and O Gunnarsson. The gw method. *Reports on Progress in Physics*, 61(3):237, 1998.
- [180] Dario Rocca, Ralph Gebauer, Yousef Saad, and Stefano Baroni. Turbo charging time-dependent density-functional theory with lanczos chains. *The Journal of Chemical Physics*, 128(15), 2008.
- [181] Matthias Ernzerhof and Gustavo E. Scuseria. Assessment of the perdew-burkeernzerhof exchange-correlation functional. *The Journal of Chemical Physics*, 110(11):5029–5036, 1999.
- [182] Jochen Heyd, Gustavo E. Scuseria, and Matthias Ernzerhof. Hybrid functionals based on a screened coulomb potential. *The Journal of Chemical Physics*, 118(18):8207–8215, 2003.
- [183] M. K. Y. Chan and G. Ceder. Efficient band gap prediction for solids. *Phys. Rev. Lett.*, 105:196403, Nov 2010.
- [184] Jonathan H. Skone, Marco Govoni, and Giulia Galli. Self-consistent hybrid functional for condensed systems. *Phys. Rev. B*, 89:195112, May 2014.
- [185] Adle D. Laurent and Denis Jacquemin. Td-dft benchmarks: A review. *International Journal of Quantum Chemistry*, 113(17):2019–2039, 2013.
- [186] Tim Kowalczyk, Shane R. Yost, and Troy Van Voorhis. Assessment of the scf density functional theory approach for electronic excitations in organic dyes. *The Journal of Chemical Physics*, 134(5):–, 2011.
- [187] Jeppe Gavnholt, Thomas Olsen, Mads Engelund, and Jakob Schiøtz. *Phys. Rev. B*, 78:075441, Aug 2008.
- [188] R. O. Jones and O. Gunnarsson. *Rev. Mod. Phys.*, 61:689–746, Jul 1989.
- [189] Tom Ziegler, Arvi Rauk, and Evert J. Baerends. On the calculation of multiplet energies by the hartree-fock-slater method. *Theoretica chimica acta*, 43(3):261–271, 1977.
- [190] Nicolas Onofrio and Jean-Marie Mouesca. Analysis of the singlet-triplet splitting computed by the density functional theory broken-symmetry method: Is it an exchange coupling constant? *Inorganic Chemistry*, 50(12):5577–5586, 2011.

- [191] Andrew T. B. Gilbert, Nicholas A. Besley, and Peter M. W. Gill. Self-consistent field calculations of excited states using the maximum overlap method (mom). *The Journal of Physical Chemistry A*, 112(50):13164–13171, 2008.
- [192] David Prendergast and Giulia Galli. X-ray absorption spectra of water from first principles calculations. *Phys. Rev. Lett.*, 96:215502, May 2006.
- [193] Shang-Di Mo and W. Y. Ching. μ - β calculation of the core-hole effect in the electron energy-loss near-edge structure. *Phys. Rev. B*, 62:7901–7907, Sep 2000.
- [194] Emilio Artacho, M. Rohlfing, M. Côté, P. D. Haynes, R. J. Needs, and C. Molteni. Structural relaxations in electronically excited poly(*para*-phenylene). *Phys. Rev. Lett.*, 93:116401, Sep 2004.
- [195] Manoj K. Harbola. Exchange-correlation potentials in ground- and excited-state kohn-sham theory. *Phys. Rev. A*, 69:042512, Apr 2004.
- [196] John P. Perdew and Mel Levy. Extrema of the density functional for the energy: Excited states from the ground-state theory. *Phys. Rev. B*, 31:6264–6272, May 1985.
- [197] Jochen Heyd, Gustavo E Scuseria, and Matthias Ernzerhof. Erratum: hybrid functionals based on a screened coulomb potential[j. chem. phys. 118, 8207 (2003)]. *The Journal of Chemical Physics*, 124(21):219906, 2006.
- [198] M Marsman, J Paier, A Stroppa, and G Kresse. Hybrid functionals applied to extended systems. *Journal of Physics: Condensed Matter*, 20(6):064201, 2008.
- [199] P. H. Hahn, W. G. Schmidt, and F. Bechstedt. Molecular electronic excitations calculated from a solid-state approach: Methodology and numerics. *Phys. Rev. B*, 72:245425, Dec 2005.
- [200] Christoph Friedrich, Mathias C. Müller, and Stefan Blügel. Band convergence and linearization error correction of all-electron calculations: The extreme case of zinc oxide. *Phys. Rev. B*, 83:081101, Feb 2011.
- [201] Osman Barış Malcıoğlu, Ralph Gebauer, Dario Rocca, and Stefano Baroni. turbodft—a code for the simulation of molecular spectra using the

- liouville–lanczos approach to time-dependent density-functional perturbation theory. *Computer Physics Communications*, 182(8):1744–1754, 2011.
- [202] Francesco Sottile, Fabien Bruneval, A. G. Marinopoulos, L. K. Dash, Silvana Botti, Valerio Olevano, Nathalie Vast, Angel Rubio, and Lucia Reining. Tddft from molecules to solids: The role of long-range interactions. *International Journal of Quantum Chemistry*, 102(5):684–701, 2005.
- [203] Artur F. Izmaylov and Gustavo E. Scuseria. Why are time-dependent density functional theory excitations in solids equal to band structure energy gaps for semilocal functionals, and how does nonlocal hartreefock-type exchange introduce excitonic effects? *The Journal of Chemical Physics*, 129(3):–, 2008.
- [204] Andreas Dreuw and Martin Head-Gordon. Failure of time-dependent density functional theory for long-range charge-transfer excited states: the zincbacteriochlorinbacteriochlorin and bacteriochlorophyllspheroidene complexes. *Journal of the American Chemical Society*, 126(12):4007–4016, 2004.
- [205] J. P. Perdew and Alex Zunger. Self-interaction correction to density-functional approximations for many-electron systems. *Phys. Rev. B*, 23:5048–5079, May 1981.
- [206] Andrea Ferretti, Ismaila Dabo, Matteo Cococcioni, and Nicola Marzari. Bridging density-functional and many-body perturbation theory: Orbital-density dependence in electronic-structure functionals. *Phys. Rev. B*, 89:195134, May 2014.
- [207] R. Gaudoin and K. Burke. Lack of hohenberg-kohn theorem for excited states. *Phys. Rev. Lett.*, 94:029901, Jan 2005.
- [208] A. Chutjian, R. I. Hall, and S. Trajmar. Electronimpact excitation of h2o and d2o at various scattering angles and impact energies in the energyloss range 4.212 ev. *The Journal of Chemical Physics*, 63(2):892–898, 1975.
- [209] Leonardo Bernasconi. Statistical average of model orbital potentials for extended systems: Calculation of the optical absorption spectrum of liquid water. *The Journal of Chemical Physics*, 132(18):–, 2010.
- [210] Badry D. Bursulaya, Jonggu Jeon, Dominic A. Zichi, and Hyung J. Kim. Generalized molecular mechanics including quantum electronic structure

- variation of polar solvents. ii. a molecular dynamics simulation study of water. *The Journal of Chemical Physics*, 108(8):3286–3295, 1998.
- [211] Peter R. Ogilby. *Chem. Soc. Rev.*, 39:3181–3209, 2010.
- [212] Francis Wilkinson, W. Phillip Helman, and Alberta B. Ross. Rate constants for the decay and reactions of the lowest electronically excited singlet state of molecular oxygen in solution. an expanded and revised compilation. *Journal of Physical and Chemical Reference Data*, 24(2):663–677, 1995.
- [213] Tsuneki Ichikawa and Larry Kevan. *The Journal of Physical Chemistry*, 84(15):1955–1958, 1980.
- [214] Alfredo Pasquarello, Ingrid Petri, Philip S Salmon, Olivier Parisel, Roberto Car, Éva Tóth, D Hugh Powell, Henry E Fischer, Lothar Helm, and André E Merbach. First solvation shell of the cu (ii) aqua ion: Evidence for fivefold coordination. *Science*, 291(5505):856–859, 2001.
- [215] Vyacheslav S. Bryantsev, Mamadou S. Diallo, Adri C. T. van Duin, and William A. Goddard III. *The Journal of Physical Chemistry A*, 112(38):9104–9112, 2008.
- [216] Peter Pulay. Convergence acceleration of iterative sequences. the case of scf iteration. *Chemical Physics Letters*, 73(2):393 – 398, 1980.
- [217] Osman Bari Malcolu, Arrigo Calzolari, Ralph Gebauer, Daniele Varsano, and Stefano Baroni. Dielectric and thermal effects on the optical properties of natural dyes: A case study on solvated cyanin. *Journal of the American Chemical Society*, 133(39):15425–15433, 2011.
- [218] Maurizio Cossi and Vincenzo Barone. Time-dependent density functional theory for molecules in liquid solutions. *The Journal of Chemical Physics*, 115(10):4708–4717, 2001.
- [219] Benedetta Mennucci, Roberto Cammi, and Jacopo Tomasi. *The Journal of Chemical Physics*, 109(7):2798–2807, 1998.
- [220] Denis Jacquemin, Benedetta Mennucci, and Carlo Adamo. Excited-state calculations with td-dft: from benchmarks to simulations in complex environments. *Phys. Chem. Chem. Phys.*, 13:16987–16998, 2011.
- [221] Iurii Timrov, Oliviero Andreussi, Alessandro Biancardi, Nicola Marzari,

- and Stefano Baroni. Self-consistent continuum solvation for optical absorption of complex molecular systems in solution. *The Journal of Chemical Physics*, 142(3):-, 2015.
- [222] Aleksandr V. Marenich, Christopher J. Cramer, and Donald G. Truhlar. *The Journal of Physical Chemistry B*, 119(3):958–967, 2015.
- [223] Alberto Marini, Aurora Muoz-Losa, Alessandro Biancardi, and Benedetta Mennucci. What is solvatochromism? *The Journal of Physical Chemistry B*, 114(51):17128–17135, 2010.
- [224] Megan E Holtz, Yingchao Yu, Deniz Gunceler, Jie Gao, Ravishankar Sundararaman, Kathleen A Schwarz, Tomas A Arias, Hector D Abruna, and David A Muller. Nanoscale imaging of lithium ion distribution during in situ operation of battery electrode and electrolyte. *Nano letters*, 14(3):1453–1459, 2014.
- [225] Marcus D Hanwell, Donald E Curtis, David C Lonie, Tim Vandermeersch, Eva Zurek, and Geoffrey R Hutchison. *Journal of cheminformatics*, 4(1):1–17, 2012.
- [226] E. J. Reardon. Dissociation constants of some monovalent sulfate ion pairs at 25.deg. from stoichiometric activity coefficients. *The Journal of Physical Chemistry*, 79(5):422–425, 1975.
- [227] Anubhav Jain, Shyue Ping Ong, Geoffroy Hautier, Wei Chen, William Davidson Richards, Stephen Dacek, Shreyas Cholia, Dan Gunter, David Skinner, Gerbrand Ceder, and Kristin a. Persson. The Materials Project: A materials genome approach to accelerating materials innovation. *APL Materials*, 1(1):011002, 2013.
- [228] Matthias Rupp, Alexandre Tkatchenko, Klaus-Robert Müller, and O Anatole von Lilienfeld. Fast and accurate modeling of molecular atomization energies with machine learning. *Physical review letters*, 108(5):058301, 2012.